POLITECNICO
MILANO 1863

Politecnico di Milano
Scuola di Ingegneria Industriale e dell'Informazione
Master of Science in
Materials Engineering and Nanotechnology

A numerical analysis regarding hydrogen embrittlement of additive-manufactured specimens

Supervisor:
Prof. Laura Maria VERGANI
Co-supervisor:
Prof. Chiara COLOMBO

Master Thesis of:
Luca BALZARRO
matr. 893555

Academic year 2019/2020

Abstract

The aim of the present thesis is to numerically investigate the effect of hydrogen embrittlement. The considered material belongs to the class of maraging steels, which feature ultra-high strength and are the top choice in the aerospace and automotive sectors. 18Ni-300 samples were obtained by means of Selective Laser Melting, and successively aged to induce precipitation. The material was characterized from the mechanical and microstructural points of view. Both the tensile strength and the hardness exhibit very large values, and are in accordance with literature. SEM observations highlight the cellular solidification structure, typical of additevely manufactured maraging steels. Density measurements confirmed the correct choice of the process parameters, which led to a negligible porosity presence. A numerical model was built, with the goal of correctly describing hydrogen diffusion inside the material and its effect on mechanical properties. The model is fully coupled, simultaneously solving the mechanical and diffusional problems. The solution is possible, in ABAQUS, exploiting a thermal-diffusional analogy. The crack advancement was modelled by means of Cohesive Zone Modelling. The cohesive parameters were calibrated basing on the experimental data in absence of hydrogen. Several initial conditions were analyzed, highlighting the influence of the main parameters affecting the problem.

Keywords: Hydrogen Embrittlement, Maraging, Additive Manufacturing, Cohesive Zone Modelling

Sommario

Lo scopo di questa tesi è di investigare per via sperimentale e numerica l'effetto dell'infragilimento da idrogeno. Il materiale considerato appartiene alla classe degli acciai maraging, che sono caratterizzati da una resistenza ultra alta, e sono la miglior scelta nei settori aerospaziale e automotive. I provini di 18Ni-300 sono stati ottenuti tramite Selective Laser Melting, e successivamente invecchiati per indurre precipitazione. Il materiale è stato caratterizzato dai punti di vista meccanico e microstrutturale. Sia la resistenza a trazione che la durezza mostrano valori molto elevati, e sono in accordo con la letteratura. Le osservazioni al SEM evidenziano la struttura di solidificazione cellulare, tipica degli acciai maraging ottenuti per manifattura addittiva. Le misure di densità hanno confermato la scelta corretta dei parametri di processo, che hanno portato la presenza di porosità ad essere trascurabile. Un modello numerico è stato costruito con lo scopo di descrivere adeguatamente la diffusione dell'idrogeno all'interno del materiale, e il suo effetto sulle proprietà meccaniche. Il modello è completamente accoppiato, risolvendo contemporaneamente sia il problema meccanico che di diffusione. La soluzione è possibile, in ABAQUS, sfruttando un'analogia termo-diffusionale. L'avanzamento della cricca è stato implementato tramite il Modello a Zona Coesiva. I parametri coesivi sono stati calibrati basandosi sui dati sperimentali in assenza di idrogeno. Sono state analizzate diverse condizioni iniziali, evidenziando l'influenza dei principali parametri del problema.

Parole chiave: Infragilimento da idrogeno, Maraging, Manifattura Addittiva, Modello a Zona Coesiva

Contents

List of Figures

List of Tables

List of Abbreviations

AIDE	Adsorption-Induced Dislocation Emission
AM	Additive Manufacturing
ASTM	American Society of Testing and Materials
BCC	Body Centered Cubic
CAD	Computer Aided Design
CMOD	Crack Mouth Opening Displacement
CTOD	Crack Tip Opening Displacement
CZM	Cohesive Zone Modelling
DED	Directed Energy Deposition
EBM	Electron Beam Melting
EDM	Electro Discharge Machining
EPFM	Elasto-Plastic Fracture Mechanics
FCC	Face Centered Cubic
FEM	Finite Element Method
FM	Fracture Mechanics
GA	Gas Atomization
HE	Hydrogen Embrittlement
HEDE	Hydrogen Enhanced DE-cohesion
HEI	Hydrogen Embrittlement Index
HELP	Hydrogen Enhanced Localized Plasticity
HEZ	Hydrogen Embrittled Zone
HIP	Hot Isostatic Pressing
HP	Horizontal Plane
IHT	Intrinsic Heat Treatment
LEFM	Linear Elastic Fracture Mechanics
MPC	Multi Point Constraint

NILS	Normal Interstitial Lattice Site
PBF	Powder Bed Fusion
PREP	Plasma Rotating Electrode Process
RA	Rotary Atomization
RP	Rapid Prototyping
RS	Residual Stresses
RUC	Representative Unit Cell
SEM	Scanning Electron Microscope
SENT	Single Edge Notch Tension
SIF	Stress Intensity Factor
SLM	Selective Laser Melting
TEM	Transmission Electron Microscope
TSL	Traction Separation Law
UTS	Ultimate Tensile Strength
VP	Vertical Plane
WA	Water Atomization
YS	Yield Strength

Introduction

The aim of this master's thesis is to investigate the effect of Hydrogen Embrittlement (HE) with numerical tools, based on the Finite Element Method (FEM). HE is a phenomenon widely studied in literature and of uttermost importance in several fields, but the specific mechanisms governing it are still object of debate [1]. Additionally, it is mostly taken into account in the design phase solely by means of empirical correlations. It consists of atomic hydrogen penetrating into the material and diffusing through the metal lattice, resulting in a general degradation of the mechanical properties, especially the toughness and the load-carrying ability. Among the materials susceptible to this phenomenon, we recall high-strength steels, aluminum and titanium alloys.

The fields in which HE is of major concern are the chemical sector, being hydrogen a reagent or a product in a variety of processes, the Oil & Gas industry, where corrosion in *sour* (H_2S containing) environments is a well known issue, and, recently, the energy one, as interest and research on hydrogen as an energy vector have increased over the years. In particular, the feasibility of using it as a clean combustible also requires both a proper storage unit [2], and dedicated pipelines for its transportation, which therefore have to be designed with specific regard to HE. For this reason, a proper numerical tool to consider the phenomenon in the design phase is needed.

The recent and fast development of Additive Manufacturing (AM) of metals paves the way to a variety of applications, in several sectors. The American Society of Testing and Materials (ASTM) generally defines AM as *"the process of joining materials to make objects from 3D model data, usually layer upon layer, as opposed to subtractive manufacturing methodologies"* [3]. This technique is particularly advantageous for the production of one-of-a-kind parts, offering a vast possibility in the customization of products, with a largely increased geometrical complexity. Among the available AM processes, the industrially most relevant ones make use of a thermal source for obtaining the desired shape. The metal powder rapidly undergoes local melting, solidification and subsequent cooling. This quite harsh thermal cycle generates peculiar solidification microstructures and provokes the rise of residual stresses in the component; the entity and the consequences of them depend on several factors, possibly leading to instantaneous cracking of the part.

It is well known that a stress field can influence hydrogen diffusion, and that

hydrogen concentration modifies the stress field, but, up to now, the specific combination of HE and residual stresses due to AM has been object of little investigation, and no numerical modeling tool is available.

In the first chapter, the nature of the problem is introduced, recalling the basics of Fracture Mechanics, since the advancement of the crack tip, and the stress field around it, are fundamental in order to describe the phenomenon. Moreover, the equations governing hydrogen diffusion are reported and explained: with respect to the well-known Fick's laws, one should additionally consider the hydrostatic stress gradient and the plastic strain. Subsequently, the main hydrogen embrittlement mechanisms, as theorized and debated by literature, are illustrated. Furthermore, Additive Manufacturing is introduced, with a specific regard to the residual stresses arising in the parts production. Lastly, the maraging steels properties and microstructure, obtained both by conventional processes and by AM, are presented.

In the second chapter, based on the experimental work, the tensile properties of 18Ni-300 are investigated. The samples were manufactured by means of Selective Laser Melting and successively aged, in order to allow precipitation strengthening. The stress-strain curve highlights the material ultra-high strength, together with small ductility. The micrographies of the as-built, polished and fractured samples are shown and described. The fractography contains both ductile and brittle features, indicating a mixed-mode failure. The material characterization includes microhardness and density measurements, whose results were in accordance with literature.

The third chapter follows the creation of the numerical model. Half of the toughness test specimen is modelled, in a 2D geometry. The simulations are run in ABAQUS, exploiting the thermal-diffusional analogy by means of the PoliHydra open-source subroutines collection; this makes the implementation of the hydrogen diffusion and embrittlement equations possible. Crack advancement is modelled by means of cohesive elements, whose working principle is illustrated. Additionally, a method to consider the residual stresses arising from the manufacturing process is described.

Last, in the fourth chapter, the results of the simulations are presented and discussed. First, the Traction Separation Law is calibrated by trial and error, looking for a minimum mismatch between the numerical and experimental toughness curves, without hydrogen. The goal of the calibration is to obtain the set of parameters which describe the behavior of the cohesive elements. Then, the hydrogen simulation is run, obtaining a prediction of the toughness behavior of the charged specimen. The distribution of lattice-solved, C_L, and trapped hydrogen, C_T, are shown, with a negligible value of the latter contribution with respect to the first one. The C_L field depends on the hydrostatic stress gradient and on the time available for diffusion, while C_T is determined basing on the plastic strain, which creates additional trapping sites. The effect on the mechanical behavior is implemented reducing the cohesive energy proportionally to the total hydrogen concentration.

Chapter 1

State of the art

1.1 Recall of Fracture Mechanics

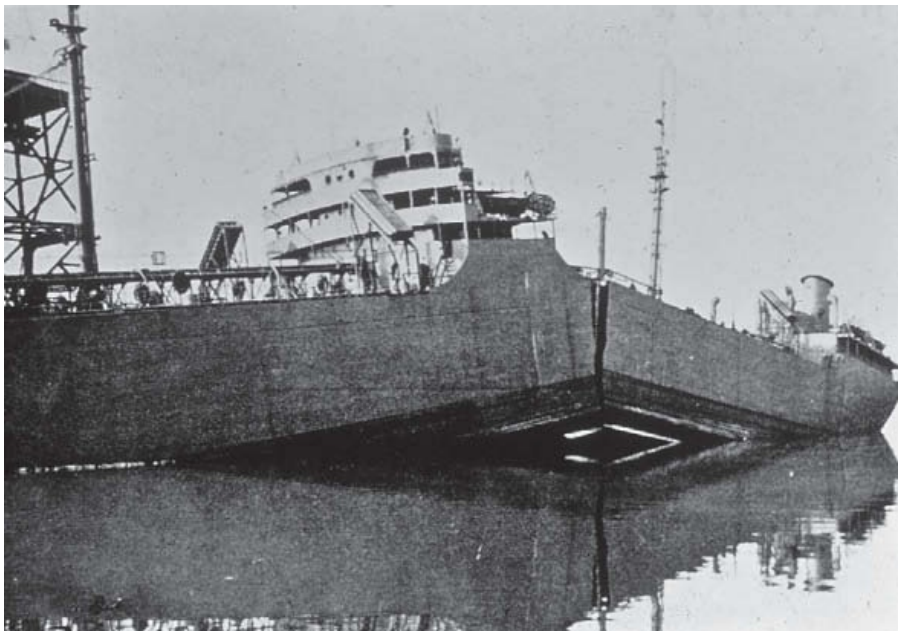

Figure 1.1: A Liberty Ship split into two parts after catastrophic failure.

Even though the studies on this subject began a little earlier, the extensive research on Fracture Mechanics (FM) started after the Liberty Ships' catastrophic failures in World War II. In order to accelerate the production of warships, the U.S. army vastly replaced riveted connections with welds. When in service, the behavior was unexpected and impressive, leading to a considerable number of ships split into two parts (Figure 1.1). The successive investigations showed no mistakes in the design, being the stress always lower than the admissible one. On the other hand, fractures always started from welds or notches, and Charpy-impact testing of the employed steel resulted in a low value of the impact energy [4]. This led to a new approach in design, called *damage tolerant*. According to this new design philosophy, the presence and size of defects are taken into account in the calculation of the limit load, and the combination of applied stress, crack length and material

toughness determines whether a specific condition is critical.

Fracture Mechanics has shown to be of major engineering importance, as cracks and flaws are always present in a material. As a matter of fact, the traditional approach, based only on tensile, compressive and bending tests, implicitly includes the effect of microscopic cracks in the definition of the strength of a material, but it is incapable of considering larger defects [5].

1.1.1 Stress at a crack tip

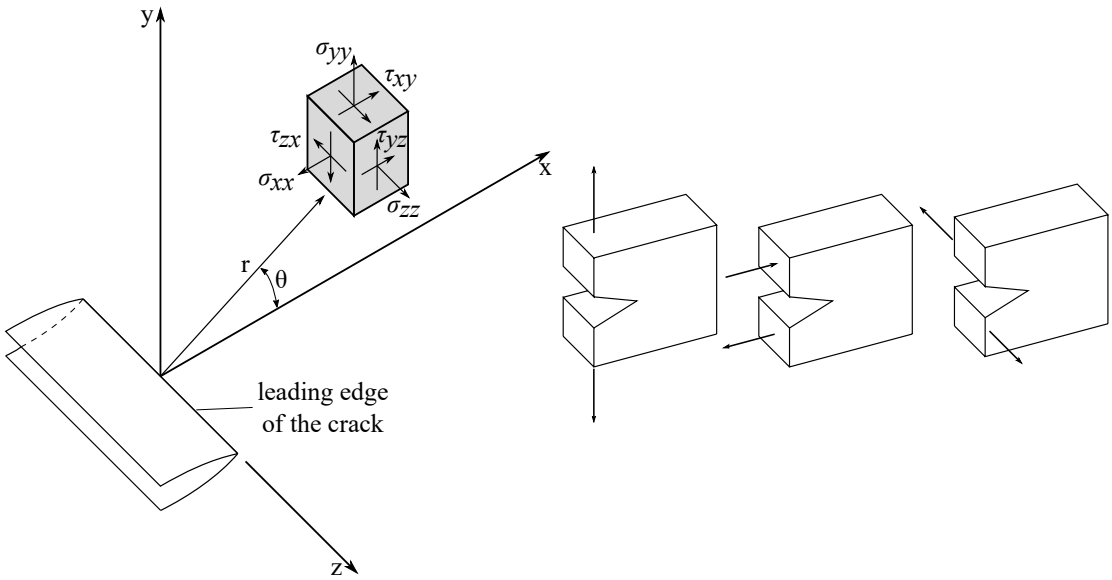

(a) Stresses near the tip of a crack. **(b)** Opening modes I, II and III.

Figure 1.2

In Linear Elastic Fracture Mechanics (LEFM), the stress field in the vicinity of the crack tip is generally expressed as

$$\sigma_{ij} = \frac{K}{\sqrt{2\pi r}} f_{ij}(\theta) + \text{other terms}, \tag{1.1}$$

where K is named Stress Intensity Factor (SIF), r is the distance from the tip and $f_{ij}(\theta)$ is a function which depends on the angular position θ of the considered point, on the stress component and on the opening mode. Figure 1.2(a) shows the representation of the material element in polar coordinates. In defining K in LEFM, one assumes the material to behave in a linear-elastic manner, according to Hooke's law.

A cracked body can be, in general, loaded in any combination of the three modes reported in Figure 1.2(b). In Mode I, the *opening mode*, the crack faces are simply moving apart, being the consequence of tension loading. On the other hand, Mode II and III are caused by shear loading, in different directions: these are called *sliding* and *tearing* modes, involving relative sliding of the crack faces in

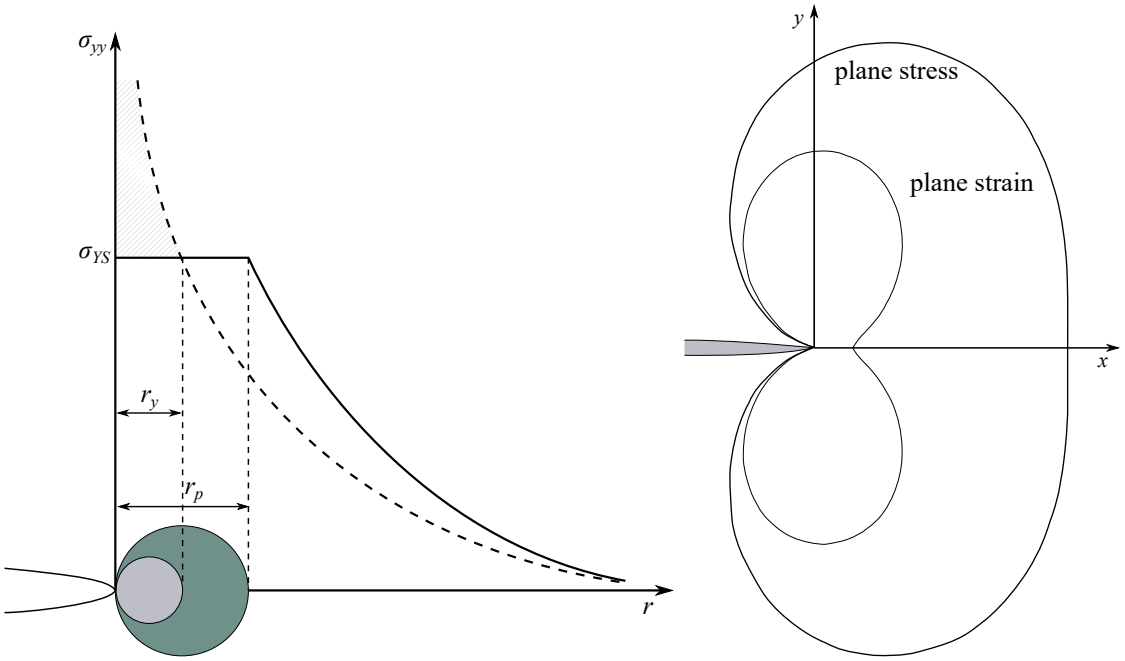

(a) Stress redistribution in elasto-plastic material, at $\theta = 0$. The hatched region corresponds to the load that has to be redistributed, resulting in a larger plastic zone.

(b) Plastic zone shape (adapted from [6]).

Figure 1.3

a direction normal or parallel to the leading edge, respectively [5].

Mode I is the most studied case, as the majority of cracking problems of engineering interest involve tension stresses. In this case, the stress components, derived on the basis of the theory of linear elasticity, are written, omitting the higher order terms, as

$$\begin{aligned}
\sigma_{xx} &= \frac{K_I}{\sqrt{2\pi r}} cos\frac{\theta}{2}\Big[1 - sin\frac{\theta}{2}sin\frac{3\theta}{2}\Big] \\
\sigma_{yy} &= \frac{K_I}{\sqrt{2\pi r}} cos\frac{\theta}{2}\Big[1 + sin\frac{\theta}{2}sin\frac{3\theta}{2}\Big] \\
\tau_{xy} &= \frac{K_I}{\sqrt{2\pi r}} cos\frac{\theta}{2}sin\frac{\theta}{2}cos\frac{3\theta}{2} \\
\sigma_{zz} &= 0 \qquad\qquad\quad \text{in plane stress} \\
\sigma_{zz} &= \nu(\sigma_{xx} + \sigma_{yy}) \quad \text{in plane strain, } \epsilon_z = 0 \\
\tau_{xz} &= 0 \\
\tau_{yz} &= 0
\end{aligned} \tag{1.2}$$

The choice between the σ_{zz} expression, assuming plane strain or plane stress, depends on the component thickness. The stress intensity factor K_I is expressed as a function of the nominal stress σ and the crack length a as

$$K_I = F\sigma\sqrt{\pi a}, \tag{1.3}$$

with F being a geometrical factor.

It should be noted that the expressions in Equation 1.2 are only valid in a region close to the crack tip, called the *K-dominant zone*. Also, all the non-zero components predict a rapid increase of the stress as one moves towards the crack tip, *i.e.* $r \to 0$, predicting a singularity of order $1/\sqrt{r}$. The presence of an infinite stress in a material would obviously be unphysical; in fact, once the stress has reached the yielding value, a plastic zone is formed around the crack tip, which allows redistributing the stresses. Figure 1.3(a) shows the theoretical and redistributed stress trends for $\theta = 0$, while Figure 1.3(b) illustrates the shape of the plastic zone in the plane stress and strain cases. This plot is obtained employing the Von Mises criterion, *i.e.*

$$\sigma_{YS} = \frac{1}{\sqrt{2}}\Big((\sigma_1 - \sigma_2)^2 + (\sigma_2 - \sigma_3)^2 + (\sigma_3 - \sigma_1)^2\Big)^{1/2} \tag{1.4}$$

One can observe that the plastic zone has a different size depending on the state of stress; in particular, in a plane strain condition this value is lower, resulting in a reduced stress redistribution, which leads to a more detrimental situation.

1.1.2 Elasto-Plastic Fracture Mechanics

As previously described, the creation of a plastic zone modifies the stress trend around a crack tip. If this region is sufficiently small, one can assume that Equation 1.2 still holds in the K-dominant zone. On the other hand, Elasto-Plastic Fracture Mechanics (EPFM) was born in order to be able to correctly describe the behavior of materials characterized by high toughness, in which the extension of the plastic zone is too large for the application of LEFM. Specifically, K turns out to not be adequate anymore for a correct description of the stress field in the vicinity of the crack tip, actually underestimating its severity.

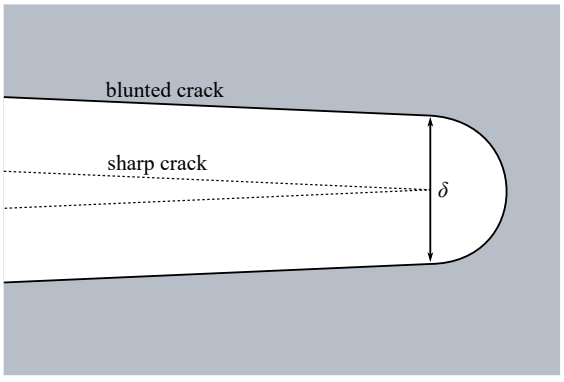

Figure 1.4: Blunting of the crack tip (from [7]).

In fact, experimental observations of a cracked specimen showed a blunting of the initially sharp crack tip, with the crack faces moving apart from each other; the tougher the material, the larger the degree of blunting. This opening of the

crack is named Crack Tip Opening Displacement (CTOD), or δ. One can find a variety of precise definitions of the CTOD value, depending on the specific model employed: the most common one is shown in Figure 1.4, where δ is evaluated in correspondence of the original (before blunting) crack tip [7].

In EPFM, a new key parameter is defined in order to describe the fracture conditions in components experiencing both elastic and plastic deformations. The J integral is defined, in a formal mathematical sense, as [8]

$$J = \int_{\Gamma} W dy - \mathbf{t} \cdot \frac{\partial \mathbf{u}}{\partial x} ds, \tag{1.5}$$

where the line integral is evaluated along any closed path around the crack tip, Γ (Figure 1.5). In fact, the independency of J on the choice of Γ can be demonstrated. In Equation 1.5, $W = \int \sigma_{ij} d\epsilon_{ij}$ is the strain energy density, $\mathbf{t}$ represents the stress vector acting on the contour, $\mathbf{u}$ the displacement vector and finally ds measures the distance along the curve Γ.

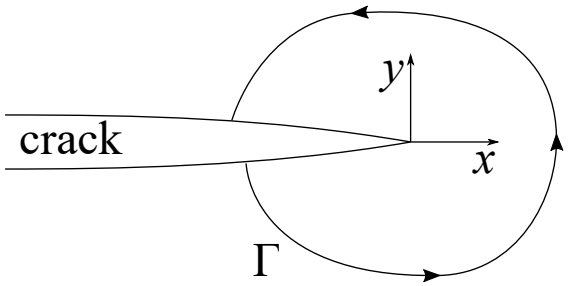

Figure 1.5: Definition of the path Γ around the crack tip.

J fulfills the role that K has in LEFM, *i.e.* is a measure of the intensity of the stress field around the crack tip; actually, if one considers a linear elastic material, the fields described by K and J coincide. Employing J, the fracture criterion simply becomes $J = J_C$.

The measurement of the resistance of a material to crack extension is called toughness test. The value of J can be experimentally obtained starting from the area below the load-displacement curve; this value increases with Δa, describing the resistance (R) curve. Other than the J-Δa one, the CTOD R-curve can be defined and recorded, correlating the crack tip opening displacement to crack advancement.

1.2 Hydrogen Embrittlement

1.2.1 Hydrogen diffusion

The macroscopic effect of the embrittlement is the result of hydrogen diffusion through the lattice, defining the concentration at the crack tip. Atomic hydrogen, after having being absorbed on the surface, moves easily towards the core through

the metal lattice, thanks to its small radius (53 pm) [9]. Diffusivity is strongly dependent on the type of lattice, the presence and nature of precipitates, the plastic strain and the stress state. In particular, a compressive state of stress has been shown to reduce hydrogen diffusivity [10]. An intuitive visualization of this last point is based on the fact that the lattice parameters are locally shortened, reducing the cross-sectional area free for diffusion.

The mathematical treatment of diffusion starts from the well-known Fick's laws:

$$\mathbf{J} = -D_L \nabla C \tag{1.6}$$

$$\frac{\partial C}{\partial t} = D_L \nabla^2 C, \tag{1.7}$$

in which the lattice is considered perfectly homogeneous, and diffusion is only due to the concentration (C) gradient [11]. Equation 1.6 holds in stationary conditions, where the flux $\mathbf{J}$, expressed as the number of atoms flowing per unit time through a unit area, is constant over time; more generally, Equation 1.7 is employed.
The diffusivity D_L represents the velocity with which atoms can move through the lattice and, being an activation energy E_a required to jump between two subsequent sites, it can be expressed through an Arrhenius law:

$$D_L = D_0 \, exp\Big(-\frac{E_a}{RT}\Big), \tag{1.8}$$

with $R = 8.314 \, \frac{J}{mol \cdot K}$ being the universal gas constant, T the absolute temperature and D_0 the diffusivity at infinite temperature. D_0 depends on the lattice arrangement: namely, its value is higher for ferritic (BCC) steels than for the austenitic (FCC) ones [12].

In reality, as previously mentioned, the stress field affects hydrogen diffusion: since the atomic radius is larger than the interstitial sites, hydrogen presence results in a cubic distortion of the lattice. This induces a macroscopic volume change V_H per mole of H, which can be experimentally measured. Microscopically, hydrogen atoms interact with the hydrostatic part of the stress tensor $\sigma_H = \frac{1}{3} trace(\underline{\underline{\sigma}})$ [13], leading to a variation of the chemical potential of $\sigma_H \cdot V_H$ [14].

In thermodynamic equilibrium, the hydrogen chemical potential has to be uniform all over the lattice. Therefore, if a non-uniform distribution of the hydrostatic stress is present, as in the case of a crack tip, a redistribution of hydrogen will occur [13]:

$$\begin{aligned} \mu_H(\sigma_H = 0) &= \mu_H^0 + RTlnC_0 = \\ \mu_H(\sigma_H \neq 0) &= \mu_H^0 + RTlnC(x) + \sigma_H V_H, \end{aligned} \tag{1.9}$$

being μ_H^0 is the standard value of the potential and C_0 is the concentration where the hydrostatic stress is zero, and

$$C(x) = C_0 \, exp\Big(\frac{\sigma_H(x) V_H}{RT}\Big). \tag{1.10}$$

It is to be underlined that Equation 1.9 holds only in the case of an ideally diluted solution, practically at low H concentrations [13].

Following Sofronis and McMeeking [15], Equation 1.6 can be modified to take the stress contribution into account:

$$\mathbf{J} = -D_L \nabla C_L + \frac{D_L C_L V_H}{RT} \nabla \sigma_H \tag{1.11}$$

The meaning of Equation 1.11 is that hydrogen will migrate towards the regions characterized by low concentrations and large hydrostatic stresses.

1.2.2 Hydrogen trapping

Hydrogen is considered to move through the lattice from one Normal Interstitial Lattice Site (NILS) to another. Past evidence [16] showed that the dislocation transport mode, *i.e.* with hydrogen diffusing along a dislocation line, is negligible. Interstitial diffusion is slowed down by traps: these are sites offering a favorable energetic environment for the atom [17], and are very different in their microstructural nature. In fact, this broad definition includes dislocations, grain boundaries, voids and inclusions. From a practical point of view, traps can be divided into two categories: reversible traps feature a limited time of residence of hydrogen, while in the irreversible ones H can be thought as permanently captured, with a low probability of being released [18].

Oriani [17] developed a theory for diffusion and trapping of hydrogen, assuming equilibrium between the trapped and solved hydrogen populations. More precisely, we can write their respective concentrations in atoms per unit volume as

$$C_T = \theta_T \alpha N_T \tag{1.12}$$
$$C_L = \theta_L \beta N_L, \tag{1.13}$$

where α and β denote, respectively, the number of sites per trap and the number of NILS per solvent atom, N_T and N_L are the volume densities of traps and solvent lattice atoms, and θ_T and θ_L are the occupancies of traps and NILS. β and N_L are material constants, where β is dependent on the lattice arrangement, and N_L can be computed as $N_L = \frac{N_A}{V_M}$, where N_A is the Avogadro's number and V_M is the molar volume of the solvent.

The equilibrium between NILS and trap sites can be expressed substituting the fractional occupancies in place of the activities in the equilibrium constant $K_T = a_T/a_L$ [17]:

$$\frac{\theta_T}{1-\theta_T} = \frac{\theta_L}{1-\theta_L} K_T. \tag{1.14}$$

The equilibrium constant can, in general, be expressed as

$$K_T = exp\Big(-\frac{\Delta W}{RT}\Big), \tag{1.15}$$

being ΔW the trap binding energy. This energy can vary greatly depending on the nature of the trap, and a summary of values is reported in Table 1.1.

Trap site		Trap binding energy ΔW (kJ/mol)	
		α-Fe	γ-Fe/Ni
Dislocation		20-58	10-20
Grain boundary		10-58	10-20
Precipitates and inclusions	MnS:	29-57	-
	AlN:	48-58	-
	Fe_3C:	57-84	-
	TiC:	95	-
Lacunae		46-54	20-42
Internal surface and void		28-96	41-53

Table 1.1: Trap binding energies, as reported by [19, 20].

Therefore, assuming a low occupancy of NILS, *i.e.* $\theta_L \ll 1$, the concentration at trap sites becomes:

$$C_T = \frac{\alpha N_T}{1 + \frac{\beta N_L}{K_T C_L}} \tag{1.16}$$

As said, the presence of traps slows down the diffusion process. To take this phenomenon into account, it is possible to introduce an effective diffusivity D_T [21]:

$$D_T = D_L \frac{1}{1 + K_T \frac{\alpha N_T}{\beta N_L}}, \tag{1.17}$$

which will feature lower values with respect to the theoretical one.

Combining the effect of diffusion in a stress field and trapping, Krom [22], basing on the work of Sofronis and McMeeking [15], obtained:

$$\frac{C_L + C_T(1-\theta_T)}{C_L}\frac{\partial C_L}{\partial t} = D_L \nabla^2 C_L - \nabla \cdot \left(\frac{D_L V_H}{RT} C_L \nabla \sigma_H\right) - \alpha \theta_T \frac{dN_T}{d\epsilon_p}\frac{d\epsilon_p}{dt} \tag{1.18}$$

This last equation, commonly implemented in numerical models for the prediction of hydrogen diffusion, includes a term related to plastic strain. In fact, being dislocations one of the possible sources of trapping, plasticity will influence the trap density, and therefore the diffusion. In other words, the material region close to a stress raiser, *e.g.* a crack tip, will experience a large concentration, as hydrogen will be attracted by the high stress, and then trapped by the sites created in the plastic zone.

1.2.3 Hydrogen embrittlement mechanisms

As mentioned before, the understanding of the specific mechanism leading to the worsening of the mechanical properties is still to be achieved [1]; in fact, many

proposals have emerged during the years, and, in general, more than one mechanism could be active at a time. The specific active mechanisms depend on material composition, microstructure and external conditions [23]. Among them, we recall Hydrogen Enhanced DE-cohesion (HEDE), Hydrogen Enhanced Localized Plasticity (HELP), Adsorption-Induced Dislocation Emission (AIDE) and hydride formation and cleavage.

More in detail, the HEDE mechanism, first postulated by Pfeil in 1926 [24] and then developed by Troiano [25] and Oriani [17], describes HE as a localized weakening of the inter-atomic bonds, consequently resulting in a reduction of the energy needed for the creation of new surfaces [1]. Hydrogen, lying at the crack tip because of trap-induced segregation [26], damages the material where the local crack tip tensile stress exceeds the bonding strength.
Other than at the crack tip, this critical combination of high concentration of hydrogen and stress could occur several tens of nanometers ahead of the crack, where the shielding effect of dislocations results in a maximum of the tensile stress [27]. In this position voids can form, favoring the brittle crack propagation. The fracture prediction is possible when the crack tip stress, the hydrogen concentration at damage sites and its relation with the bonding strength are known.

This mechanism is supported by the tendency of hydrogen to diffuse towards high stress regions, like the crack tip. Additionally, quantum simulations validate the weakening effect of hydrogen on the cohesive strength [28, 29]. However, due to the rather complex task of observing directly the events occurring at the atomic scale, direct experimental proof is difficult to obtain [27]. In fact, the observation that an increasing hydrogen content leads to a reduction of the crack tip opening angle is the principal evidence of HEDE [30].

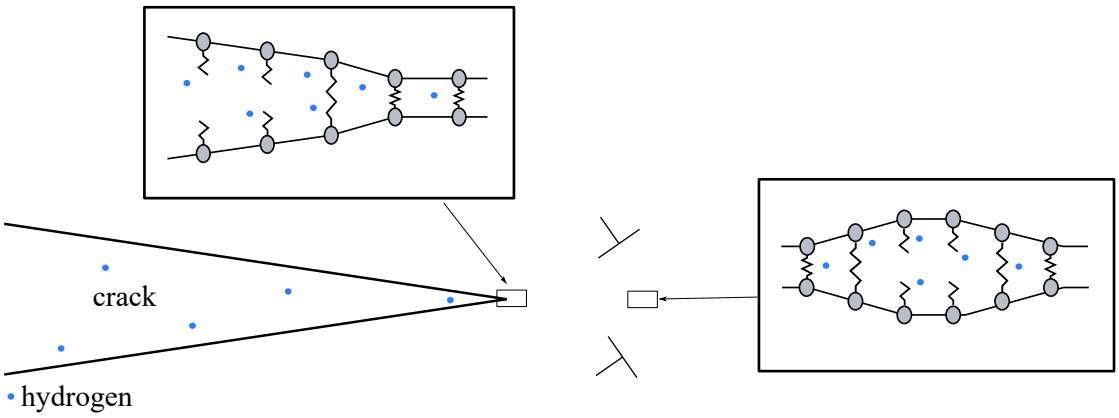

Figure 1.6: Scheme of the HEDE mechanism. The figure on the right illustrates the void formation ahead of the crack tip. The light blue circles represent the hydrogen atoms (from [31]).

In HELP, instead, hydrogen reduces the local stress required for dislocation motion. In this way, plastic deformation gets localized, resulting in a subcritical growth by localized microvoid coalescence, with brittle characteristics on the macroscopic scale [32].

More specifically, in HELP the enhanced dislocation mobility is due to hydrogen accumulation around dislocation cores, with a consequent reduction of the elastic energy required for overpassing the obstacles. In fact, atomistic simulations have shown how the presence of hydrogen lowers the dislocation core energy, reducing the stress required for their movement [33]. In addition, Robertson [34] directly observed the increased dislocation activity using a high-voltage Transmission Electron Microscope (TEM): upon hydrogen introduction, stationary dislocations start moving, and, at the same time, the ones already in motion accelerate by 1-2 orders of magnitude.

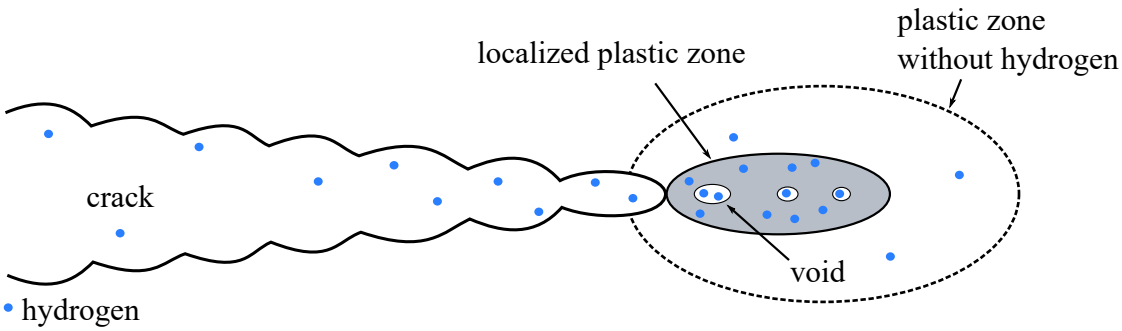

Figure 1.7: Scheme of the HELP mechanism. The light blue circles represent the hydrogen atoms (from [31]).

On the other hand, in AIDE, first proposed by Lynch [35], the weakening of the metal bond leads to enhanced dislocation emission at the crack tip [36]. The nucleation stage is critical, and favored by adsorption. Once nucleated, dislocations can easily move away from the tip, leading to crack growth. Additionally in this model, crack growth, other than dislocation emission, involves nucleation and growth of microvoids ahead of crack tips. Indeed, at slip-band intersections the stresses are sufficiently high to induce some dislocation activity [37]. The resulting crack paths may be intergranular or transgranular, depending on the relative ease of dislocation emission and void nucleation. In fact, atomistic calculations [38] show that adsorbed hydrogen facilitates dislocation emission from the crack tips, given the slip planes are favorably oriented.

Lastly, hydride formation is a specific case of the hydrogen-induced phase change mechanisms. Several types of phases may contribute; it is sufficient that they are stabilized by the presence of hydrogen and the crack tip stress field, and that the so formed phases are brittle. The typical systems exhibiting hydride embrittlement are Nb, V, Ta, Zr, Ti and their alloys. This mechanism is active under conditions where the rate of hydride formation is sufficiently high to preclude other forms of failure, ultimately depending on the thermodynamical stability of these phases [39]. According to this mechanism, hydrogen diffuses towards the regions featuring high hydrostatic stress, so that a hydride phase can nucleate and grow; once a critical size is reached, the crack advances by particle cleavage, and is arrested at the hydride-matrix interface.

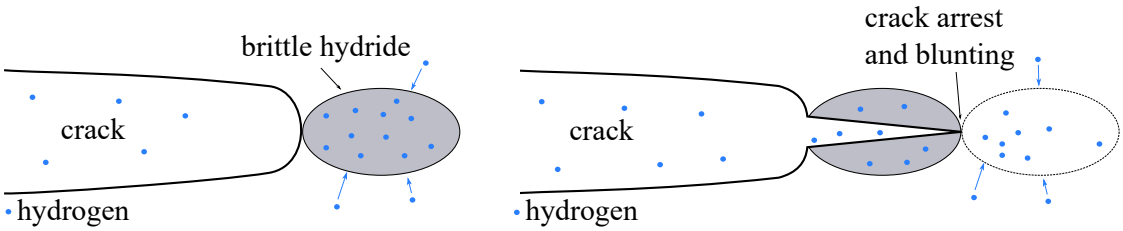

Figure 1.8: Scheme of hydride formation and cleavage. The light blue circles represent the hydrogen atoms (from [31]).

1.2.4 Numerical modeling of HE

Over the years, several attempts regarding the numerical simulation of hydrogen embrittlement have been conducted.

Brocks *et al.* [40] developed a non-open source code capable of describing adsorption, diffusion and the weakening effect of hydrogen on the material. In this work, followed then by the one of Gobbi *et al.* [41], the stress and diffusion problems are fully coupled and solved simultaneously. Even though a commercial code coupling these problems is not yet available, the authors exploit the analogy between the equations governing the coupled heat transfer-stress problem, implemented in ABAQUS, and the current one.

More in detail, the authors [40] based their modeling on a high strength, low alloy steel C(T) specimen, electrochemically hydrogen charged *in situ*, during the CTOD toughness test. They built a 2D plane strain model, refining the mesh around the crack tip using trapezoidal elements, obtaining a minimum element size of 62.5 µm, and implementing aspects from both HEDE and HELP mechanisms. They analyzed an "on air" and three hydrogen charged tests, with different displacement rates. Having obtained a good agreement with the experimental data, they moved their attention at investigating the impact of switching off the effects of one of the two mechanisms at a time: the results indicated that, in order to correctly predict the material behavior, a synergetic role of the two mechanisms is needed. In fact, HEDE is reasonably accurate at low displacement rates, but predicts a too brittle behavior at high $\dot{u}$; conversely, HELP can correctly describe crack advancement in a fast test, underestimating the crack extension at low deformation rates. The comparison between the two mechanisms is shown in Figure 1.9.

Additionally, comparisons are also made for the surface kinetics and diffusion law. Regarding the first subject, the authors observed only a slight difference between considering a surface kinetics model and a constant equilibrium concentration, *i.e.* neglecting the transient character of hydrogen absorption. On the other hand, the mismatch from the Fick's equation and the enhanced diffusion equation they employed (Equation 1.18) is more appreciable: in fact, the coupling of diffusion with mechanical quantities results in a reduced crack extension resistance for all the displacement rates.

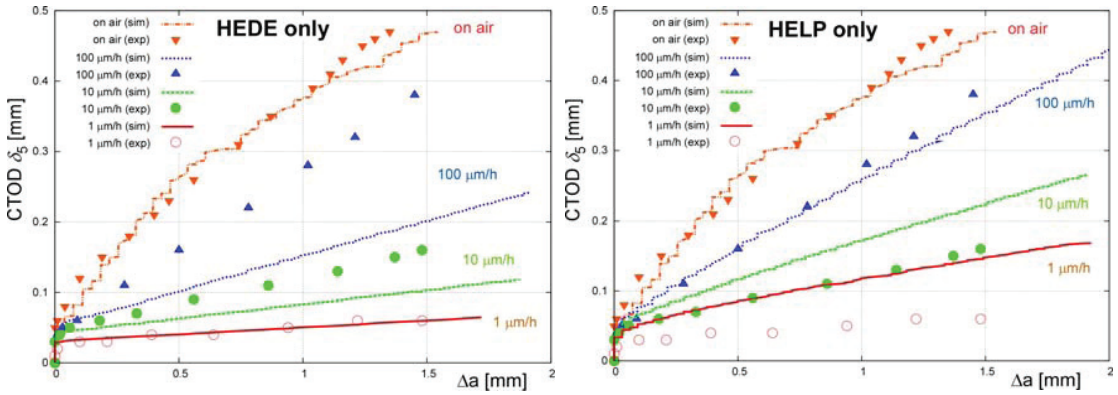

Figure 1.9: Comparison between the effects of HEDE and HELP mechanisms, from Brocks [40].

The group of Alvaro and Olden [42–45] thoroughly investigated hydrogen embrittlement and its modeling. In their early work, the authors built a 2D model to simulate the behavior of a 25% Cr duplex stainless steel. In particular, it was possible to demonstrate the significant influence of trapping on hydrogen concentration: C_L shows a peak in correspondence of the stress one, whereas C_T is maximum close to the surface, due to plastic strain, which offers new trapping sites.

Subsequently, the group switched their investigation towards a pipeline steel, namely the API X70. They first employed a bi-dimensional model similar to the previous one, before extending the analysis to a 3D representation of the specimen. The chosen mesh features a rather small size of the finest element, corresponding to 7.5 µm. A comparison between the 2D and 3D results is offered: the latter produces higher peak stresses, at a position further away from the crack tip. Moreover, the effective plastic strain almost doubles the corresponding value of the bi-dimensional model.

In all their works, the authors employed a three-step procedure, successively implemented by Gobbi *et al.* [46] as well. In this method, the diffusion-stress problem is decoupled: initially, a static analysis is conducted, in order to obtain the value, and, more importantly, the gradient of the hydrostatic stress; then, the diffusion of hydrogen, influenced by σ_H (Equation 1.11) is evaluated, obtaining the hydrogen concentration in the lattice, C_L; lastly, after having evaluated the trapped hydrogen C_T, obtaining the total concentration C, a final static cohesive analysis is conducted. In this last step, the resistance of the elements is reduced proportionally to the local hydrogen concentration.

Recently, Yang *et al.* [47] conducted a thorough investigation of hydrogen diffusion in the Ti-6Al-4V titanium alloy. They modeled a square plate with a central hole, and analyzed the coupling effects between stress and diffusion. In order to solve the coupling problem in COMSOL, three modules are used, namely the built-in solid mechanics and mass transport ones, and a general PDE one, which allowed describing the relation between C_T, C_L and ϵ_p.
After having verified their model comparing the results of pure diffusion with the

analytical expressions, the authors assumed a uniform initial hydrogen concentration, with no flux through the edges during the simulation. A tensile load is applied on the upper edge, and hydrogen diffusion is investigated at various stress levels. They observe that, at low remote stress levels, the hydrostatic stress features a maximum in correspondence of the crack tip, causing hydrogen diffusion towards it. However, when the remote stress overcomes 300 MPa, the local stress at the crack tip exceeds the yield limit, leading to a modification of the hydrostatic stress trend, which now shows a peak ahead of the tip. This fact, in turn, causes a dramatic change of the hydrogen concentration trend, both in the lattice and in the traps. In particular, after a sufficient diffusion time the concentration peak in front of the tip vanishes, and C_L and C_T assume value much lower than in the elastic stage (Figure 1.10).

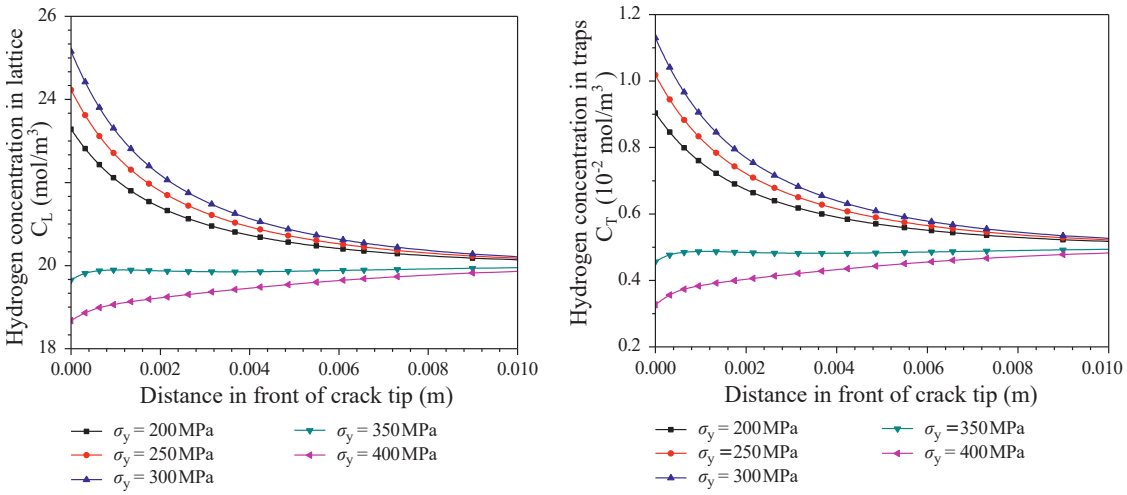

Figure 1.10: C_L and C_T trends in front of the crack tip. The initial homogeneous concentration was set to 20 mol/m^3. σ_y represents the remote stress (from [47]).

Moriconi *et al.* [19, 48] extended the coupled modeling in order to account for a cyclic stress state. The authors implemented the HEDE mechanism in the simulation of the behavior of the 15-5 PH maraging steel. In order to be able to describe cyclic effects, a UMAT subroutine with non-linear kinematic hardening was added, and the damage variable was decomposed into monotonic and cyclic parts. The smallest element size has been chosen to be 2 µm. The results of the simulation without hydrogen show an appreciable prediction of the experimental crack growth curves, for two different load ratios. Introducing hydrogen and considering the elasto-plastic behavior to be independent on it, a fair agreement is obtained in the case of low hydrogen pressure (0.09 MPa), while at high pressures (9 MPa) the crack growth rate is greatly underestimated.

Furthermore, the authors found that, at low cycling frequency, the hydrogen affected zone is larger than at higher frequencies: this observation is readily explained by the longer time available for diffusion.

Finally, they hypothesize that the mismatch between experimental and numerical results at high pressures may be related to dislocation transport of hydrogen, which needs further investigation, and to the employment of empirical relations which have only been validated for monotonic loads.

The approach of Vasco *et al.* [49] differs significantly from the above-mentioned ones. They modeled the behavior of the aerospace 2024 T3 aluminum alloy from a corrosion point of view, without directly considering hydrogen diffusion and trapping. This model is multi-scale: first, the authors simulated the behavior of a single corroded and embrittled area, named Representative Unit Cell (RUC). This area is shaped like a cube with a truncated cone hole, and it is composed of the bulk material and three different Hydrogen Embrittled Zones (HEZ), which feature degraded stress-strain curves. The position of these HEZ was chosen according to nanoindentation tests. Successively, the degraded elements are randomly placed in the specimen according to the observed pit density.

In order to account for failure, the maximum strain criterion was employed, abruptly decreasing the elastic modulus of the failed elements. In this way, the authors were capable of obtaining the stress-strain curves of the embrittled material, after different exposure times. In particular, they compare the elongation to failure with both the experimental one and the value obtained in a previous work [50], which considered the presence of pits but neglected the effect of hydrogen: the results clearly indicate that this approach is capable of correctly predicting the experimental behavior, with a much lower error compared to the previous work.

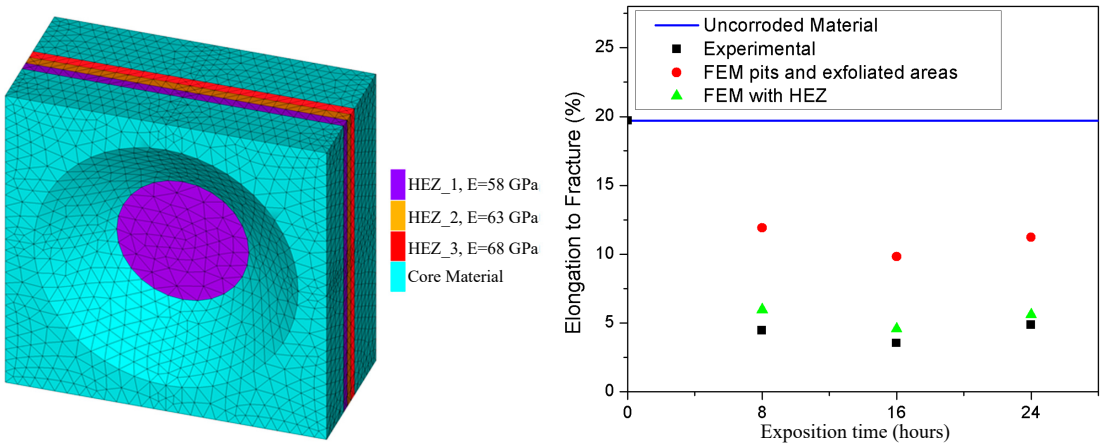

(a) Meshed model of the Representative Unit Cell, with the three Hydrogen Embrittled Areas.

(b) Plot of the elongation to failure versus exposition time, comparing present and past work with the experimental results.

Figure 1.11: From Vasco [49].

1.3 Maraging steel

The term maraging steel refers to a group of ultra-high strength martensitic steels, featuring low carbon and high nickel contents. The term *maraging* comes from the contraction of *martensite* and *aging*: indeed, these steels are hardened by intermetallics precipitation, occurring during aging treatments, rather than carbides. As a result, they exhibit an excellent combination of high strength and good toughness. In addition, the low carbon content confers excellent machinability and weldability, which is exploited in additive manufacturing. The collection of these properties make maraging steels a top choice in the aerospace and automotive industries, as well as for the fabrication of moulds and dies.

The development of maraging steels, initiated in the '60s with the work of Decker *et al.* [51], led to the spread of 18% Ni steels, usually designated by a number (200, 250, 300, 350) which indicates the yield stress in ksi (1400 to 2400 MPa). Other than Ni, the common alloying elements include Co, Mo, Ti and Al.

1.3.1 Hardening mechanisms

In order to achieve precipitation, the material has first to be fully solubilized in the austenitic zone, in the temperature range between 800 and 900 °C. Subsequent cooling occurs, resulting in a supersaturated solid solution, formed primarily by lath martensite with an elevated dislocation density, which can be indexed as a Body Centered Cubic (BCC) material [52, 53]. In fact, the choice of 18% Ni ensures that the martensite finish temperature (M_f) lies significantly above room temperature: as a consequence, martensite is produced even with slow cooling, allowing the processing of large sections [54].

During aging, a number of phenomena can occur, depending on the specific combination of processing time and temperature. Below 450 °C, S, μ and X phases (Table 1.2) are formed; the investigation about these phases is limited, as they are not strongly relevant to the overall material strength [55]. Successively, above 450 °C, one can observe the creation of Ni_3(Ti,Mo); the shape of this precipitate can be either rod-shaped or ellipsoidal, approximately with a width of 5 nm and length of 10-20 nm. Proceeding with time, this metastable Ni-rich phase is dissolved back in the matrix, with subsequent Mo-enriching: the spherical Fe_2Mo then precipitates, with a contribution to strength lower than the Ni_3(Ti,Mo) one.

At higher temperatures, the Ni-rich phase dissolution and Fe_2Mo precipitation lead to Ni enrichment of the matrix, causing austenite nucleation. This phenomenon, named austenite reversion, contributes to the softening of the material (overaging), limiting its service temperature [57]. Reverted austenite is formed by a diffusion-controlled reaction

$$\alpha' \rightarrow \alpha + \gamma, \tag{1.19}$$

being α' the martensitic matrix, α a low Ni phase and γ is the Ni-rich austenite. The influence of reverted austenite on the mechanical properties depends on its volume fraction. Even though the retention of a small quantity of austenite at

Phase	Stoichiometry	Crystal structure	Lattice parameters
γ		FCC	$a = 3.5852$ Å
α		BCC	$a = 2.8812$ Å
μ	A_7B_6	rhombohedral	$a = 4.751$ Å $\alpha = 30.38\,^\circ$
ω	A_2B	hexagonal	$a = 3.9 - 4.05$ Å $c = 2.39 - 2.48$ Å
S	A_8B	hexagonal	$a = 7.04$ Å $c = 2.48$ Å
X	A_3B	hexagonal	$a = 2.55$ Å $c = 8.30$ Å
Fe_2Mo	A_2B	hexagonal	$a = 4.75$ Å $c = 7.75$ Å
Ni_3(Ti,Mo)	A_3B	hexagonal	$a = 5.10$ Å $c = 8.31$ Å
Ni_3Mo	A_3B	orthorombic	$a = 5.06$ Å $b = 4.22$ Å $c = 2.48$ Å

Table 1.2: Phases observed in a maraging steel (from [56]).

grain boundaries has been shown to lead to an increase in toughness [58], its extensive presence affects detrimentally the yield strength; at the same time, overaged particles behave as crack nucleation sites, with a consequent toughness drop [59].

The strength of maraging steel comes from a combination of three contributions, namely the strength of the martensitic matrix, solid solution strengthening and precipitation hardening. Galindo-Nava *et al.* [60] express the overall Vickers hardness and yielding stress as

$$H_v = \frac{1}{3}\sigma_Y = \frac{1}{3}\Big(\sigma_{Mart} + \sigma_{ss} + \sigma_p\Big) \tag{1.20}$$

More in detail, the first contribution is related to dislocation density and the effective grain size:

$$\sigma_{Mart} = 0.25 M \mu b \sqrt{\rho} + \frac{300}{\sqrt{d_{block}}}, \tag{1.21}$$

in which $M = 2.5$ is an orientation factor, μ the shear modulus, b the magnitude of the Burgers vector, ρ the dislocation density and finally d_{block} the block size.

When lath martensite is formed, one can recognize three hierarchically dependent constituents: the austenitic grain is divided into packets, which are groups of laths with the same habit plane; then, each packet is further divided into blocks, *i.e* the laths featuring the same orientation [62]. A representation of this structure is given in Figure 1.12.

Secondly, solid solution strengthening is based on the size difference between the alloying elements. A substitutional atom forms a stress field around its posi-

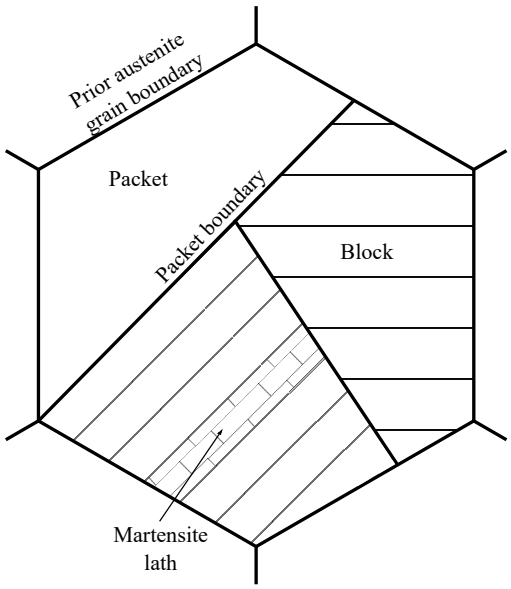

Figure 1.12: The three level hierarchy in lath martensite (adapted from [61]).

tion, whose sign and amplitude will depend on the difference in atomic radii with respect to the solvent atom. This stress field interacts with dislocations, impeding their motion and consequently causing an increase in the yield strength.

Following Fleischer's equation [63], which considers the atomic fraction of the substitutional element in the matrix, $x_{i,\alpha}$, and its strengthening constant, β_i (reported in Table 1.3), one can obtain:

$$\sigma_{ss} = \sum_i \sqrt{\beta_i^2 x_{i,\alpha}}. \tag{1.22}$$

Element	**Ni**	**Mn**	**Al**	**Ti**	**Mo**
β_i (MPa/at)	708	540	196	2628	2362

Table 1.3: Solid solution strengthening constants (from [60]).

It should be underlined that the contribution of the particle-forming elements decreases as the concentration of their intermetallics increase, as these species leave the matrix.

Lastly, the precipitation strengthening mechanism relies on the production of a dispersion of obstacles to dislocation motion, increasing the stress necessary for them to move. The size and distribution of precipitates vary during the aging time: during the first stage, the dispersion is fine and coherent; successively, these particles coarsen, with a continuous loss of coherency, consequently losing the disclocation motion hindering capability. Eventually, the equilibrium structure is formed at long ageing times.

Pereloma *et al.* [64] use a modified form of the Orowan equation for the prediction of precipitation strengthening:

$$\sigma_p = \frac{2\mu b\phi}{4\pi(\Lambda - d)} ln\left(\frac{\Lambda - d}{2b}\right) \tag{1.23}$$

In this equation, ϕ is related to the Poisson's ratio of the matrix, ν, as $\phi = \frac{2-\nu}{2(1-\nu)}$, d represents the average particle size and Λ is the interparticle spacing. According to this model, dislocations bow around the precipitates, leaving loops after their passage; as deformation proceeds, more loops are formed around a particle, increasing the stress needed for subsequent dislocations to move around it. An illustration of this mechanism is offered in Figure 1.13(a).

Solving the kinetics equations as a function of time and considering Equations 1.21 to 1.23, it is possible to plot the trend of hardness during aging, which can be seen in Figure 1.13(b). The graph illustrates the above-mentioned consideration according to which at small aging times, the solutes depletion due to precipitates causes a drop in the solid solution hardening contribution. At any rate, it can be observed that the precipitates contribution is significantly higher than both solid solution and lattice ones.

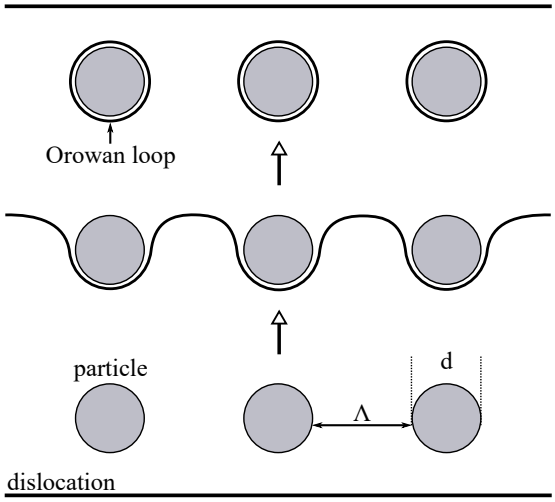

(a) Orowan mechanism.

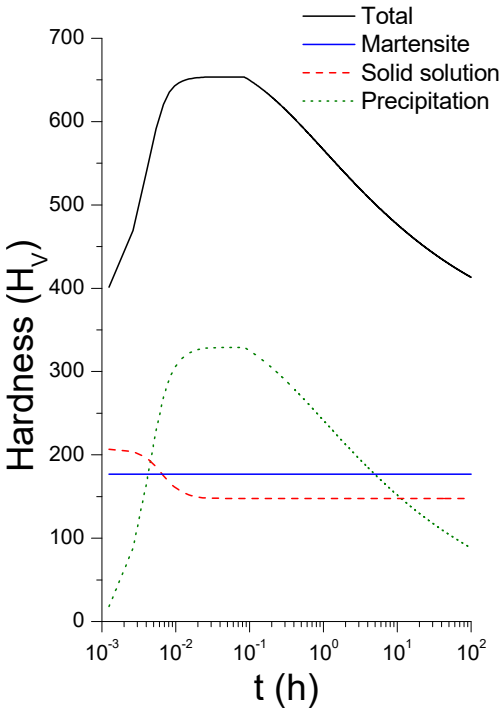

(b) Hardness trend as a function of time in a M350 maraging steel at 540° C (from [60]).

Figure 1.13

1.4 Additive Manufacturing

AM, often referred to as Rapid Prototyping (RP) or 3D printing, is a term grouping a variety of production processes, regarding all classes of materials: in fact, even though AM was historically first developed for polymeric materials, nowadays also composites, metals and ceramics can be 3D printed.

The common feature is the realization of 3D objects starting from a Computer Aided Design (CAD) model; this file is virtually sliced in layers of finite thickness, obtaining the *.stl* (from *STereoLitography*) file, which describes the surface of the object using only small triangles. It is then read by the machine, which will build up the component completing one layer at a time. The procedure inevitably introduces a certain error, consequence of building an object by sections with a finite thickness: both quality and precision will obviously improve with thinner layers [65]. Once the fabrication is completed, the part is removed and subject to post-process treatments, such as cleaning, stress-relieving or Hot Isostatic Pressing (HIP).

Figure 1.14: Steps in the fabrication of an AM part (from [66]).

In recent years, AM has drawn the attention of both the industrial and the academic world. This interest is especially due to its shape and design freedom: in particular, AM allows obtaining lattice geometries, internal channels, as well as customizing the product, since no die, mold or punch is needed. Also, the field of topological optimization increased in popularity, exploiting the possibility of adding or removing material exclusively where needed, fulfilling the double goal of increasing the mechanical performance of the part while decreasing its weight. Last but not least, AM strongly reduces material waste when compared with tra-

ditional subtractive processes. Consequently, AM can be regarded as a sustainable production system, also thanks to its low energy consumption and the possibility of reducing the carbon footprint by means of design optimization [67].

Even though AM offers a plethora of advantages, some drawbacks still limit its spread: among them, we recall the slow deposition rates, the small build volumes and the relatively high cost of materials. As a consequence, AM is currently employed for the production of high-performance components in the most advanced fields, such as aerospace, automotive and energy (Table 1.4). For instance, in the aerospace and automotive industries, where the weight reduction represents a critical issue, AM has enabled manufacturing complex cross-sections, like the honeycomb cell, capable of strongly decreasing the weight-to-strength ratio. Also the medical field is taking advantage of AM, which offers an excellent tool for the production of prostheses for bone replacement, even enabling obtaining a porous structure that mimics the actual bone [68].

	Al	Maraging steel	Stainless steel	Ti	Co-Cr	Ni super alloys	Precious metals
Aerospace	✓	✓	✓	✓	✓	✓	
Medical			✓	✓	✓		✓
Energy, oil and gas		✓	✓	✓		✓	
Automotive	✓		✓	✓		✓	
Marine			✓	✓		✓	
Tools and molds		✓	✓				
Consumer products	✓		✓				✓

Table 1.4: Applications of common additive manufacturing alloys (from [69]).

Regarding hydrogen service, AM could be employed in the state-of-the-art applications; among the components, we recall valves, vessels, fittings, pumps and blowers. The research in this field is pushed by the fact that the possibility of employing a manufacturing technology which guarantees both low costs and hydrogen service reliability is crucial, in order to allow for the use of hydrogen as a safe energy vector [70, 71].

1.4.1 AM processes

Talking about metals, two families of AM processes can be distinguished. In Powder Bed Fusion (PBF), the metal powder is spread on an area of finite size, the bed, and an energy source scans the surface following a pattern set by the *.stl* file. After one layer has been scanned, the platform supporting the bed is lowered by a distance corresponding to the layer thickness, the powder stock distributes new powder on the bed and the process is repeated. The energy source can either be a laser, as in Selective Laser Melting (SLM) or an electron beam, as in Electron Beam Melting (EBM).

Instead, in Directed Energy Deposition (DED), the solid material is directly fed to work site, where it is melted by means of the energy source. It is mainly

employed for the production of large parts, and it allows repairing or adding new features to an already existing object. In Table 1.5 a comparison of the available processes is presented.

Process	DED			PBF	
Feedstock	Powder	Wire		Powder	
Heat source	Laser	E-beam	Electric arc	Laser	E-beam
Nomenclature	DED-L	DED-EB	DED-PA	SLM	EBM
Power (W)	100-3000	500-2000	1000-3000	50-1000	
Speed (mm/s)	5-20	1-10	5-15	10-1000	
Max. build size (cm x cm x cm)	200 x 150 x 75		500 x 300 x 100	50 x 28 x 32	
Production time	High	Medium	Low	High	
Dimensional accuracy (mm)	0.5-10	1.0-1.5	Intrincate feratures are not possible	7-20	

Table 1.5: Comparison between AM processes, adapted from [69].

The feedstock material is typically in the form of powder, due to the ease of feeding and the possibility of charging a fixed ratio of different alloys, so to obtain a composition and property gradient. The powder production process is found to be of uttermost importance, since it determines the oxidation susceptibility and the flowability. For laser processes, the typical powder particle diameter lies in the range $10 - 60$ µm. Among the manufacturing processes, we recall:

- Gas Atomization (GA), in which the flow of Ar or N_2 atomizes the molten metal;
- Rotary Atomization (RA), featuring a rotating disk, radially expelling fine droplets of the molten metal;
- Water Atomization (WA), where a high-pressure water jet atomizes and solidifies the molten metal droplets;
- Plasma Rotating Electrode Process (PREP), melting the end of a rotating metal bar by means of an electric arc and collecting the particles ejected by the centrifugal force.

Even though PREP allows obtaining fine spherical particles with a uniform size distribution, the production process entails high costs. Consequently, the trade-off between powder production cost and bed properties has to be considered when choosing the manufacturing process [69].

Talking more in detail about SLM, a fine powder is introduced in the chamber, which is filled with a protective gas (N_2 or Ar) to prevent oxidation. The powder is typically preheated, in order to decrease the needed laser power and the harshness of the thermal cycle [73]. On top of the powder bed a laser scans the surface in the $x - y$ plane, while the motion in direction z is controlled through a piston below

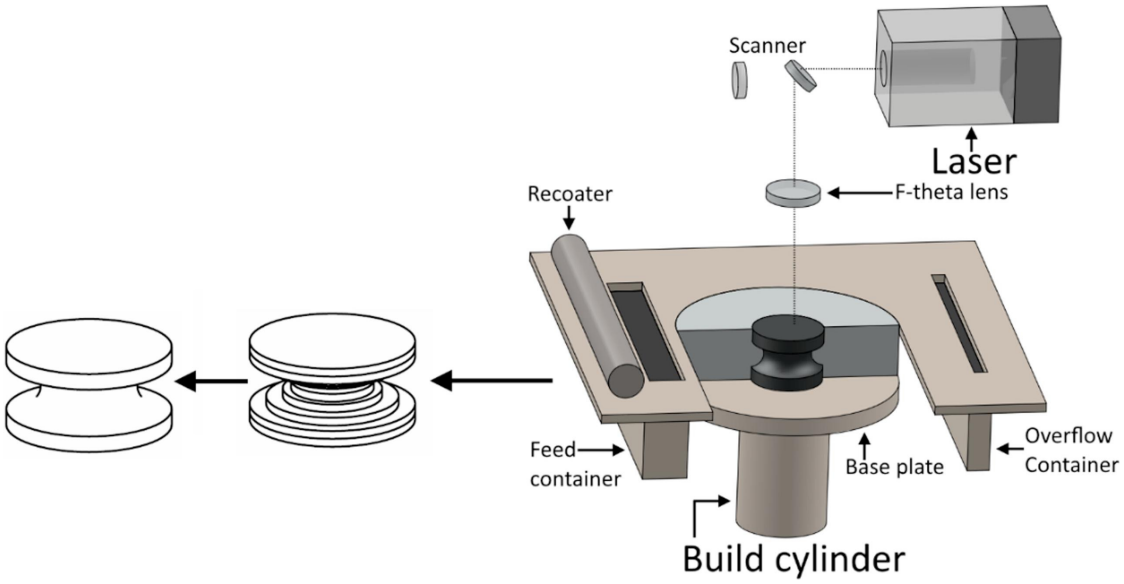

Figure 1.15: Working scheme of the SLM process (from [72]).

the powder bed. The laser beam is deflected by means of galvano-mirrors, and convoyed to the powder bed through a $f - \theta$ lens, in order to have a uniform spot size on the $x - y$ plane, avoiding defocusing because of the different optical path length. The laser photons energy is transferred to the powder particles, creating the melt pool; then, as the laser moves further, the melt region rapidly solidifies and cools down. In Figure 1.15 one can observe the principal components of a SLM system; in addition to the already mentioned ones, it shows the recoater, the feed contained and the overflow container, necessary for the replenishment of the powder after a layer is completed.

Among the benefits of SLM we recall the comparatively low cost and the capability of manufacturing near net-shaped components and hanging parts, by means of proper supports. Furthermore, the cooling rate happens to be faster with respect to EBM, which allows to obtain a finer microstructure, resulting in improved strength and tribological properties [74]. Regarding the cons, SLM is slow, when compared with the other available AM processes, and requires finishing operations to reach an acceptable surface quality.

1.4.2 Residual stresses in AM

Residual Stresses (RS) are defined as *"stresses that remain inside a body that is stationary and at equilibrium with its surroundings"* [75]. In metals, they are originated by inhomogeneous plastic deformation, which can be mechanically or thermally induced. RS may be introduced by purpose in the material, typically to create a compressive stress field on the surface, which increases the material resistance to crack initiation. An example is represented by shot peening, where the part surface is stricken by a flux of hard particles moving at high velocity.

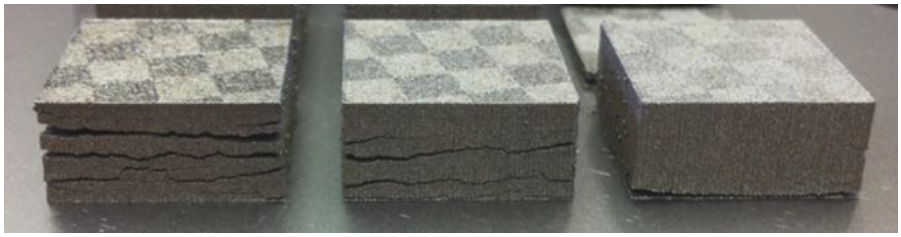

Figure 1.16: Cracks in SLM produced M2 High Speed Steel, with increasing scan speed from left to right (from [78]).

RS are classified depending on the length they act on. More specifically, type I residual stresses are active on the whole body, and they are therefore named as macroscopical RS. Secondly, type II refers to stresses arising between neighboring grains because of their different orientations and subsequent mesoscopic anisotropy. Lastly, type III stresses act on an atomic level, being created by intragranular defects, such as dislocations, vacancies or solute atoms [75].

The magnitude and distribution of residual stresses in a material due to a thermal cycle depend on a variety of material properties; indeed, other than the thermal and mechanical parameters, also the effect of allotropic transformations should be taken into account. First, the general relation between strain and temperature variation is described by

$$\begin{bmatrix} \epsilon_{11} & \epsilon_{12} & \epsilon_{13} \\ \epsilon_{21} & \epsilon_{22} & \epsilon_{23} \\ \epsilon_{31} & \epsilon_{32} & \epsilon_{33} \end{bmatrix} = \begin{bmatrix} \alpha_{11} & \alpha_{12} & \alpha_{13} \\ \alpha_{21} & \alpha_{22} & \alpha_{23} \\ \alpha_{31} & \alpha_{32} & \alpha_{33} \end{bmatrix} \cdot \Delta T, \tag{1.24}$$

where α_{ij} are the coefficients of thermal expansion. Residual stresses are generated by the fact that ΔT is not constant throughout the material, but a gradient ∇T is present.

Additionally, transformation strains are to be considered. A transformation can occur in two main ways. The reconstructive mechanism features solute and solvent atoms undergoing uncoordinated diffusion, resulting in an isotropic volume change, which may create residual stresses if the material is constrained. Conversely, in the displacive one, in which the new structure arises from a rapid distortion of the parent lattice, both dilational and shear strains are created. A displacive transformation can be influenced by the residual stresses already existing in the material; in fact, variants in which the transformation strain is opposed to the already existing one will be favored. In other words, displacive transformations may be a way to lower residual stresses [76, 77].

In AM, stresses are repeatedly built up on a small scale, and their superposition gives the final macroscopic RS field. Several research studies have been conducted to model the formation of the melt pool and the temperature field around it [79–81]. The evaluation of residual stresses is a complex task, being strongly dependent on the material properties and tendency to form new phases and on the processing parameters, such as the scan speed, the laser power, the hatch spacing, the powder

particle size and the layer thickness. In order to alleviate the intensity of residual stresses and homogeneize the as-built structure, AM parts are normally subjected to a heat treatment before usage [82].

1.4.3 Microstructures of AM maraging steel

The microstructure of AM produced 18Ni-300 has been extensively investigated. Conversely to the conventionally produced features described in Section 1.3.1, the material obtained by both SLM and DED shows a cellular/dendritic solidification microstructure [83–86]. The lath martensite blocks are shown to be often confined to a single dendrite, because of retained austenite at cell boundaries. Due to the inhomogeneous cooling rate, which is maximum at the boundary of the molten pool, segregation happens, as visible in Figure 1.17. In particular, Ni segregates at grain boundaries; as a result, being Ni an austenite stabilizer element, a significant fraction of retained austenite (6-11%) can be found [83, 87, 88]. Also, several authors report that in SLM the formation of lath martensite is prevented by the high cooling rate [89–91].

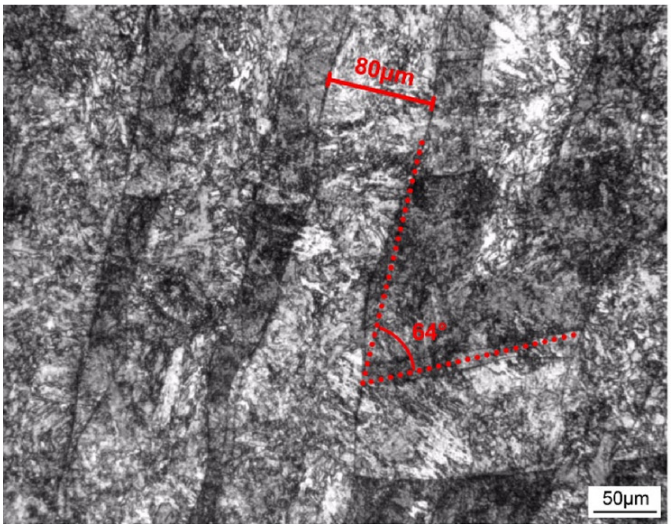

Figure 1.17: Microstructure of 18Ni-300 maraging steel produced by SLM after etching (from [87]).

Figure 1.18 shows the evolution of the microstructure with aging. Increasing the aging temperature from 390 °C to 590 °C, the cell boundaries become thicker, initially because of Ni_3Ti, Ni_3Mo and Ni_3Al precipitation at 490 °C, and then because of massive austenite reversion at 590 °C, leading to an austenite volume fraction of more than 60% [87].

The cellular microstructure is erased after a solution treatment, typically conducted in the 815-840 °C range, and gets substituted by a fully martensitic structure after quenching [84, 85, 92]. As investigated by Jägle *et al.* [86], the as-built precipitate population differs depending on the AM process. When SLM is employed, no precipitates are present, because of the higher scan speed and smaller

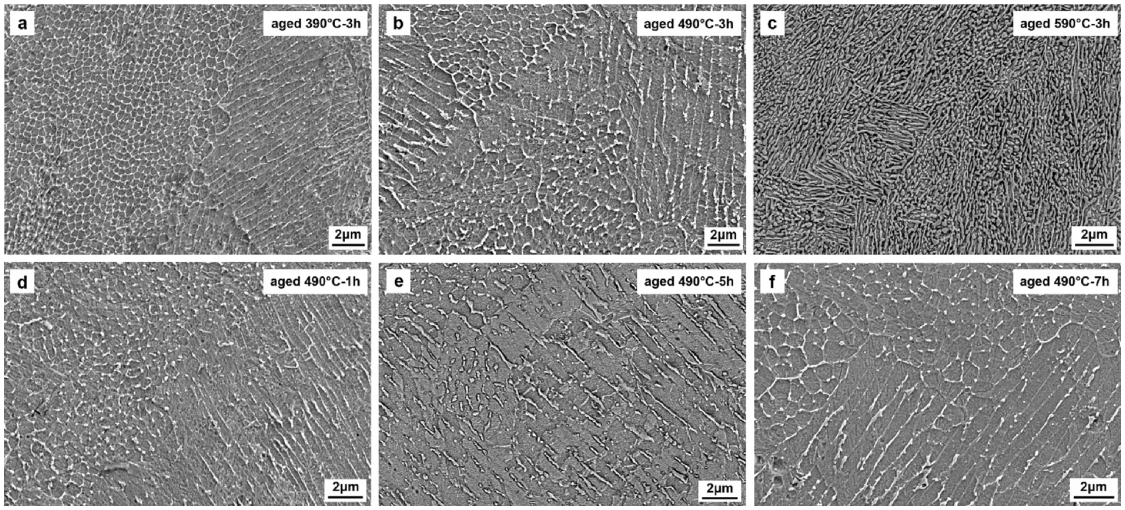

Figure 1.18: Evolution of the microstructure of 18Ni-300 maraging steel produced by SLM with aging (from [87]).

melt pool. On the other hand, with DED, the hardness results higher, because of small clusters of atoms, which are typical of early stages of precipitation. The reason for this phenomenon is connected to the repeated re-heating of the already deposited material, caused by the deposition of the subsequent layers. In fact, this DED hardness increase can not be found on the top layers, which do not experience re-heating. The authors name this condition Intrinsic Heat Treatment (IHT), and believe it might be exploited for the design of a maraging steel that would not need an aging treatment, as it would be fully *in-situ* strengthened.

1.4.4 State of the art of HE in AM

Given the novelty of Additive Manufacturing and the complexity of Hydrogen Embrittlement, little research has been conducted up to present.

Kwon *et al.* [93] investigated the behavior of 18Ni-300 maraging steel produced by SLM. They analyzed the effect of HE on samples exposed to two levels of hydrogen charging, and with different thermal treatments. In particular, they compared the as-built, solution treated, as-built + aged and solution treated + aged conditions.

The results of the tensile tests are shown in Figure 1.19; even though this kind of test is not the standard in HE investigation, the slow strain rate (10^{-5} s^{-1}) guarantees the observability of the detrimental effect. They found out that solution treatment dramatically improves the HE resistance of the material, obtaining overlapping curves for the uncharged and charged specimens. This effect is attributed to the reduction of dislocation density, acting as trapping sites, and of retained austenite, which offers a higher solubility to hydrogen; in fact, as-built specimens released more hydrogen upon a thermal desorption measurement. Conversely, the loss in ductility, in terms of strain to failure ϵ_f, becomes very severe after aging, no matter whether the sample had previously been solution treated or not. This

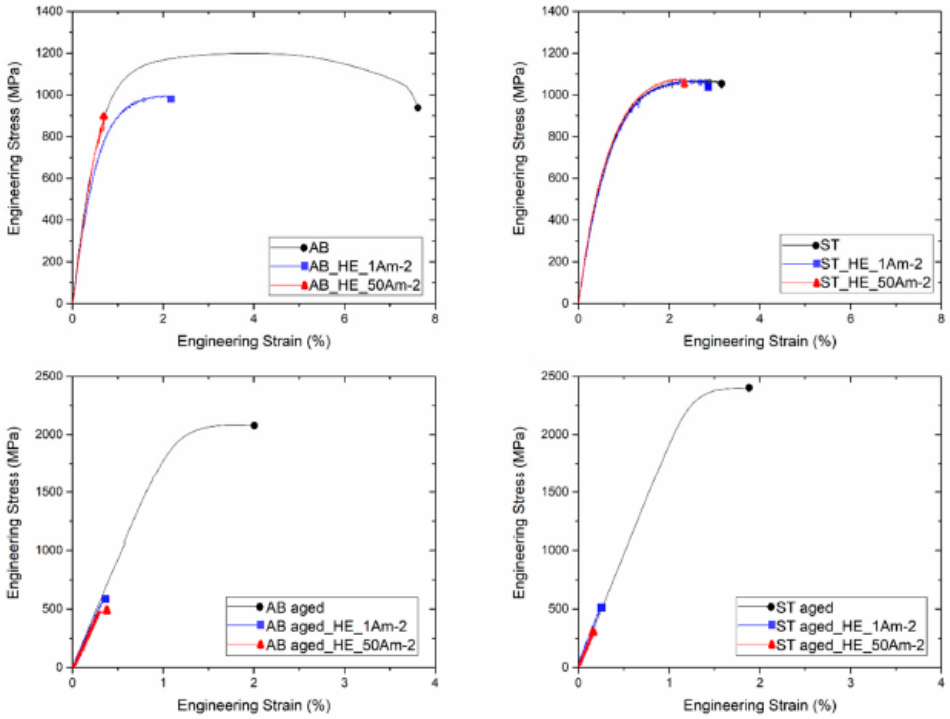

Figure 1.19: Stress-strain curves of hydrogen-charged 18Ni-300. The strain rate is equal to 10^{-5} s^{-1}. From [93].

embrittlement effect is believed to be due to the precipitation of intermetallics such as Ni_3Ti, Fe_2Mo and Fe_7Mo_6, which act as additional hydrogen trapping sites.
Regarding the specific influence of the SLM process on the HE behavior, the authors state a comparison with experiments on traditionally obtained samples is troublesome, because of differences in H-charging conditions, testing environment and chemical composition.

A different material was tested by Baek *et al.* [70]: the authors investigated the behavior of stainless steel AISI 304L obtained by DED sintering, and compared it with the one of specimens cut from a rolled plate.
The resulting stress-strain curves of the AM samples show a significant improvement in the resistance to HE. In fact, the rolled specimens pass from a strain to failure of 62.3% to 19.2% after hydrogen exposure; conversely, AM samples only show a ϵ_f reduction of 5%, from 64.3% to 59.1%. Also, the fracture surface of the DED samples showed dimples, regardless of the atmosphere; in contrast, the rolled plate ones pass from a cup-and-cone surface to a cleavage one. The reason is attributed to the creation of a fine and dense secondary grain boundary fused phase throughout the specimen, which leads to stress relaxation and energy dissipation.
To the authors' knowledge, this is the first observation that the manufacturing process affects the sensitivity of a steel to HE.

Lastly, Li *et al.* [94] studied the influence of hydrogen on DED-manufactured IN 718 nickel-based superalloy. The authors took into account the influence of the

building direction: in fact, other than an extensive study of the microstructure, they compare the stress-strain curves of as-deposited samples built with the thickness parallel and vertical to the z direction, designated as HP and VP, respectively. The authors underline the observation of partial serrations in the σ-ϵ curve of the as-deposited hydrogen-charged HP sample, which is believed to be related to the hydrogen dragging effect on dislocations. However, the reason why these serrations could not be observed in VP samples is still not clear.

Additionally, the effect of thermal treatment (homogenization + aging) on the HP samples is reported. The Hydrogen Embrittlement Index (HEI), defined as the percentage variation of the strain to failure between uncharged and charged conditions, depends on the testing conditions: it moves from 23% for the as-built VP sample to 37.4% for the heat-treated HP one, passing through 27% if the material is processed in the horizontal plane and tested as-built (HP). The premature failure of the alloy is attributed to a synergistic effect of both HEDE and HELP mechanisms.

Chapter 2

Experimental

2.1 Materials and methods

2.1.1 Specimen manufacturing

The SLM printing process has been conducted by the National Council of Research at ICMATE, in Lecco. The employed machine is a Renishaw AM 400 (Figure 2.1), whose features are reported in Table 2.1.

Build area X × Y × Z	250 mm × 250 mm × 300 mm
Build rate	Up to 20 cm^3/h
Powder layer thickness	20 µm to 100 µm
Laser power	400 W
Laser focus diameter	70 µm
Scanning speed	Up to 2 m/s
Positioning speed	7 m/s
Running Ar consumption	< 50 l/h
Compressed air	Required

Table 2.1: Renishaw AM 400 features.

The M300 maraging steel powder has been purchased from Renishaw, and its chemical composition, according to the datasheet, is reported in Table 2.2. The choice of a high strength steel as the material to be investigated stems from the high sensibility to HE, so that the detrimental effect is more evident.

Ni	**Co**	**Mo**	**Ti**	**Si**	**Mn**	**C**	**P**	**S**	**Fe**
17-19	7-10	4.5-5.2	0.3-1.2	≤ 0.1	≤ 0.15	≤ 0.03	≤ 0.01	≤ 0.01	bal.

Table 2.2: M300 chemical composition, in weight %.

The samples for the tensile characterization of the material have been designed in accordance with the ASTM E8 standard [95]. In order to reduce the powder consumption and the needed force for tensile loading, the sub-sized shape has been chosen. Its geometry and dimensions are shown in Figure 2.2(a).

Figure 2.1: Renishaw AM 400.

Secondly, the samples for toughness testing (Figure 2.2(b)) have been modeled following the testing procedures used at SINTEF laboratories in Trondheim. The notch produces a stress concentration factor of 6.4, which simulates a weld toe undercut [96]. The upper part of the notch has been designed for an easy application of clip-on-gages. The slow rate test specimen (Figure 2.2(c)) features a geometry much similar to the notched one, with the resistant cross-section being the same, *i.e.* a 5 mm edged square. The choice of toughness testing as a HE investigation method is well supported by literature [21, 40, 97]

The dimension of the specimens has been chosen in order to be able to reach complete failure with the available 100 kN load cell even in the most resistant material scenario: in fact, the Renishaw datasheet indicates a 1800 MPa Ultimate Tensile Strength (UTS) after age hardening, while the study of Kwon *et al.* [93], conducted on 18Ni-300, reports a UTS of 2400 MPa after solution treatment and aging.

The drawings show the final sizes, after the removal of the 1 mm allowance, which has been added everywhere to allow polishing. The notch has to be machined after the printing by Electro Discharge Machining (EDM). Lastly, nine little cubes of 6 mm in edge were printed in order to conduct hydrogen absorption measurements.

The building platform was preheated to 170 °C, as reported on the provider's guidelines. The preheating reduces the harshness of the thermal cycle; moreover, the printing parameters were optimized in order to deliver the correct energy amount starting from this temperature. The samples were printed along the horizontal direction, *i.e.* with the smallest dimension along the z-axis, in order to reduce the needed powder.

Successively, all the samples have been thermally treated, in order to alleviate

the stresses due to the manufacturing process and allow the intermetallics precipitation. In particular, the treatment consisted of aging at 540 ° C for 1 hour. The choice of the aging treatment was based on the study of Casati *et al.* [88], as a good compromise between peak stress and strain to failure. With the aim of highlighting the HE effect, a relatively large initial ductility is needed, in order to better appreciate its drop. In fact, the chosen time-temperature combination offers the larger ductility among the investigated ones [88].

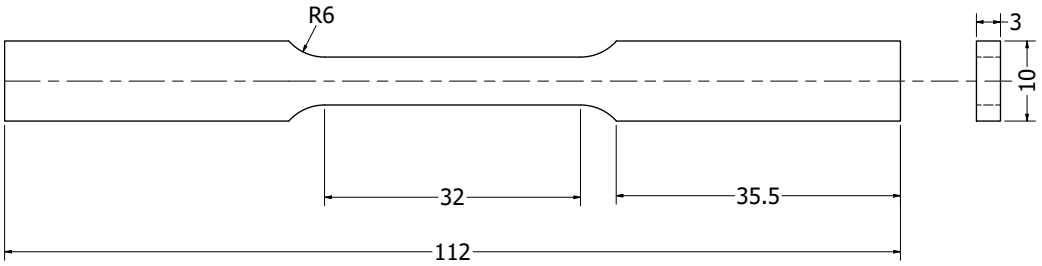

(a) Tensile specimen

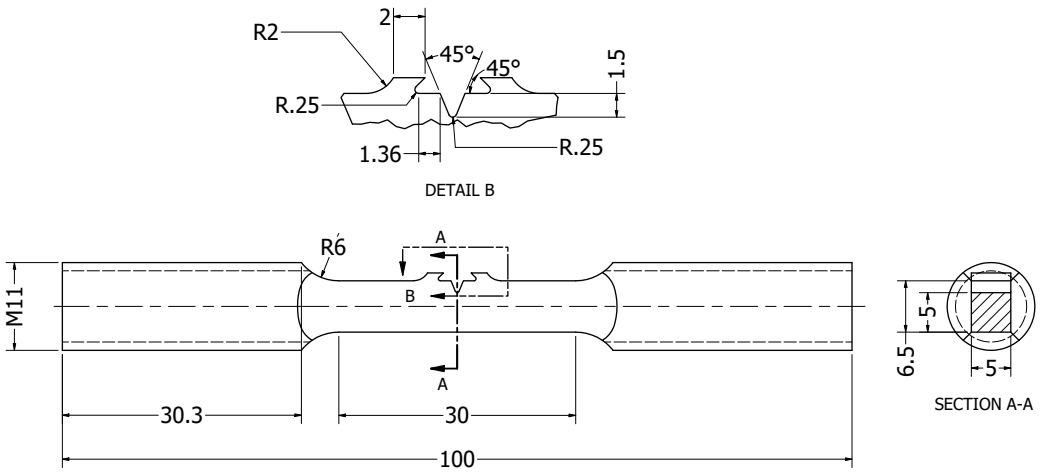

(b) Single Edge Notch Tension (SENT) specimen

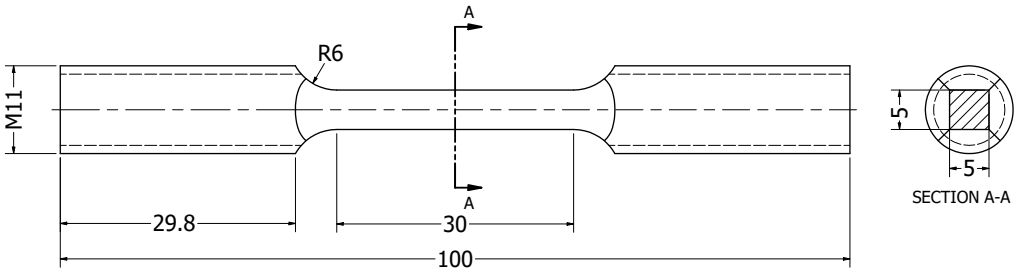

(c) Slow strain rate specimen

Figure 2.2: Specimen geometries.

2.1.2 Mechanical characterization

The tensile characterization of the samples, aimed at obtaining the uni-axial stress-strain curve, has been conducted at CLASD labs in Politecnico. For the test, a MTS Alliance RT 100 with a 100 kN load cell was employed. Other than the samples printed preheating the base, labelled as **P**, 2 samples obtained without preheating, labelled as **RT**, were tested, in order to check the effect of the preheating. In order to directly measure the strain, a MTS extensometer was used. The displacement speed was set to 1 mm/min.

The CTOD-Δa curve, necessary for the calibration of the numerical model, and for the prediction of the steel behavior in presence of hydrogen, can be obtained experimentally from the toughness test. Following a procedure similar to the one reported ASTM E1820 - 09 standard [98] (recalling that the employed specimen is not the standard one), the specimen is loaded uniaxially, measuring the Crack Mouth Opening Displacement (CMOD) by means of a clip-on-gage. This value is used, together with the continuous measurement of the force *vs* load-line displacement curve, in order to calculate the toughness quantity, *i.e.* J, K or CTOD. The standard provides all the formulas, which depend on the specimen geometry, starting from the CMOD and the specimen elastic compliance. In the case of a non-standard SENT specimen, the adequate formulas are found in literature [99].

Conversely to the original test planning, it was not possible to perform the toughness test, due to the delay accumulated during the several steps (powder purchasing, printing, heat treatment, EDM cut from the base plate, shipping, machining, pre-cracking) necessary to have the samples ready to be tested by our partners at NTNU (Trondheim). This delay in the experimental part was completely due to the CoViD-19 lockdowns in different countries, at different times. Initially, the metal powder could not be purchased due to the suspended activity in China; successively, the printing stage was greatly delayed by the Italian closure; lastly, the lab activity in Trondheim was markedly slowed-down due to personnel rotation.

Consequently, it was decided to proceed with the building of the numerical model, employing the CTOD-Δa curve of another martensitic steel, leaving the actual calibration, based on the real maraging data, for the future steps of this project. In particular, we make reference to the data of AISI 4130, whose fatigue and toughness properties were investigated by Colombo *et al.* [100]. In their work, the authors tested single-edge notch C(T) specimens, both in air and after hydrogen charging, obtained electrochemically following the procedure described in [101]. The material properties and composition are reported in Table 2.3 and Table 2.4, respectively.

The polarizing cathodic current employed by [100] was equal to 0.5 mA/cm^2; the charged samples were successively tested in air. In order to consider hydrogen degassing during the test, the authors measured its concentration by means of the hot glycerol method, reporting a hydrogen concentration after 5 hours of 1.3 ppm,

Property	Value
Yielding strength	715 MPa
UTS	950 MPa
Young's modulus	220 GPa
J_{IC}, no hydrogen	215.5 N/mm
J_{IC}, hydrogen	22.0 N/mm
K_{IC}, no hydrogen	217.7 MPa$\sqrt{\text{m}}$
K_{IC}, hydrogen	69.9 MPa$\sqrt{\text{m}}$

Table 2.3: AISI 4130 mechanical properties (from [100]).

C	Mn	Si	Cr	Mo	Fe
0.30	0.50	0.25	0.95	0.20	bal.

Table 2.4: AISI 4130 chemical composition, in weight % (from [100]).

confirming hydrogen presence in the specimen for the whole test duration.

2.1.3 Microstructure and fracture surface

The cubes for hydrogen measurement, described in Section 2.1.1, were employed for the observation of the surface appearance. Initially, the samples were observed with a Scanning Electron Microscope (SEM), produced by Oxford Instruments, with no surface preparation.

Successively, the samples were prepared, in order to be able to observe the microstructure, removing the surface defects and oxides. First, the cubes were cold mounted in the epoxy resin Technovit® 4071, for easier handling. Later, the samples were polished with a progressive mesh size of 320-600-800-1200 and 2500 dots/in^2, and finally with cloths on which diamonds of 6-3-1 µm were sprayed. Finally, the microstructure was highlighted by etching in Nital 2% v/v (HNO_3 in ethanol) for 20 s, and observed at the Leitz Aristomet optical microscope.

The tensile sample **P2**, tested in Section 2.1.2, was observed at the SEM, in order to obtain information about the fracture surface.

2.1.4 Microhardness and density

In order to characterize the material from the hardness point of view, microhardness tests were executed. The employed instrument is a Leitz Miniload 2, equipped with a 200 gf Vickers indenter. After having pressed the indenter to the surface for 10 s, the resultant indent is observed at the optical microscope. The software allows the calculation of the microhardness values selecting the position of the indent vertices. A total of 5 measurements were carried out on the polished xy surface of a hydrogen measurement cube.

Parts produced by Additive Manufacturing present, in general, a lower density compared to the same material obtained by subtractive processes. The cause of this phenomenon is found in the presence of porosities in the part, which can have different origins. More specifically, the process nature leads to the possibility of having gas entrapment, both due to the working atmosphere and to the evaporation of low-vaporizing allying elements [102]. Additionally, the choice of the process parameters, particularly the laser power and scan speed, influence the resulting density. In fact, a low power density leads to lack of fusion, while, increasing it excessively, a keyhole is generated, with again the possibility of entrapping gas, namely the plasma [103]. Lastly, the high power density can easily produce spatters of different sizes, which affect density, microstructure and mechanical properties [104].

Among the available methods for additively manufactured parts, the Archimedes one is reported to be the most accurate and repeatable [105]. The procedure consists in weighting the sample in two different fluids, normally air, obtaining m_{air}, and distilled water, acetone or ethanol, obtaining m_l. The choice of ethanol and acetone is particularly advantageous when testing lattice structures, where air bubbles prevent water from filling all the gaps, due to water high surface tension [102].

Neglecting the density of air, the sample density is obtained starting from the equation for the hydrostatic force F for submerged surfaces, *i.e.*

$$F = \rho_l \, g \, V, \tag{2.1}$$

being ρ_l the density of the liquid, g the gravitational acceleration and V the sample volume. In fact, with little calculation one can obtain the sample density, ρ_{sample}, as

$$\rho_{sample} = \rho_l \, \frac{m_{air}}{m_{air} - m_l}. \tag{2.2}$$

The weight measurements were performed with a Gibertini S/2 analytical balance. Initially, dirt and grease were removed from the surfaces of three cubes by immerging them in acetone, using an ultrasonic cleaner for 5 minutes. Successively, they were tested three times each, in air and distilled water, with proper care in removing the air bubbles on the surface. The balance automatically shows the sample density value.

2.2 Results

2.2.1 Mechanical properties

The resulting $\sigma - \epsilon$ curves are shown in Figure 2.3. All the samples behaved similarly, independently on the base preheating, except for the sample P2, which failed at a lower strain value. Other than the samples curves, the figure reports the average curve, computed without considering sample P2, whose behavior was attributed to a printing defect. The most relevant mechanical properties are reported in Table 2.5. The table clearly shows that the material showed a ductility

Property	Range	Average	Reference [88]
Elastic modulus [GPa]	170-184	176 ±6	-
Yield Strength (YS) ($Rp_{0.2}$) [MPa]	1718-1755	1741 ±14	1870
UTS [MPa]	1762-1798	1785 ±14	1957
Strain to failure [%]	2.6-5.9	5.7 ±0.1	2.07

Table 2.5: 18Ni 300 tensile properties.

larger than the one measured in the reference study.

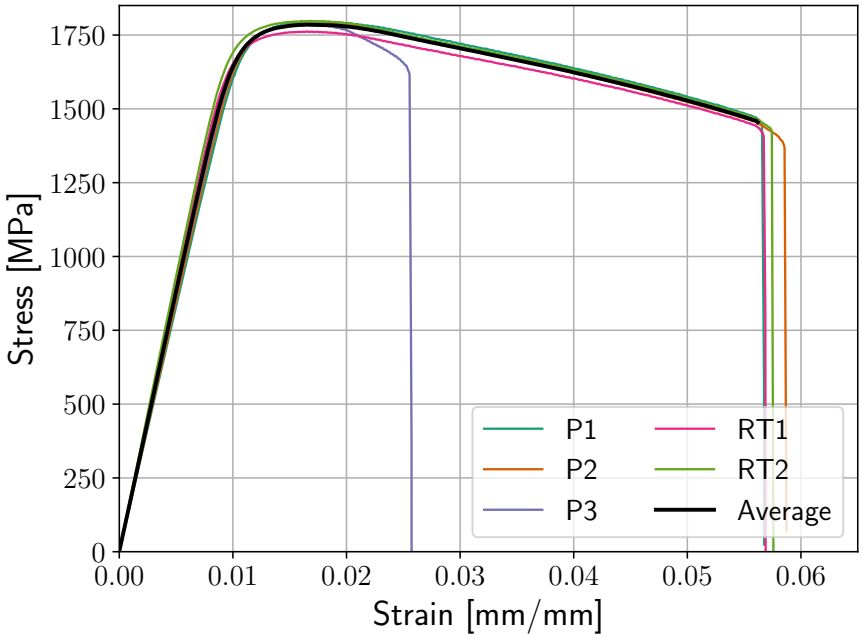

Figure 2.3: Tensile stress-strain curves.

The CTOD-Δa curves of AISI 4130, as obtained by Colombo *et al.* [100], for both as-received and hydrogen-charged conditions are reported in Figure 2.4.

2.2.2 Microstructure and fracture surface

Starting from the unpolished sample, in Figure 2.5(a) the SEM top view, corresponding to the xy-plane (with z being the building direction), is presented. The laser scan lines are clearly visible, with the oxide film, originated during aging, homogeneously covering the surface. On the other hand, Figure 2.5(b) shows the lateral view. Other than the layers sequence, a number of spherical entities are visible. These features correspond to partially melted metal powder particles, which adhere to the surface. In fact, these particles have the same size as the starting powder, in the 20-40 µm range. There is no evidence of melt pool spatters, which normally feature larger diameters (around 200 µm), and a porous structure [106].

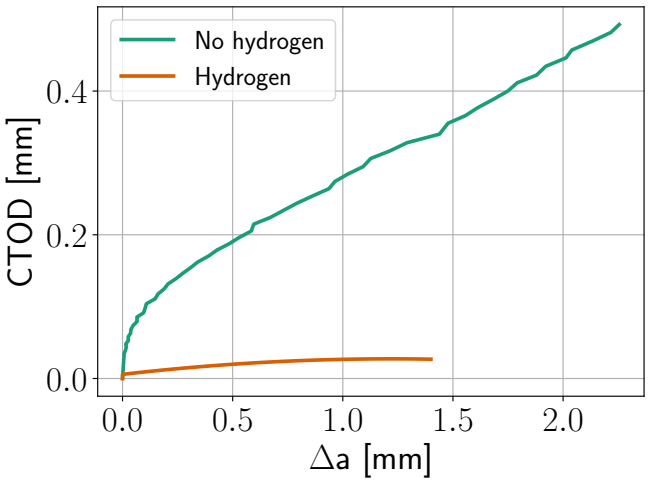

Figure 2.4: AISI 4130 CTOD-Δa experimental curves (from [100]).

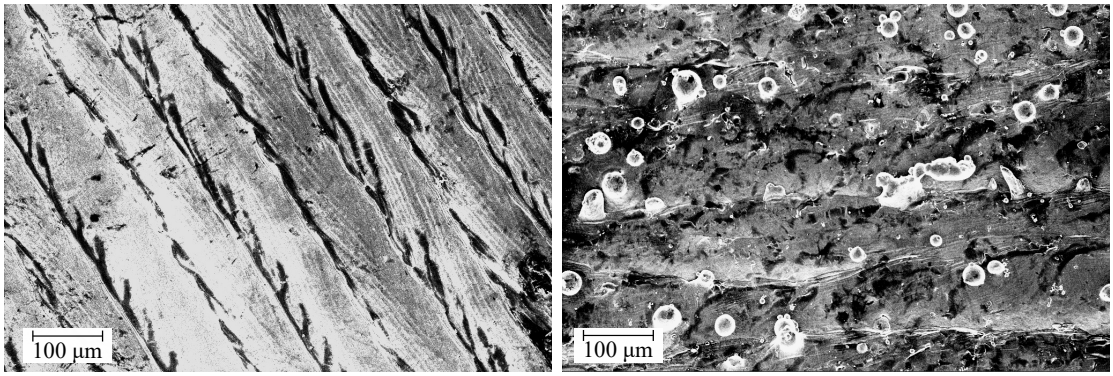

(a) Top view. **(b)** Lateral view.

Figure 2.5: SEM pictures of the unpolished sample.

Moving to the observation of the polished samples at the optical microscope, the top view allows confirming the typical AM maraging microstructure described in Section 1.4.3. The cellular structure, clearly visible in Figure 2.6(b), arising from the fast cooling rate, prevents the formation of lath martensite and of the hierarchical structure. The intercellular spacing is in the 1 µm range, contributing to the excellent tensile and hardness properties. In Figure 2.6(c) the different layers are clearly distinguishable, with a certain degree of downward bending, due to the gravitational attraction on the melt pool. Increasing the magnification up to 1000x (Figure 2.6(d)), the martensite orientation can be seen, together with the retained/reverted austenite (brighter zones).

Lastly, the fracture surface appearance was investigated at the SEM. As shown in Figure 2.7(a), the surface is composed by two different zones. In fact, the top-left area presents a ductile appearance, with void nucleation and coalescence; Casati *et al.* [88] impute the origin of larger voids to pre-existing defects, such as unmelted powder particles and molten splats. On the other hand, the crack, after having nucleated following this ductile mechanism, propagates following a quasi-cleavage

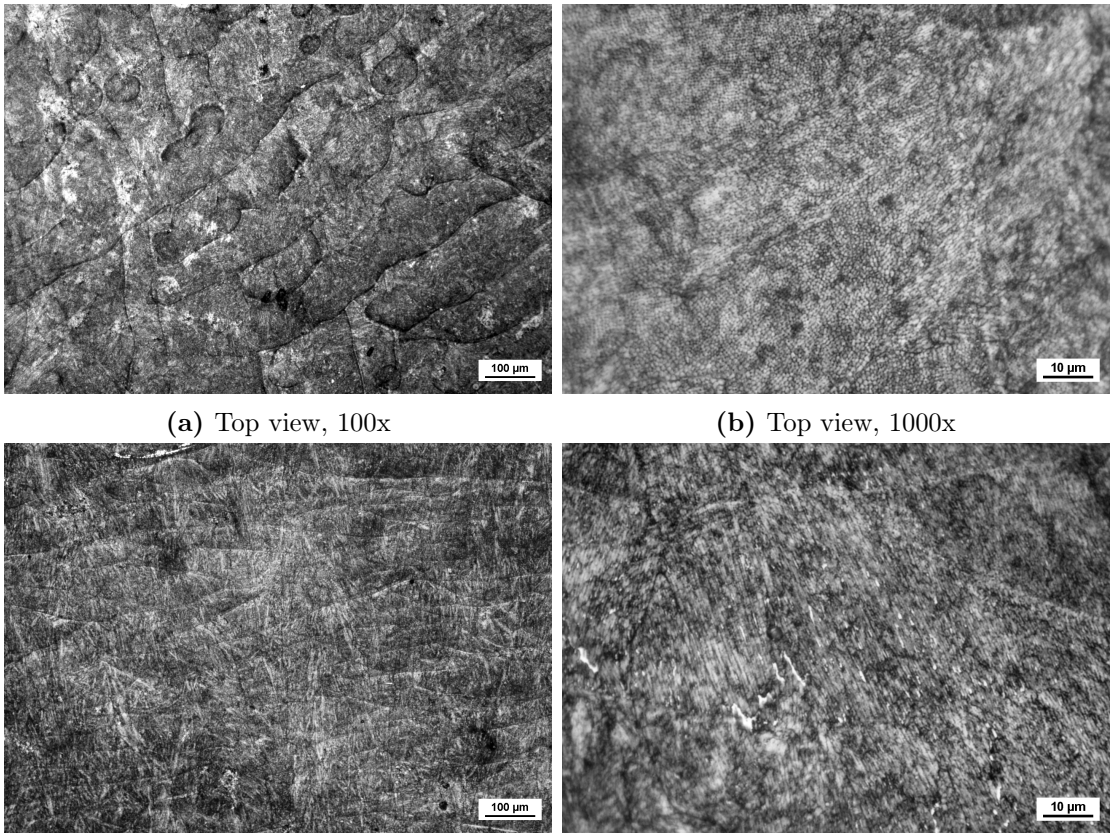

(a) Top view, 100x

(b) Top view, 1000x

(c) Lateral view, 100x

(d) Lateral view, 1000x

Figure 2.6: Optical microscope pictures on the etched samples.

fashion, typical of brittle failure.

At a greater magnification (Figure 2.7(b)), one can notice the characteristic surface of ductile failures, with the larger dark areas corresponding to voids. These cavities lead to the arise of large stresses, provoking the formation of more cavities; they will ultimately coalesce, leading to a fast tear growth [89]. Moreover, the presence of pores (circle on the bottom-center), probably due to gas entrapment during processing, should be highlighted.

2.2.3 Microhardness and density

The results of the microhardness testing are shown in Figure 2.8, obtaining an average value of 587 ± 24 HV. When comparing these values with the experimental findings of Casati *et al.* [88], one can appreciate the confirmation of the expected values. In fact, the authors report a hardness of 570 HV for the peak-aged samples at 540° C.

Table 2.6 summarizes the density measurement results. The high relative density value confirms the correct choice of the process parameters; Kempen *et al.* [89] report a maximum value equal to 99.4%.

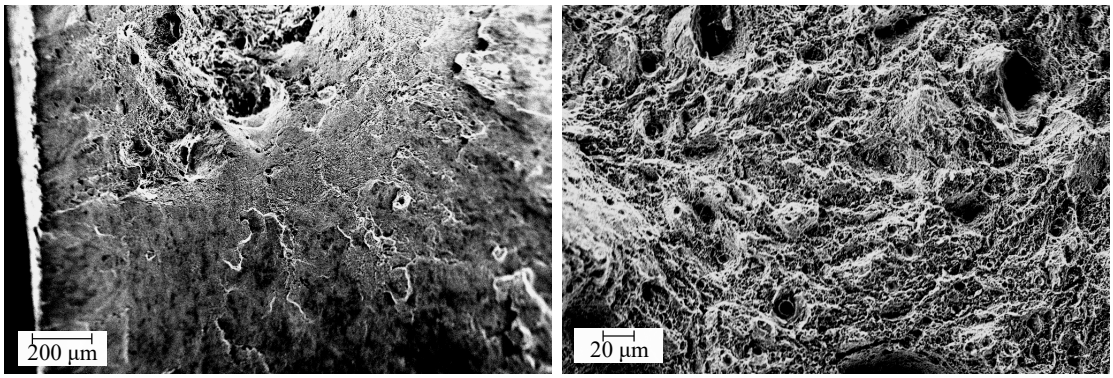

(a) 200x. **(b)** 1000x.

Figure 2.7: SEM images of the fracture surface of sample P2.

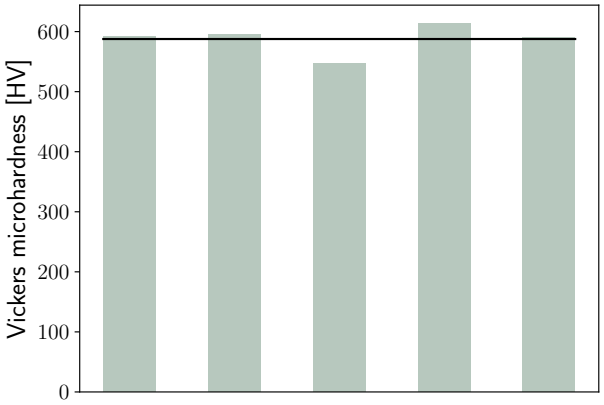

Figure 2.8: Microhardness values.

	Value [g/cm^3]
Range	8.0130-8.0590
Standard deviation	0.162
Average	8.0324
Bulk density	8.1
Relative density [%]	99.2

Table 2.6: Density values

Chapter 3

Numerical model

3.1 Methods

The objective of the numerical analysis was to build a model simultaneously capable of considering:

- the effect of the stress field on hydrogen diffusion;
- the effect of hydrogen concentration on the stress field;
- the variation of hydrogen trap sites due to plastic deformation;
- crack advancement;
- the influence of hydrogen concentration on crack growth.

The analysis was conducted using ABAQUS 2017, properly linked with Microsoft Visual Studio 2012 and Intel Parallel Studio XE 2016; the softwares cooperation is necessary for the compilation of the user-defined subroutines.

The nature of the problem requires a model capable of describing the progressive failure of the specimen and of solving the coupled diffusion-stress equations. The tools used for this purpose are, respectively, the cohesive elements and a set of FORTRAN subroutines, as described in the following.

3.1.1 Material behavior

In order to describe the elasto-plastic behavior of the material, as obtained in Section 2.1.2, in ABAQUS, data has to be elaborated. In fact, for the elastic part the software requires the Young's modulus E and Poisson's ratio ν, set equal to 176 GPa and 0.3, respectively. On the other hand, the description of the plastic behavior can follow several laws. One option is to express it point by point, by means of stress-strain pairs, employing Mises' isotropic hardening. ABAQUS will then interpolate between these given points, obtaining a stress value for any strain.

More specifically, the true stress has to be coupled with the equivalent plastic strain ϵ_p, starting from $\epsilon_p = 0$. It is useful to recall here the difference in the definition of engineering and true stress and strain. The true strain is defined as

$$\begin{aligned} dL &= \epsilon_t \, L \\ \epsilon_t &= log\frac{L}{L_i}, \end{aligned} \tag{3.1}$$

therefore considering the progressive increment in the specimen size, L; conversely the engineering one is referred to the total variation, as

$$\epsilon = \frac{\Delta L}{L_i}. \tag{3.2}$$

The engineering stress, which is normally considered in a tensile test, is computed starting from the applied load, P, and the original cross-sectional area, A_i, as

$$\sigma = \frac{P}{A_i}. \tag{3.3}$$

On the other hand, the true stress does consider the variation of A during the test. Since this area shrinks with an increasing load, the value of the true stress will overcome the engineering one. In fact, in a true stress-strain diagram the tensile curve is always rising, up to failure. Knowing the engineering stress σ-strain ϵ curve, the true strain ϵ_t and stress σ_t can be obtained as [5]

$$\epsilon_t = log(1 + \epsilon) \tag{3.4}$$

$$\sigma_t = \sigma(1 + \epsilon) \tag{3.5}$$

Successively, the plastic part of the true strain is computed simply subtracting the elastic strain, obtained by means of the Hooke's law, *i.e.*

$$\epsilon_p = \epsilon_t - \frac{\sigma_t}{E} \tag{3.6}$$

At this point, it is necessary to interpolate the data following an analytical model, in order to be able to extrapolate the behavior at large strain values, to avoid instability. A very common way to proceed is represented by the Ramberg-Osgood model, in which the elasto-plastic trend is described by a continuous curve as

$$\epsilon_t = \frac{\sigma_t}{E} + \left(\frac{\sigma_t}{H}\right)^{\frac{1}{n}} \tag{3.7}$$

Parameter	**Value**
n	0.0463
H	2332.5 MPa

Table 3.1: Ramberg-Osgood parameters

In the previous equation, H and n are the Ramberg-Osgood parameters, obtained fitting the plastic strain, ϵ_p, and the true stress, σ_t, in a double logarithmic plot, *i.e.*

$$log(\sigma_t) = n \; log(\epsilon_p) + log(H) \tag{3.8}$$

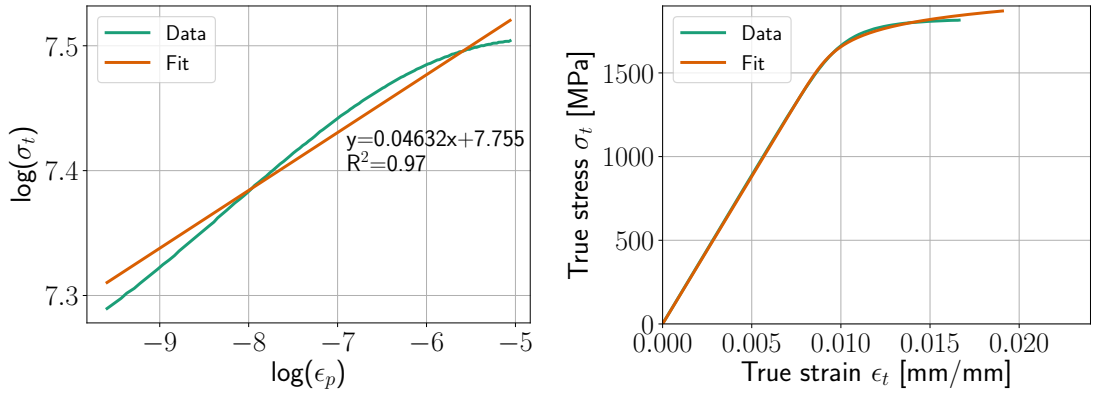

(a) Linear fitting in a double logarithmic plot. **(b)** True stress and strain curve and Ramberg-Osgood interpolation.

Figure 3.1

Figure 3.1(a) shows the straight line fitting the log-log plot, in which data has been restricted between the yielding point and the UTS, in order not to consider the part affected by necking. Successively, in Figure 3.1(b) one can observe the comparison between the experimental data, corrected to be in the true stress-strain plane, and the fitting curve. The resulting H and n values are displayed in Table 3.1. The values imported in ABAQUS lie in a range of ϵ_p from 0 to 1.

3.1.2 Cohesive Zone Modelling

Cohesive Zone Modelling (CZM) has been widely presented and discussed in literature for the past 50 years. The early research on this topic has been conducted by Dugdale in 1960 [107], who introduced the idea of a cohesive force preventing the crack from advancing. In his model, the author set the magnitude of this cohesive force to be equal to the yield strength σ_Y of the material, modeled as perfectly elasto-plastic. Successively Barenblatt [108] developed CZM for the decohesion of atomic lattices, replacing σ_Y with a cohesive law.

The main idea behind CZM is the consideration that an infinite stress cannot, of course, realistically exist at the crack tip. It can be seen as a localized damage model, in which fracture is resisted by cohesive tractions [109] and it is due to the separation of the faces of an infinitely thin region, in contrast to continuum damage models, based on deformation. At any time instant, it is possible to identify a so-called "process region" [110] in between two extreme points, namely the *zero damage* and the *zero traction* ones. In correspondence to the first one, damage has not yet affected the behavior, which is therefore dominated by the bulk material properties. Moving towards the other point, failure progressively occurs, corresponding to a monotonic increase of the damage index from 0 (unaffected state) to 1 (failure). In this way, it is possible to implement the crack surfaces opening and separation in a mathematically continuum model [21].

This procedure is forcing damage to occur in a specified location, as the posi-

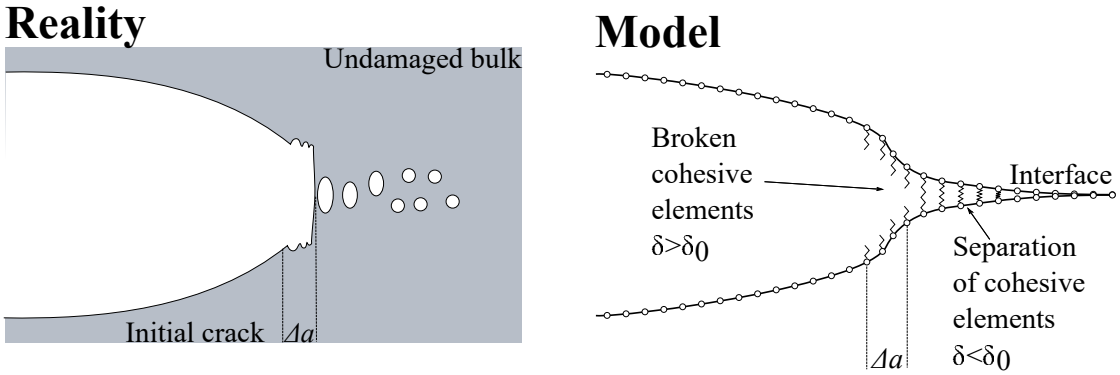

Figure 3.2: Comparison of real material and Cohesive Zone Model (adapted from [111]).

tion of the cohesive zone univocally determines where separation can happen; it is therefore required to be aware of the potential crack location and path [112]. In fact, this condition is met in a CTOD-Δa toughness test, since the specimen is notched and precracked, favoring crack growth along a well-defined plane.

The Traction Separation Law (TSL) describes to the constitutive behavior of the cohesive elements. This law relates the traction, T, with the element opening, *i.e.* the crack surfaces separation, δ. After this variable has exceeded a certain value δ_0, the element fails and it is not capable of carrying or transmitting a load anymore. In addition to δ_0, a cohesive element is defined by its cohesive strength T_0, *i.e.* the maximum stress, and by the cohesive energy Γ_0, with

$$\Gamma_0 = \int_0^{\delta_0} T(\delta) d\delta. \tag{3.9}$$

Being the cohesive elements an artifact to simulate fracture, the TSL parameters are not connected to physical properties. For this reason, the shape of the TSL is not defined *a priori*, but can be adapted by the user depending on the specific condition to be modeled. In addition, the cohesive parameters depend on the choice of the TSL shape: the same model will require, in general, different values of T_0, δ_0 and Γ_0 for different shapes, confirming the phenomenological nature of CZM [111].

It should be noted that the specific influence of the TSL shape on the results is object of debate: in fact, while Tvergaard & Hutchinson [113] obtained a negligible variation of results with the TSL choice, Scheider & Brocks [114] highlighted its impact on their results. Among all the possible formulations, the trapezoidal one in Figure 3.3 has been chosen for its capability of correctly describing the steel's elasto-plastic behavior and its ease of implementation [46, 111].

With reference to the notation in Figure 3.3, the trapezoidal TSL is defined basing on three displacement parameters, δ_1, δ_2 and δ_0, and the cohesive strength T_0. After a first elastic part up to δ_1, corresponding to zero damage, the element exhibits a plateau region with constant stress. Once δ_2 is reached, the stress decreases linearly up to failure, occurring at δ_0.

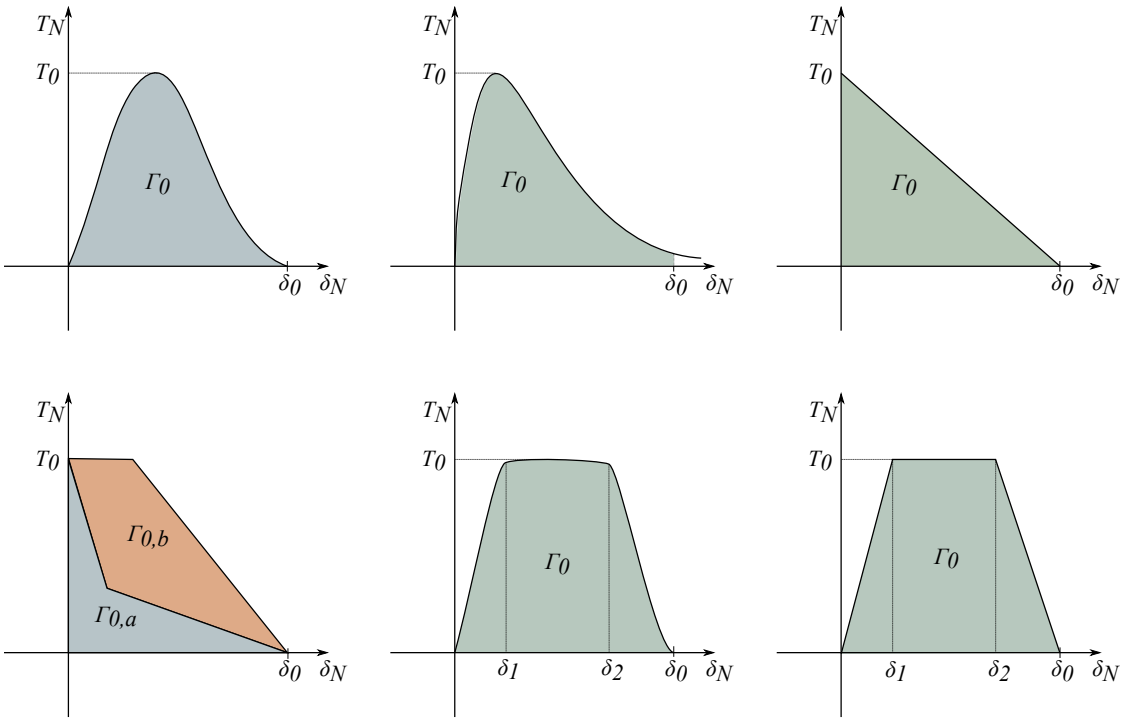

Figure 3.3: Different possible TSL formulations (adapted from [111]).

In ABAQUS, progressive failure is described by means of a damage index, $\bar{D}$ monotonically evolving from 0 to 1. This index is related to the traction as

$$T = (1 - \bar{D})\,\bar{T}, \tag{3.10}$$

where $\bar{T}$ is the traction predicted by the elastic behavior without damage, and computed by the solver for the current increment [115]. Successively, applying the Hooke's law and combining it with Equation 3.10 one can obtain

$$\bar{T} = \delta \cdot E = \delta \cdot \frac{T_0}{\delta_1} \tag{3.11}$$

$$\frac{T}{T_0} = (1 - \bar{D}) \cdot \frac{\delta}{\delta_1} \tag{3.12}$$

The trapezoidal TSL features three regions. As a damage initiation criterion, the maximum nominal strain one is employed, meaning that $\bar{D} = 0$ for $\delta < \delta_1$, *i.e.* the elastic region. Then, in the plateau region, defined for $\delta_1 \leq \delta \leq \delta_2$, the traction is constant, $T = T_0$. Therefore, from Equation 3.12 one can obtain a hyperbolic expression of the damage:

$$\bar{D} = 1 - \frac{\delta_1}{\delta} \tag{3.13}$$

Lastly, in the failure part, $\delta_2 \leq \delta \leq \delta_0$, the traction is decreasing linearly down to 0. Imposing the passage from two points, the expression of traction becomes

$$\frac{T}{T_0} = \frac{\delta_0 - \delta}{\delta_0 - \delta_2}, \tag{3.14}$$

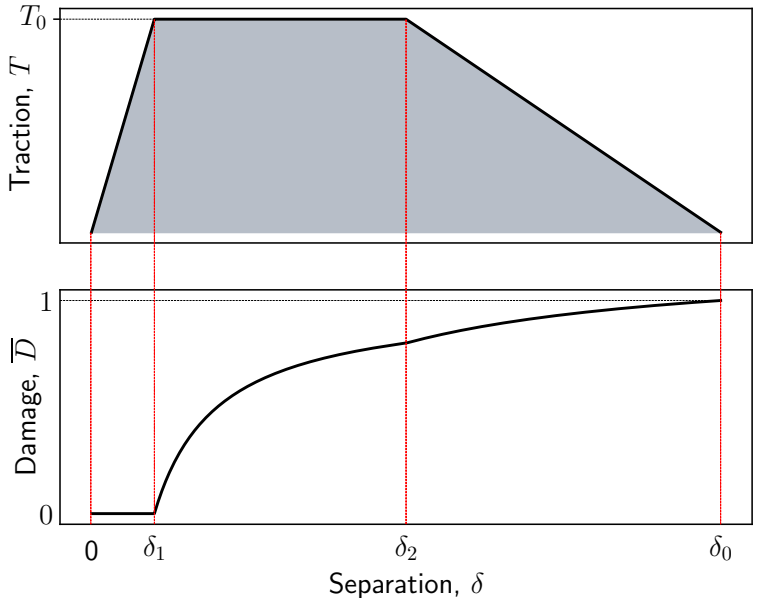

Figure 3.4: Trapezoidal TSL and damage evolution.

and, substituting in Equation 3.12, the damage trend is found as

$$\bar{D} = 1 - \frac{\delta_1}{\delta}\frac{\delta_0 - \delta}{\delta_0 - \delta_2} \tag{3.15}$$

When D reaches 1, *i.e.* for $\delta = \delta_0$, the cohesive element fails, and it is not opposing any stress to its elongation anymore. Therefore, when analyzing the simulation results, the crack is seen as advancing through the cohesive elements that have exceeded the maximum displacement, *i.e.* featuring $D = 1$.

3.1.3 Mesh description

The SENT specimen (Section 2.1.1) has been modeled as a 2-D plane strain object, in order not to excessively increase the computational time. The mesh is generated through a MATLAB script directly writing the *.inp* file, therefore no *.cae* is generated. In order to allow obtaining a structured mesh everywhere and exploiting the specimen's symmetry, the geometry has been simplified, considering only a rectangle, with a length equal to half of the one of the specimen. In this way, only the upper half of the SENT specimen was modelled, as the behaviour would be symmetric.

The smallest element size has to be chosen in order to be able to catch the hydrogen concentration peak close to crack tip; previous works [41, 43, 45] suggest a value in the range 5-20 µm. Here, 15 µm has been chosen as a compromise between accuracy and speed.

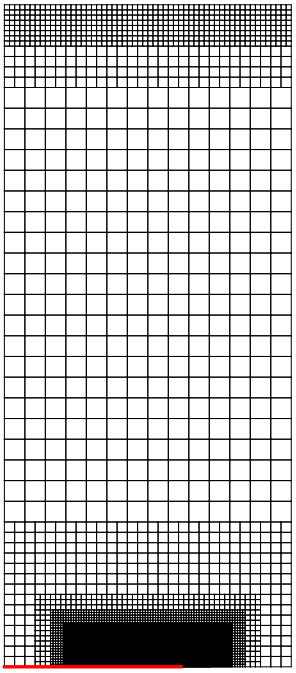

(a) Whole model.

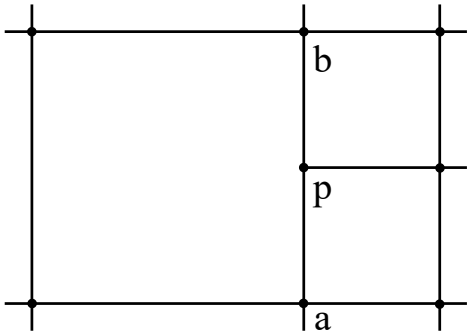

(b) Linear Multi Point Constraint.

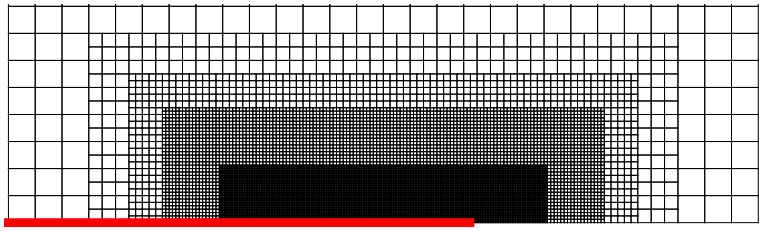

(c) Close-up on the refinement region.

Figure 3.5: Mesh.

Figure 3.5(c) shows the region close to the crack tip: the central region, which features an element size of 15 µm, is surrounded by frames in which the size is doubled at every step. The red line in the figure corresponds to the cohesive elements, which have a length equal to the solid element they are connected to and zero initial thickness. The position of the first cohesive element, corresponding to the crack tip location after pre-cracking, has been set 2 mm from the edge. In fact, the notch in Figure 2.2(b) is 1.5 mm deep, to which the extent of the pre-cracking is to be added. This is an hypothesis, that has to be checked based on the experimental pre-crack measurement.

Regarding the refinement technique, Gobbi *et al.* [41] showed that using Multi Point Constraint (MPC) results in having the smallest error in the estimation of the hydrostatic stress gradient. Being this value necessary for the estimation of hydrogen diffusion in the lattice, according to the equations and techniques described later, MPC was chosen. More in detail, this constraint regards the degrees of freedom of the nodes created passing from coarser to finer mesh frames (node p in Figure 3.5(b)): each value is computed as a linear interpolation of the neighboring nodes (a and b).

3.1.4 Hydrogen effect and trapping

In order to predict the embrittlement phenomenon, the model has to take into account the diffusion of hydrogen, which is initially present in the specimen and can be absorbed at the boundary. Once the concentration of hydrogen at the crack

tip is known, the weakening effect is modeled by reducing the cohesive strength Γ_0, *i.e* decreasing the area below the TSL by a factor k. This procedure simulates the HEDE mechanisms described in Section 1.2.1.

Serebrinsky *et al.* [116] built a model for quantifying the effect of the segregated hydrogen on the fracture behavior. The authors obtained a relationship between the cohesive strength and the impurity coverage θ. This was possible fitting the data of Jiang and Carter [117], relating surface energy to θ in $Fe-\alpha$ (110), and extending the findings of Van der Vers and Ceder [28], according to which the failure displacement δ_0 is independent on θ. The relation reads

$$k = \frac{T_0(\theta)}{T_0(0)} = 1 - 1.0467\,\theta + 0.1687\,\theta^2, \tag{3.16}$$

correlating the cohesive strength in the presence of impurity, $T_0(\theta)$, to the one of the non-contaminated material, $T_0(0)$. According to this procedure, the employed trapezoidal TSL is moved towards the horizontal axis for increasing values of the coverage factor θ, as shown in Figure 3.6.

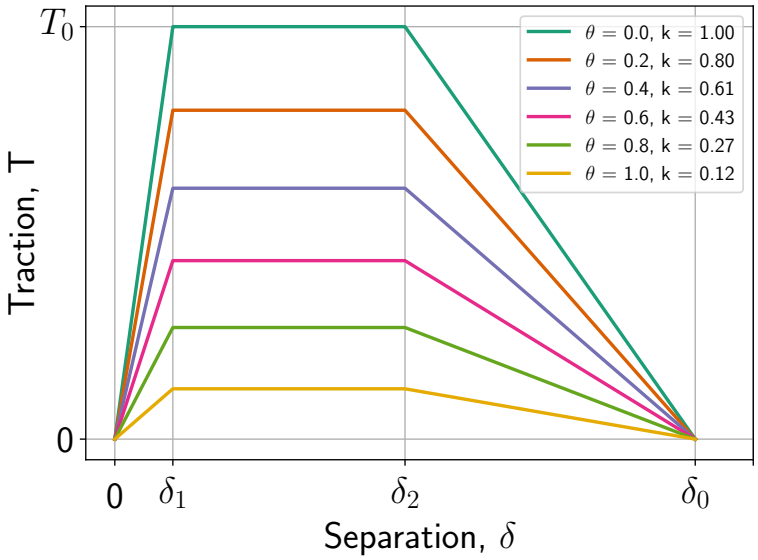

Figure 3.6: Effect of the increasing coverage factor θ on the TSL.

Successively, in order to couple the diffusional problem to an impurity-dependent cohesive law, the authors employed a Langmuir-McLean isotherm [118]:

$$\theta = \frac{C}{C + exp\left(-\frac{\Delta g_b^0}{RT}\right)} \tag{3.17}$$

being $C = C_L + C_T$ the total bulk concentration and Δg_b^0 the variation of the Gibbs free energy between the adsorbed and bulk standard states, set to 30 kJ/mol [116].

The effect of plastic deformation on the dislocation density and, therefore, on the trap sites population, is taken into account by means of the exponential law

proposed by Kumnick & Johnson [119], obtained fitting experimental data for iron and steels, *i.e.*,

$$log_{10}(N_T) = 23.6 - 2.33\, exp(-5.5\, \epsilon_p). \tag{3.18}$$

This relation allows modifying the trap sites density at every increment and, consequently, the local equilibrium between solved and trapped hydrogen.

3.1.5 Thermal-diffusional analogy

ABAQUS allows defining a temperature-stress coupled analysis by means of the UMATHT subroutine, in which the general form of the heat transfer equation is implemented:

$$\rho \frac{\partial U_q}{\partial t} + \nabla \cdot \mathbf{J_q} + r_q = 0, \tag{3.19}$$

where ρ is the mass density, U_q the internal thermal energy per unit mass, J_q the heat flux and r_q represents the source term.

The diffusion-stress analysis is not implemented in the solver. However, in our problem the equation to be solved reads

$$\frac{\partial C}{\partial t} + \nabla \cdot \mathbf{J_m} = 0, \tag{3.20}$$

being C the total concentration and J_m the hydrogen flux. No hydrogen source term r_q is present.

Comparing the equations, the analogy is evident, setting

$$\rho U_q = C \tag{3.21}$$

$$\mathbf{J_q} = \mathbf{J_m} \tag{3.22}$$

$$r_q = 0 \tag{3.23}$$

Now, proper expressions for C and $\mathbf{J_m}$ are needed. Regarding the concentration, it is sufficient to recall that the total amount C is the sum of the interstitial and trapped hydrogen contents. Furthermore, these two terms are related by Equation 1.16, and the term βN_L, linking the lattice concentration to the fractional occupation of NILS, is computed for steel as

$$\begin{aligned} \beta N_L &= \frac{\rho N_A \beta}{A M_{Fe}} = \\ &= \frac{6.022 \cdot 10^{23}\ \text{mol}^{-1} \cdot 7870\ \text{kg/mm}^3 \cdot 6\ \text{NILS/atom}}{55.8 \cdot 10^{-3}\ \text{kg/mol}} \\ &= 5.096 \cdot 10^{20}\ \text{NILS/mm}^3 \end{aligned} \tag{3.24}$$

The open-source PolyHydra code has been employed to solve this fully coupled problem. An accurate description of the subroutines working scheme can be found in [21, 41].

3.1.6 Residual stresses

The presence of residual stresses can be taken into account in ABAQUS following two different approaches.

In the first one, an accurate description of the printing stage is needed. In particular, a preliminary numerical model has to be built, implementing both the heat transfer equations, describing the laser-powder interaction, and the fluid dynamics of the melt pool. Subsequently, the magnitude and distribution of residual stresses are obtained directly by the thermal contraction due to the cooling down to room temperature. This procedure shows a great advantage in terms of accuracy, since the residual stress field is directly computed starting from its physical causes; on the other hand, such a description requires the implementation of heavily complex equations, coupling the heat transfer, fluidodynamic and mechanical problems [120, 121]. Additionally, a thorough knowledge of the possible precipitates formation mechanisms is needed, as they might involve heat exchanges [122].

Once that the thermal analysis has been conducted, the resulting stress field can be stored and called in the subsequent mechanical analysis, by means of the string

```
*INITIAL CONDITIONS, TYPE=STRESS, FILE=x.odb
```

Alternatively, a much less demanding path can be followed. After the samples have been printed, the presence of residual stresses is evaluated experimentally, employing one of the several methods available [123]. Starting from the knowledge of the stresses in some discrete points, the stress field is reconstructed in an iterative way. First, the experimentally measured stresses are passed in ABAQUS by means of the SIGINI (**sig**ma **ini**tial) subroutine, called by

```
*INITIAL CONDITIONS, TYPE=STRESS, USER
```

The FORTRAN file has to show the structure [115]

```
      SUBROUTINE SIGINI(SIGMA,COORDS,NTENS,NCRDS,NOEL,NPT,LAYER,
     1 KSPT,LREBAR,NAMES)
C
      INCLUDE 'ABA_PARAM.INC'
C
      DIMENSION SIGMA(NTENS),COORDS(NCRDS)
      CHARACTER NAMES(2)*80


      user coding to define SIGMA(NTENS)


      RETURN
      END
```

The coding has then to define the components of the stress tensor, either element-wise or based on the coordinates.

The stress values, being measured in discrete points, will not, in general, constitute an equilibrated stress field. For this reason, an initial static analysis is needed in the ABAQUS job, with no imposed loads or displacements. At the end of the step, the obtained stress field will present different values in correspondence of the experimental points, due to the solution of the equilibrium equations. For this reason, the process has to be iterated, in order to obtain an equilibrated stress field as close as possible to the experimentally measured one.

A Python script can be written, whose goal is to extract the stress components element by element. The data, contained in a text file, is successively imported in the subroutine, and manually modified to resemble the experimental data. This process is repeated until a satisfying resemblance between the stress field after the equilibrium step and the experimental data is found. Examples of the Python script and the SIGINI subroutine are reported in Appendices A.1 and A.2.

3.1.7 Loads and boundary conditions

As initial boundary conditions, both in the cases with and without hydrogen, the vertical displacement of the nodes on the lower side of the cohesive elements was set to zero, simulating the resistance of the not-modelled lower half of the specimen. At the same time, the motion along the horizontal direction is prevented imposing $U_1 = 0$ at the top-center node. Additionally, the hydrogen model simulates pre-charging of the specimen, with a uniform hydrogen concentration. A concentration has to be written in ABAQUS in terms of atoms per cubic millimeter; being C normally expressed in parts per million (ppm), the conversion factor is

$$\begin{aligned} 1\,\text{ppm} = 10^{-6}\frac{\text{g}_\text{H}}{\text{g}_\text{steel}} = 10^{-6}\cdot 8.03\cdot 10^{-3}\frac{\text{mol}_\text{H}}{\text{mm}^3} = \\ = 4.836\cdot 10^{15}\,\frac{\text{at}_\text{H}}{\text{mm}^3}, \end{aligned} \tag{3.25}$$

having considered the density measured in Section 2.2.3.

Moreover, the hydrogen boundary condition has to be discussed. Setting a constant concentration on the boundary simulates an *in situ* test, in which hydrogen is capable of penetrating into the specimen during the experiment. On the other hand, hydrogen pre-charging followed by an *ex situ* test requires to take hydrogen release from the boundary into account. With the goal to do so, the *FILM ABAQUS command is employed, describing heat flux from a surface as

$$q = -h(\theta - \theta^0). \tag{3.26}$$

In order to define the flux direction, a vector is required, defined as the normal to one of the element faces. In the relation above, q represents the heat (atomic) flux, θ the local temperature (concentration), θ^0 the reference sink temperature

(concentration), set to 0, and h is the film coefficient. In our case, h should have the LT^{-1} dimension, since it has to link the concentration in at/mm^3 to the atomic flux in at/(s·mm^2). The numerical value of h was approximated starting from the data in the paper by Colombo *et al.* [100]. The authors report a hydrogen concentration moving from 2.7 to 1.3 ppm in 5 hours. Basing on the C(T) specimen geometry (area $A = 3400$ mm^2 and volume $V = 11700$ mm^3), and assuming Newtonian cooling, by means of

$$\frac{C}{C_i} = exp\left(-\frac{hA}{V}t\right), \tag{3.27}$$

one can obtain h equal to $1.4{\cdot}10^{-4}$ mm/s. Consequently, in the ABAQUS definition, an approximate value of $h = 10^{-4}$ mm/s was used.

The model simulates a displacement-controlled test; in fact, during the step, the vertical displacement of the upper nodes is imposed as a boundary condition. A graphical summary of the imposed boundary conditions is offered in Figure 3.7. The elements highlighted in red represent the region of either constant C_L or hydrogen flux, depending on the specific case.

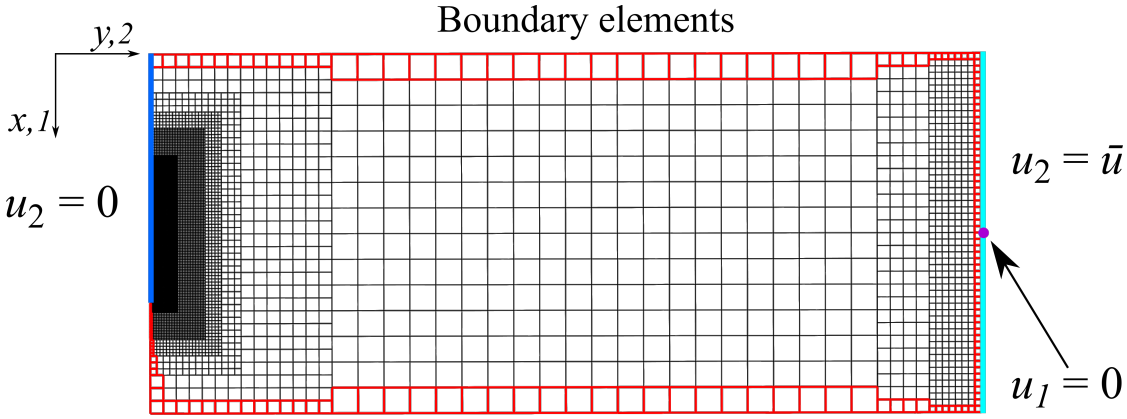

Figure 3.7: Applied boundary conditions.

When running the model without hydrogen, the total step time is 1 s, as the material properties are considered independent on the strain rate. On the other hand, the step time plays an important role in the hydrogen simulation, as a lower strain rate strongly increases the embrittlement effect [40,124]. Therefore, the step time ranged from 1.2 to 1800 s in different analyses.

3.1.8 Data extraction

After having run the analysis, ABAQUS/Python is used to compile a script (Appendix A.3) which creates *.txt* files containing, for any time increment:

1. the displacement in the y-direction (U_2) at the initial position of the crack tip;
2. the reaction force in the y-direction (RF_2) at the central node of the upper edge;

3. U_2 for each node on the upper edge of the cohesive elements;

4. C_L, C_T and k for each element above the cohesive elements.

Then, in order to estimate the crack advancement, U_2 is compared with the displacement leading the cohesive elements to failure, δ_0. If $\delta > \delta_0$, the element is counted as failed and its length is added to the extension of the crack. The CTOD is computed doubling the U_2 value at the initial crack position, as the lower half of the specimen would have a symmetric behavior. Finally, plotting the CTOD vs Δa for all the time increments, the numerical CTOD-R curve is obtained.

3.2 Results

3.2.1 TSL calibration

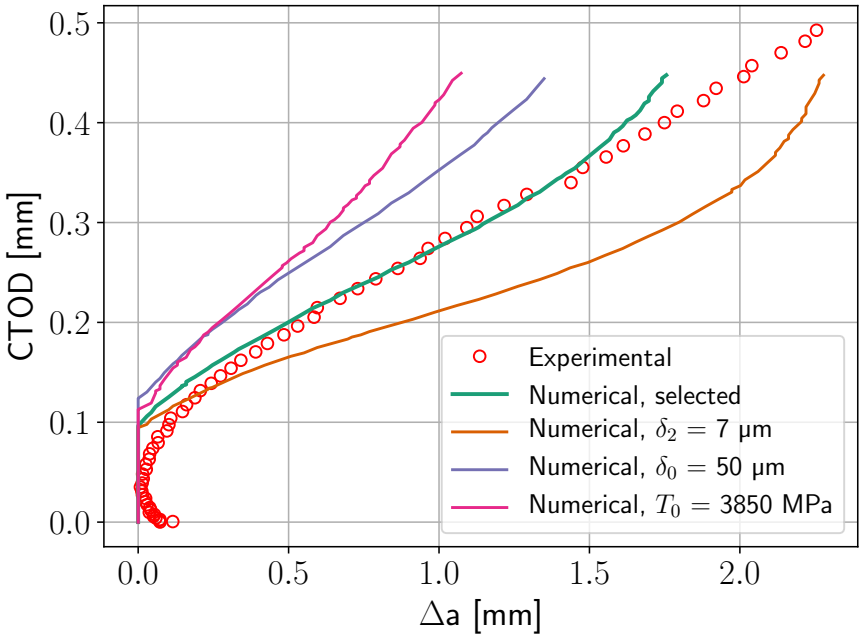

Figure 3.8: CTOD-Δa curves comparison. The numerical curves different from the selected one have been obtained starting from the optimal TSL parameters, displayed in Table 3.2, and changing one at a time. The effect of the variation of δ_1 is not reported, as hardly recognizable.

The TSL parameters have to be chosen in order to replicate the experimental data. Since it is not possible to simply fit the parameters, as a FEM analysis has to run with the current set to obtain the deviation with respect to the experimental curve, a trial and error procedure has to be followed. For each set of δ_1, δ_2, δ_0 and T_0, the vertical displacements of the nodes connecting solid and cohesive elements (the red line in Figure 3.5(c)) are extracted (Appendix A.3), and the similarity of the CTOD-Δa numerical curve to the experimental one is evaluated.

After having identified the 4 acceptable parameter ranges by visually inspecting the curves, a Python script (see Appendix A.4) was executed in order to run an analysis for all the possible combinations; the *.odb* files obtained with the best 3 sets of parameters are automatically renamed and copied in a separate folder. The similarity between the curves was taken into account interpolating the experimental data on the numerical Δa values, in order to then compute the mean quadratic deviation of the CTODs. Table 3.2 displays the TSL parameters best fitting the experimental data, whereas in Figure 3.8 it is possible to observe the numerical and experimental curve, as well as the behaviors for different choices of parameters.

Parameter	Value
δ_1	0.7 µm
δ_2	9.5 µm
δ_0	40 µm
T_0	3750 MPa

Table 3.2: Optimal TSL parameters

The influence of the parameters on the resulting curve reveals to be quite intuitive. In fact, recalling the TSL shape of Figure 3.4, one can recognize the parameters definition: decreasing δ_2, damaging is initiated in advance, leading to easier crack advancement; on the other hand, an increase in both δ_0 and T_0 have the effect of strengthening the cohesive elements (the cohesive energy Γ_0 is increased), delaying their failure, with, consequently, higher CTOD. The numerical value of the selected cohesive strength, *i.e.* 3750 MPa, is in accordance with the expectations. In fact, literature [44, 125] reports a cohesive to yield strength ranging from 2 to 3. In the present case, this ratio is equal to 2.15.

3.2.2 Hydrogen simulation

Parameter	Value
Hydrogen concentration, C_0	1 ppm
Deformation rate, $\dot{\epsilon}$	0.1 mm/min
Diffusivity, D_L	10^{-3} mm^2/s

Table 3.3: Simulation parameters.

As a first analysis, the coupled diffusional-mechanical problem was solved with the parameters reported in Table 3.3; the effect of their variation will be discussed in the following sections. The implemented diffusivity is the lattice one, D_L. In addition to the initial homogeneous concentration C_o, the same concentration is set to be constant on the boundary elements, simulating an *in situ* test.

Figure 3.9 depicts the lattice hydrogen concentration field, C_L, in the vicinity of the crack tip, at the time frame immediately before the failure of the first cohesive element. One can observe that it assumes its maximum a few elements in front of

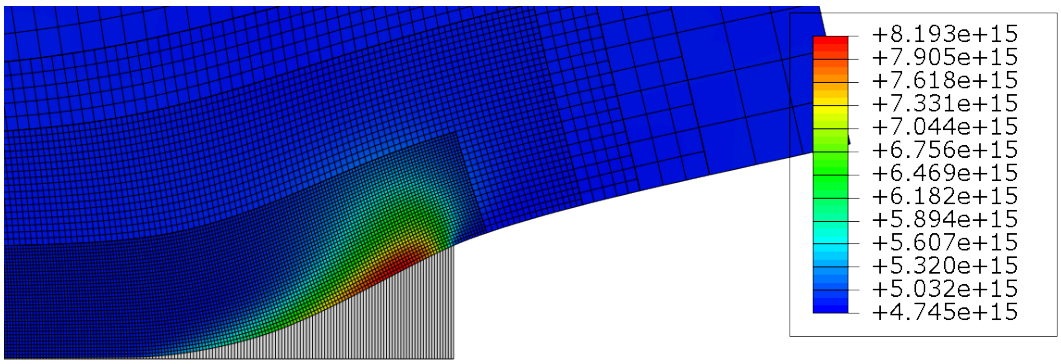

Figure 3.9: Lattice hydrogen concentration (C_L) field, at the onset of crack propagation. Values are in at/mm^3.

the tip. This is caused by the gradient of the hydrostatic stress, $\nabla\sigma_h$, which results being maximum in correspondence of the cohesive elements that just started their separation. The solubility of hydrogen in the lattice becomes larger due to lattice expansion, resulting in a flux towards the tip region. This observation remains valid for the whole duration of the simulation, and is in accordance with the findings of [21, 41, 43].

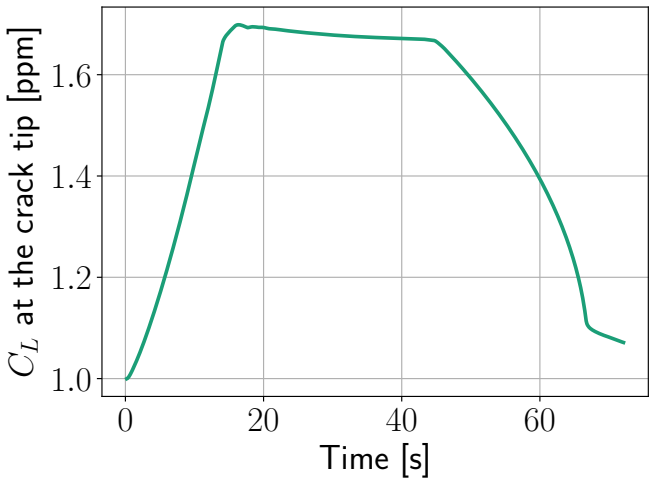

Figure 3.10: Lattice hydrogen concentration at the crack tip as a function of time.

The evolution of hydrogen concentration at the crack tip is displayed in Figure 3.10. Starting from the nominal concentration of 1 ppm, hydrogen rapidly migrates towards the tip from the surrounding region, until a peak value is reached. Successively, the concentration remains almost constant for 20 s: during this period of time, the diffusing hydrogen does not move to further concentrate at the tip, but in an area whose size increases in time. In this way, a relatively large number of cohesive elements is affected, suffering from a reduction in the k factor, defined in Equation 3.16. A decreased k is directly translated into a diminished allowable stress.

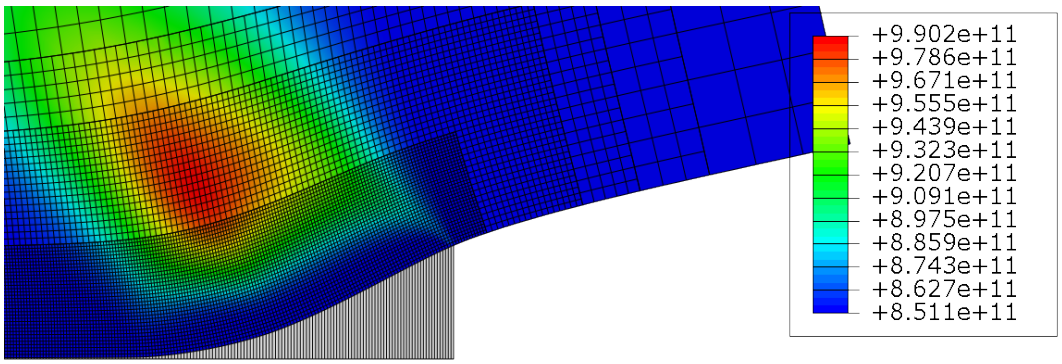

Figure 3.11: Trapped hydrogen concentration (C_T) field, at the onset of crack propagation. Values are in at/mm^3.

The sudden decrease at 45 s can be explained referring to the stress field. In fact, at this time instant the first cohesive element exits the TSL plateau region: this causes a variation in the distribution of $\nabla\sigma_h$, which governs hydrogen flux. In other words, since the stress is locally decreasing, hydrogen is forced to leave the tip, as the reduced tension provokes lattice shrinking. Consequently, the interstitial sites become smaller, compelling hydrogen migration. Once that the crack starts propagating (62 s circa), the crack tip moves much faster than hydrogen, helped by the embrittled area in front of its original position. This explains the abrupt slope variation, as now the crack is proceeding through a region where hydrogen had shorter time to diffuse out.

Focusing now on the trapped hydrogen concentration, C_T, shown in Figure 3.11, one can immediately recognize a large difference with respect to C_L, in terms of both magnitude and distribution. In fact, the contour is strongly related to the ϵ_p one: the number of trap sites increase with the plastic deformation amount, following Equation 3.18. A part of these sites is promptly filled, as the equilibrium between lattice and trap fractional occupation (Equation 1.14) has to be respected.

Due to the modest value of the equilibrium constant, K_T, at 25° C, the trapped hydrogen population happens to be 4 orders of magnitude lower than C_L. As a consequence, the trapped hydrogen does not play a significant role in the cohesive elements behavior.

Additionally, Figure 3.12 illustrates the vertical stress, σ_{yy}, fields around the crack tip, immediately before crack propagation, for both the simulations. The different extent of the process region is understandable observing the different number of cohesive elements with a non-negligible separation. Moreover, the difference in the deformed shape is immediately evident, with a much larger degree of plasticization when hydrogen is absent. This fact is also confirmed by the maximum value of ϵ_p, that drops from 3.1% to 0.45%.

Figure 3.13(a) reports the trends σ_{yy} in the vicinity of the crack tip. Comparing the calibration simulation, without hydrogen, to the present one, with 1

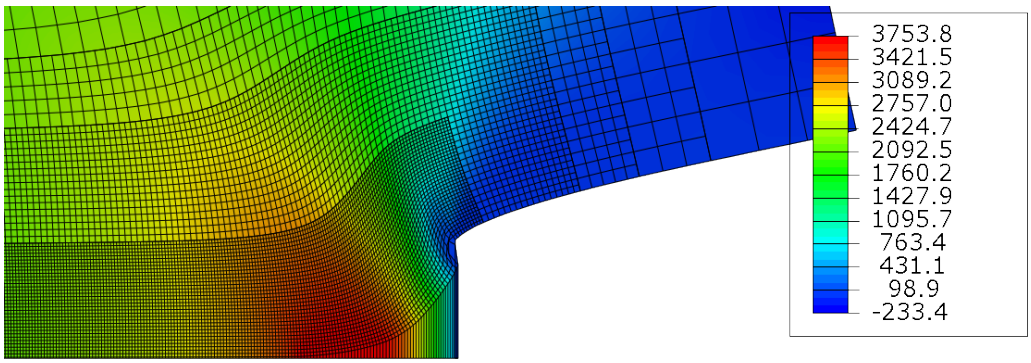

(a) Stress field in absence of hydrogen.

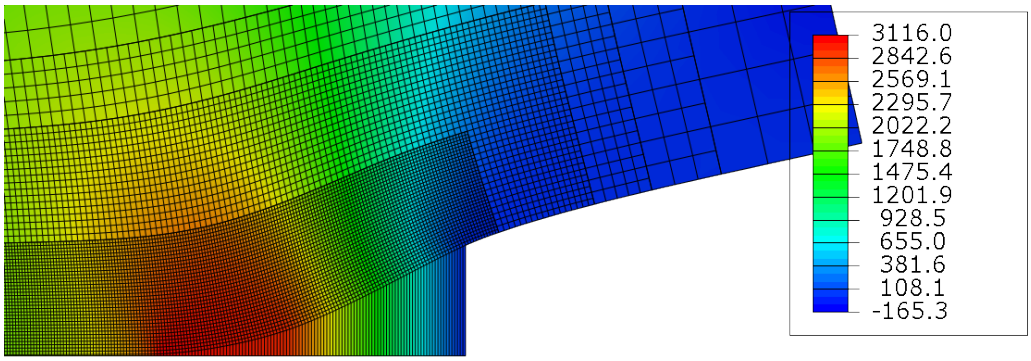

(b) Stress field with 1 ppm hydrogen.

Figure 3.12: σ_{yy} fields at the onset of crack propagation. Values are in MPa.

ppm nominal concentration, it can be seen that the span of the process region in the green line is quite limited, meaning that it is possible to find elements in the vicinity of the tip that are still capable of offering their original resistance. On the other hand, hydrogen makes crack advancement almost instantaneous, as it is necessary to proceed down the crack path by 1 mm to approach T_0.

Furthermore, the value of the TSL decreasing factor is extracted from the *.odb* file and plotted as a function of the distance from the crack tip. The graph on Figure 3.13(b) is dependent on the concentration trend, and allows understanding the different degrees of embrittlement. Far from the tip, where hydrogen is present with its nominal concentration, the maximum allowable stress in the cohesive elements is reduced by 17%; on the other hand, the element 250 µm far from tip suffers from a 25% reduction, highlighting the weakening effect of hydrogen migration towards the tip.

3.2.3 Hydrogen flux from the boundary

An analysis with the *FILM condition described in Section 3.1.7 was conducted, in order to evaluate the influence of hydrogen leaving the specimen due to surface desorption.

Figure 3.14(a) shows the comparison of the lattice hydrogen concentration in the

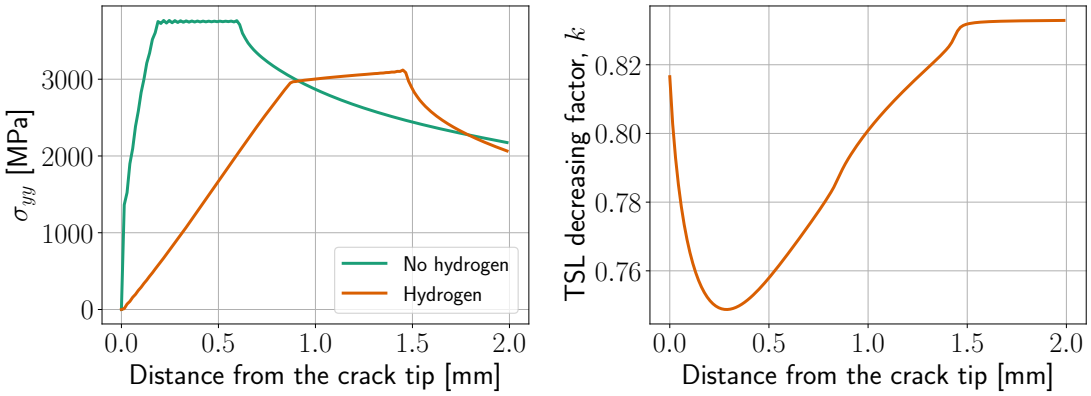

(a) Stress around the crack tip, at the onset of crack propagation.

(b) Trend of the TSL decreasing factor around the crack tip, at the onset of crack propagation.

Figure 3.13

two cases. One can observe that the influence of the updated boundary condition is only slightly appreciable close to the tip. At a greater distance, the two curves overlap, as the solid elements connected to the cohesive ones are not included in the boundary definition; in reality, they would be connected to the lower half of the specimen, and therefore they are not able to exchange hydrogen with the environment. The difference of the two cases is more appreciable in Figure 3.14(b): in fact, the plateau in the time-C_L plot described previously is not present anymore, as hydrogen is constantly lost during the simulation. The most relevant feature is the one illustrated in the C_L field of Figure 3.14(c). As a matter of fact, an hydrogen-depleted zone is formed to the right of the tip, where the precracking is modelled. This region is not present in Figure 3.9, as the hydrogen attracted due to $\nabla\sigma_h$ was constantly compensated by the new atoms available on the boundary. At any rate, the CTOD-Δa curves for the two boundary conditions overlap, as this depletion region is not important from the mechanical behavior point of view. For this reason, in the subsequent analyses the *in situ* condition, *i.e.* constant concentration on the boundary, was adopted.

3.2.4 Concentration effect

In order to choose the relevant nominal concentration range, it was made reference to literature [20, 21, 40, 45, 126, 127]. Stopher *et al.* [20] report the case of a bearing steel with an experimentally measured hydrogen concentration equal to 4.8 ppm. Consequently, it was chosen to make the nominal concentration in the model range from 0 to 5 ppm.

Figure 3.15(a) summarizes the effect of hydrogen on the macroscopical toughness curve. Basing on the plot, it is possible to state that the toughness is highly sensitive to low hydrogen concentrations: 0.1 ppm are sufficient to cause a reduction of the CTOD of 35%. Barsanti *et al.* report 0.1 ppm as the hydrogen concentration that can arise from common Nickel plating [128]. The reduction in

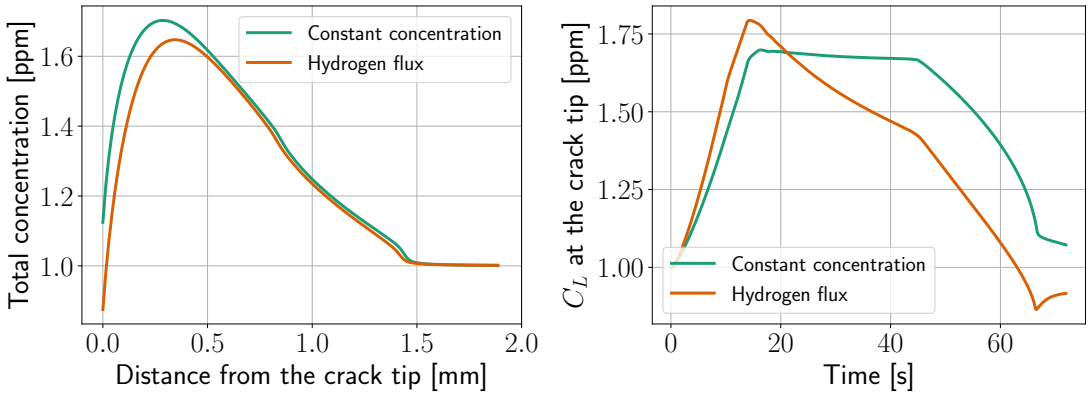

(a) C_L trend around the crack tip at the onset of propagation, for different boundary conditions.

(b) C_L at the crack tip as a function of time.

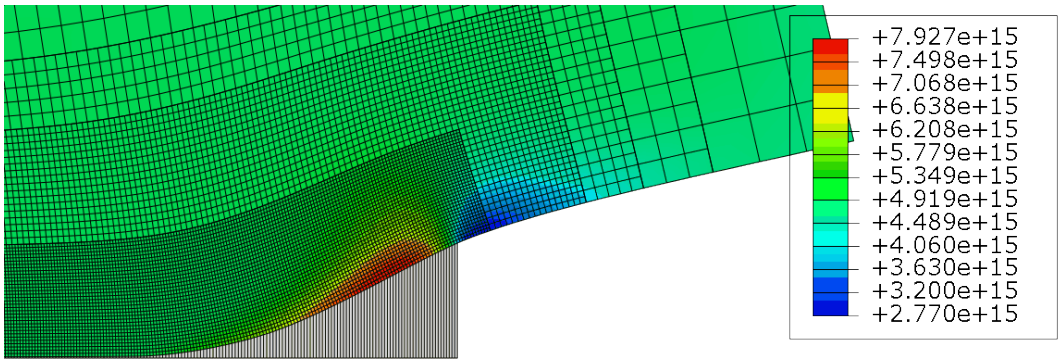

(c) C_L at the crack tip field at the onset of crack propagation, considering hydrogen flux at the boundary. Values are in at/mm^3.

Figure 3.14: Effect of the change in the hydrogen boundary condition.

the CTOD value is doubled when increasing the concentration up to 5 ppm. The sharp drop in CTOD for relatively little hydrogen contamination is in accordance with the reference work by Gobbi [21].

Moreover, even though the crack opening required for propagation remains almost constant (in the 0.08-0.10 mm range), the evolution is deeply different. In fact, the crack grows in a stable manner for low or no hydrogen; on the other hand, propagation and failure are almost instantaneous for high concentrations. This effect can be more clearly illustrated plotting the crack advancement as a function of time. Shifting all the curves to the origin, *i.e.* subtracting the time instant corresponding to the onset of propagation, Figure 3.15(b) is obtained. In absence of hydrogen, the crack takes more than 1 minute from the onset of propagation to lead to complete failure; conversely, for a concentration as high as 5 ppm, this time period is shortened down to barely 1 s.

Lastly, the maximum value of the reaction force in the vertical direction (RF_2) on the node set at middle-length of the top edge is extracted, and plotted as a function of hydrogen concentration. The graph, shown in Figure 3.16, confirms the previous observation: the hydrogen detrimental effect increases more rapidly

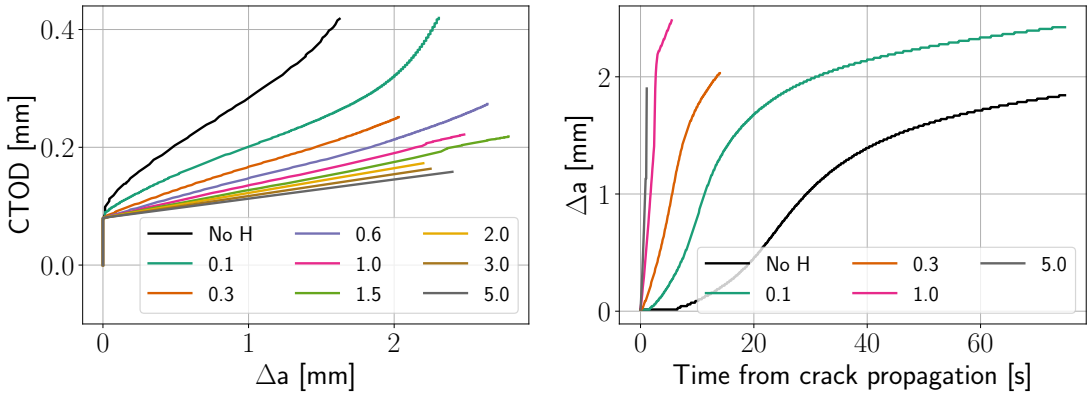

(a) CTOD-Δa curves at different hydrogen concentrations.

(b) Crack growth in time.

Figure 3.15: Effect of concentration variation. Values in the legend are in ppm.

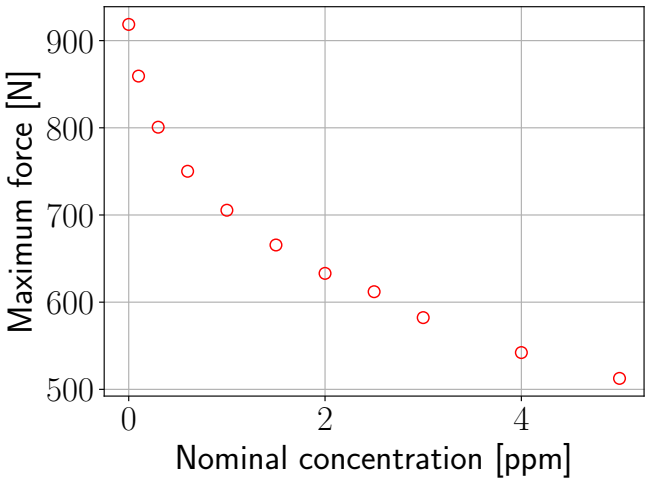

Figure 3.16: Variation of the maximum reaction force in the node at the center of the upper edge with hydrogen concentration.

at low concentrations. The slope becomes less negative shifting towards larger ppms.

3.2.5 Strain rate effect

It is well known that the detrimental effect of hydrogen depends on the deformation conditions. In particular, past evidence [129, 130] showed how a slower strain rate amplifies the reduction in the mechanical properties: this phenomenon is generally attributed to the longer time available for hydrogen accumulation at the tip. Moreover, the hydrogen effect is hardly recognizable in Charpy impact tests, as the strain rate is too large, leading to a negligible variation in the impact energy with respect to the uncharged specimens [131].

Here, the strain rate influence on the mechanical properties was numerically investigated varying the deformation speed, $\dot{u}$: this is made possible changing the

$\dot{u}$ [mm/min]	$\dot{\epsilon}$ [s^{-1}]	Top edge u_2 [mm]	Time [s]	Time increment [s]
0.005	$5.5{\cdot}10^{-6}$	0.15	1800	$8{\cdot}10^{-1}$
0.01	$1.1{\cdot}10^{-5}$	0.15	900	$5{\cdot}10^{-1}$
0.1	$1.1{\cdot}10^{-4}$	0.15	90	$5{\cdot}10^{-2}$
1	$1.1{\cdot}10^{-3}$	0.20	12	10^{-2}
10	$1.1{\cdot}10^{-2}$	0.20	1.2	10^{-3}

Table 3.4: Imposed deformation rates in the analyses.

total analysis time in the *.inp* ABAQUS file. Table 3.4 relates $\dot{u}$ to the strain rate, $\dot{\epsilon}$, being the conversion factor the specimen height, and shows the time parameters of the input file. The time increment was extended as the total time increased, for two reasons: besides maintaining the computational time in an acceptable range, it was noted that the model showed some degree of hourglass instability for a large number of increments. Since both a mesh refinement and the enhanced hourglass control appeared being of little help, it was decided to restrain the increments number.

Moreover, it can be noted that the imposed displacement was increased, increasing the deformation rate. This was necessary in order to ensure crack propagation: in fact, the cohesive elements become less affected by hydrogen at high $\dot{u}$, requiring a larger u_2 to be applied at the top edge. As for the determination of the TSL parameters, the adequate value is to be found in an iterative way, observing the extent of crack propagation at the end of the analysis, increasing u_2 in case it was insufficient.

Regarding the nominal concentration, all the analyses were conducted imposing a value equal to 0.3 ppm. In fact, the strain rate influence on the CTOD-Δa curve is hardly recognizable at 1 ppm, as k is already greatly lowered by the nominal concentration, before hydrogen flows towards the tip.

Figure 3.17(a) illustrates the effect of the deformation rate on the mechanical properties. In particular, it is possible to have a confirmation of the expected trend, with a reduced material resistance at slower rates. The significant influence of the longer time available for diffusion is evident in Figure 3.17(b). In fact, when the specimen is pulled quickly, hydrogen almost does not have the possibility of diffusing towards the tip, resulting only in a slight increase of 0.1 ppm in the tip C_L. Conversely, at the lowest deformation rate, 5 µm/min, the concentration at the tip grows as high as 1.2 ppm. In addition, one can observe that the position of the peak moves progressively further away from the tip as the deformation rate decreases. Again, this phenomenon is attributed to hydrogen migration towards the position featuring the maximum $\nabla\sigma_h$, *i.e.* a few cohesive elements away from the tip: the increased time allows hydrogen to concentrate in that region.

Lastly, Figure 3.17(c) reports the trapped hydrogen concentrations in the vicinity of the tip. Even though the absolute value is 3 orders of magnitude lower than

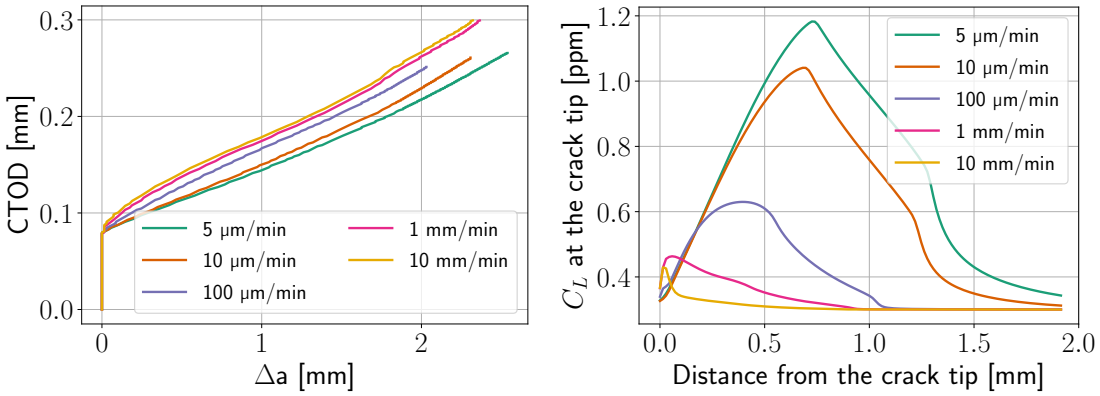

(a) CTOD-Δa curves at different deformation rates.

(b) C_L trend around the crack tip, at different deformation rates.

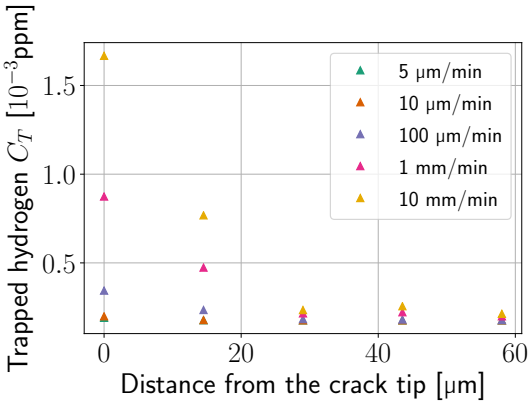

(c) C_T in the vicinity of the crack tip, at different deformation rates.

Figure 3.17: Effect of strain rate variation.

C_L, therefore negligible from the k point of view, one can note a significant difference depending on the deformation rate. Moreover, the trend is opposite to the C_L one, with larger values at fast deformation rates; this is explained referring to the equivalent plastic strain, ϵ_p. In fact, at 10 mm/min, as already said, C_L shows a limited increase at the tip, leading to a higher k value. This slighter decrease in T_0 allows a greater stress at the tip, with a consequently higher ϵ_p. The dislocation density increases accordingly, creating a larger number of trapping sites, hence the observation of a larger trapped population.

3.2.6 Diffusivity effect

In literature, it is possible to find hydrogen diffusivity values lying in a wide range [132–134]. In fact, D_L depends on several factors, such as temperature and the steel lattice structure (Figure 3.18). Moreover, the presence of traps influences the experimental measure of diffusivity, actually obtaining the value of the effective diffusion coefficient, D_T (Equation 1.17), rather then D_L. The presence of traps slows down lattice diffusion, resulting in a lower measured value, due to the kinetics of hydrogen trapping and releasing. Regarding maraging steel, Valentini

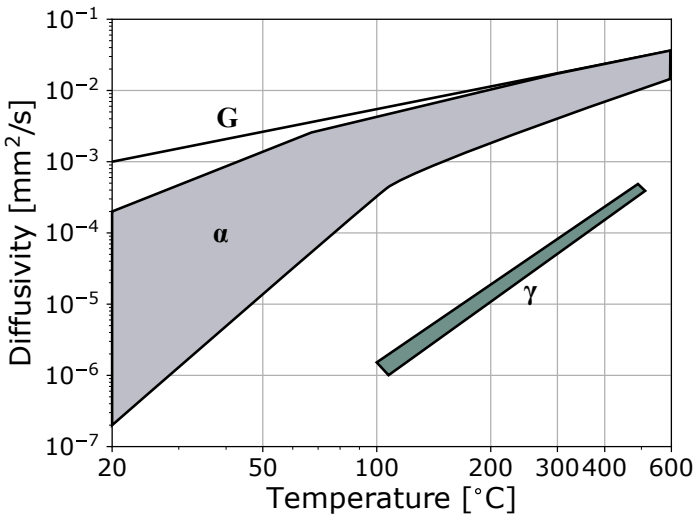

Figure 3.18: Diffusion coefficient for hydrogen in steel for ferrite (α) and austenite (γ). G represents lattice diffusion. Adapted from [12].

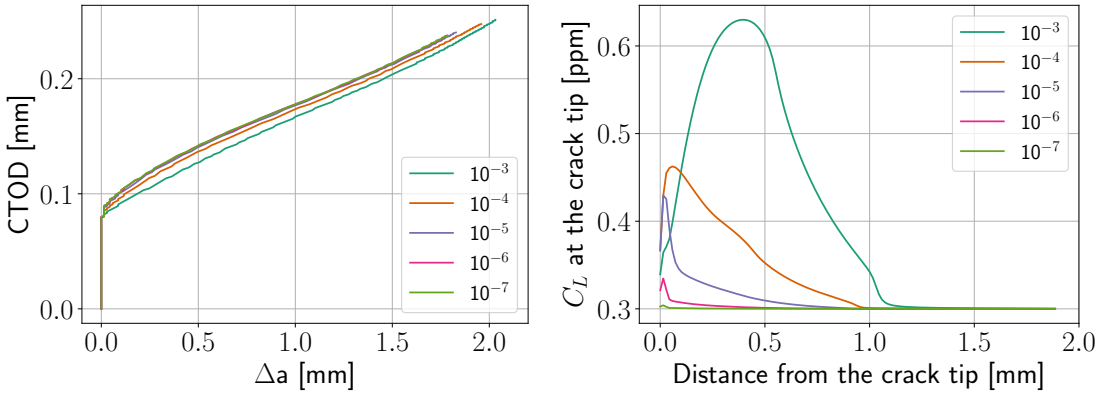

(a) CTOD-Δa curves for different diffusivities.

(b) C_L trend around the crack tip for different diffusivities.

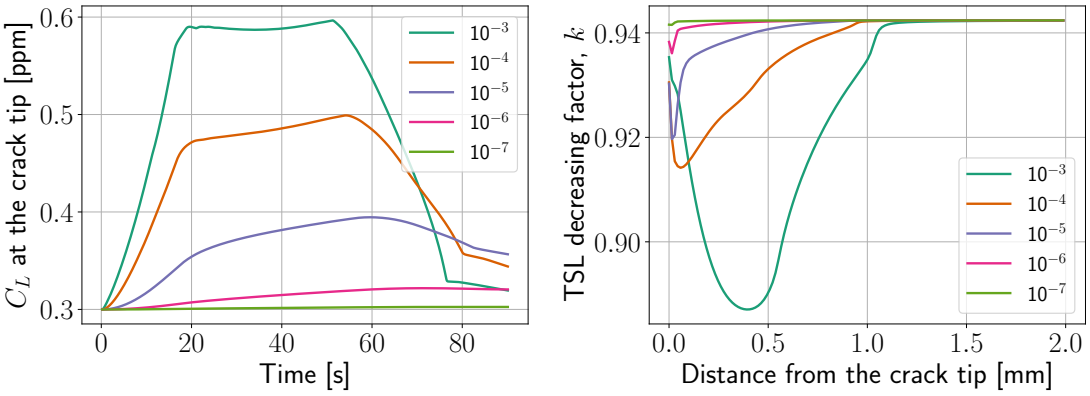

(c) Lattice hydrogen concentration at the crack tip as a function of time, for different diffusivites.

(d) Trend of the TSL decreasing factor around the crack tip for different diffusivities.

Figure 3.19: Effect of diffusivity. Values in the legend are in mm^2/s.

et al. [132] report a value in the 8-9·10^{-7} mm^2/s range for 18Ni-250, depending on the aging treatment; instead, Tsay *et al.* [133] investigated T-200, resulting in D_T = 2·10^{-6} mm^2/s.

Being D_L a higly varying parameter, the effect of its variation on the numerical predictions was investigated. The parameter, included in ABAQUS as the thermal diffusivity, due to the thermal analogy described in Section 3.1.5, ranged between 10^{-7} and 10^{-3} mm^2/s. The analyses were conducted setting C_0 = 0.3 ppm and $\dot{u}$ = 0.1 mm/min.

As reported in Figure 3.19(a), the influence of the diffusion coefficient on the CTOD-Δa curve is only slightly recognizable. However, the trend confirms the expectations, with a moderately lower value of the crack opening for larger D_L; this phenomenon can be explained, again, referring to the different rates of hydrogen migration. As a matter of fact, Figure 3.19(b) illustrates the improved capability of hydrogen to concentrate in the region close to the tip for increasing D_L. The shift in position of the maximum value of the lattice concentration C_L, moving further away from the tip as the diffusion coefficient grows, partially counterbalances the larger maximum value. Indeed, one can see the plot of the TSL decreasing factor as a function of the distance from the crack tip in Figure 3.19(d). When D_L is set to be equal to 10^{-4} mm^2/s, the elements close to the tip suffer from a larger decrease in the maximum T_0 with respect to the case of 10^{-3} mm^2/s (1% more).

Lastly, Figure 3.19(c) describes the variation of the lattice concentration at the crack tip as a function of time. Apart from the trend, described previously, one can note that in the case of 10^{-7} mm^2/s C_L remains almost constant for the whole duration of the simulation, basically meaning that hydrogen diffusion is restrained.

Conclusion

The presented numerical model is capable of describing the detrimental effect of hydrogen on the material toughness. The specific influence of the simulation parameters, such as nominal concentration, strain rate and diffusivity, is investigated. The importance of conducting a sensibility analysis lies in the fact that these parameters are highly variable, depending on the environmental and loading conditions. The results confirm what is commonly found in literature.

The nominal concentration, C_0, ranged between 0 and 5 ppm: a larger value leads to a more significant detrimental effect on the toughness. The CTOD curve shows a larger sensibility to hydrogen at low C_0. The effect of the strain rate $\dot{\epsilon}$, varying in the $5.5{\cdot}10^{-6}$ to $1.1{\cdot}10^{-2}$ s^{-1} range, is quite intuitive: a slower $\dot{\epsilon}$ allows allows hydrogen to diffuse towards the crack tip for a longer time, with a consequent more evident impact on the toughness curve. On the other hand, the variation of diffusivity, between 10^{-7} and 10^{-3} mm^2/s, greatly influences the trend of the lattice concentration in the vicinity of the crack tip, while it shows little effect on the CTOD-Δa curve. Additionally, the model response to a different boundary condition, with hydrogen flowing out from the edges, is described, provoking a negligible effect on the mechanical behavior. At any rate, some considerations on the validity of the predictions have to be formulated.

First, we recall that, unfortunately, it was not possible to determine the experimental toughness curve. In fact, the model was calibrated basing on the curve of AISI 4130; certainly, the availability of the 18Ni-300 experimental data would lead to a different set of TSL parameters. Featuring maraging steel a larger UTS and reduced ductility, it is believed one would obtain a greater T_0 and smaller δ parameters. However, this set also varies depending on the geometry: for this reason, a new calibration would be necessary in case of employment of the numerical model in the design stage of a part. Therefore, it was preferred here to focus on the overall functioning of the model, with a description of the influencing parameters.

Moreover, the model includes several equations deriving from the fitting of experimental measurements, on different materials. Actually, a degradation law for the specific alloy would be preferable, as the sensibility to hydrogen depends, in general, on the composition and thermal treatment. In reality, one can find in literature *ad hoc* laws, as in the work of Yu *et al.* [125]; in their work, the authors suggest two different laws for the same high strength steel tempered at different temperatures. Additionally, hydrogen trapping is neglected, as only little

plasticity develops before failure. Therefore, a possible model improvement would certainly include the implementation of the material-tailored degradation law in the ABAQUS subroutine.

In order to confirm or reject the reliability of the model, a proper validation is needed. Gobbi [21] compared the CTOD-Δa curves resulting from the implementation of the aforementioned equations to the experimental behavior of hydrogen-charged AISI 4130 steel. The numerical model predicts a slightly higher toughness with respect to reality. The mismatch was attributed to the lack of implementation of the HELP mechanism, having described solely HEDE. In fact, the prediction of Brocks *et al.* [40], who considered both the mechanisms, perfectly overlaps with the experimental data. Nevertheless, the authors employed a different, closed-source code, which could contain additional different features. Therefore, the experimental validation should be planned in the future project steps, in order to determine whether the HEDE model is accurately describing the maraging steel behavior, which shows reduced ductility with respect to AISI 4130.

Also, the eventual presence of residual stresses, remaining in the material even after the aging treatment, may be considered by means of the SIGINI subroutine. In the present work, the SIGINI was tested and a method to implement the desired stress field, aiming at counterbalancing ABAQUS equilibration, was developed. Successively, due the impossibility of testing the notched specimens, and therefore of measuring the residual stresses present after the sample machining, the subroutine was commented out from the *hydra.f* collection of subroutines. At any rate, the model would promptly be able to include the σ field, with a possible better convergence of experimental and numerical data.

Bibliography

[1] I. M. Robertson, P. Sofronis, A. Nagao, M. L. Martin, S. Wang, D. W. Gross, and K. E. Nygren. Hydrogen Embrittlement Understood. *Metallurgical and Materials Transactions A*, 46:2323–2341, June 2015.

[2] M. Klell. Storage of Hydrogen in the Pure Form. In *Handbook of Hydrogen Storage*, pages 1–37. John Wiley & Sons, Ltd, 2010. ISBN 978-3-527-62980-0.

[3] M. Yakout, M. A. Elbestawi, and S. C. Veldhuis. A Review of Metal Additive Manufacturing Technologies. *Solid State Phenomena*, 278:1–14, 2018. ISSN 1662-9779.

[4] W. Zhang. Technical Problem Identification for the Failures of the Liberty Ships. *Challenges*, 7(2):20, December 2016. Number: 2 Publisher: Multidisciplinary Digital Publishing Institute.

[5] N. E. Dowling. *Mechanical Behavior of Materials: Engineering Methods for Deformation, Fracture, and Fatigue*. Pearson Prentice Hall, 2007. ISBN 978-0-13-186312-5. Google-Books-ID: 6Pp3QgAACAAJ.

[6] L. Vergani. *Meccanica dei materiali*. McGraw-Hill, 2nd edition, 2006.

[7] T. L Anderson. *Fracture mechanics: fundamentals and applications*. Taylor & Francis, Boca Raton, FL, 2005. ISBN 978-0-8493-1656-2. OCLC: 57251284.

[8] R.W. Hertzberg, R. P. Vinci, and J. L. Hertzberg. *Deformation and Fracture Mechanics of Engineering Materials*. Wiley, 5 edition, 2012. ISBN 978-0-470-52780-1.

[9] A. Sciuccati. *Mechanical behaviour of high toguhness steels in extreme environments: influence of hydrogen and low temperature*. PhD thesis, Politecnico di Milano, 2011.

[10] H. J. Grabke and E. Riecke. Absorption and diffusion of hydrogen in steels. *Materiali in tehnologije*, 34:331–341, 2000.

[11] D. V. Ragone and J. Wiley & Sons. *Thermodynamics of materials*, volume 1. Wiley, New York, 1995. ISBN 978-0-471-30885-0. OCLC: 932209609.

[12] J. Woodtli and R. Kieselbach. Damage due to hydrogen embrittlement and stress corrosion cracking. *Engineering Failure Analysis*, 7(6):427–450, December 2000. ISSN 1350-6307.

[13] R. Kirchheim. Revisiting hydrogen embrittlement models and hydrogen-induced homogeneous nucleation of dislocations. *Scripta Materialia*, 62(2): 67–70, January 2010. ISSN 1359-6462.

[14] R. Kirchheim. Interaction of hydrogen with external stress fields. *Acta Metallurgica*, 34(1):37–42, January 1986. ISSN 0001-6160.

[15] P. Sofronis and R. M. McMeeking. Numerical analysis of hydrogen transport near a blunting crack tip. *Journal of the Mechanics and Physics of Solids*, 37(3):317–350, January 1989. ISSN 0022-5096.

[16] G. S. Frankel and R. M. Latanision. Hydrogen transport during deformation in nickel: Part I. Polycrystalline nickel. *Metallurgical Transactions A*, 17(5): 861–867, May 1986. ISSN 1543-1940.

[17] R. A Oriani. The diffusion and trapping of hydrogen in steel. *Acta Metallurgica*, 18(1):147–157, January 1970. ISSN 0001-6160.

[18] G. M. Pressouyre and I. M. Bernstein. A quantitative analysis of hydrogen trapping. *Metallurgical Transactions A*, 9(11):1571–1580, November 1978. ISSN 1543-1940.

[19] C. Moriconi. *Modélisation de la propagation de fissure de fatigue assistée par l'hydrogène gazeux dans les matériaux métalliques*. PhD thesis, SAE-ENSMA Ecole Nationale Supérieure de Mécanique et d'Aérotechique-Poitiers, 2012.

[20] M. A. Stopher and P. E. J. Rivera-Diaz-del Castillo. Hydrogen embrittlement in bearing steels. *Materials Science and Technology*, 32:11:1184–1193, 2016.

[21] G. Gobbi. *Modelling of hydrogen embrittlement phenomenon: different prespectives and dimensional scales*. PhD thesis, Politecnico di Milano, April 2016.

[22] A. H. M. Krom, R. W. J. Koers, and A. Bakker. Hydrogen transport near a blunting crack tip. *Journal of the Mechanics and Physics of Solids*, 47(4): 971–992, February 1999. ISSN 0022-5096.

[23] S. He, W. Ecker, R. Pippan, and V. I. Razumovskiy. Hydrogen-enhanced decohesion mechanism of the special 5(012)[100] grain boundary in Ni with Mo and C solutes. *Computational Materials Science*, 167:100–110, September 2019. ISSN 0927-0256.

[24] L. B. Pfeil and H. C. H. Carpenter. The effect of occluded hydrogen on the tensile strength of iron. *Proceedings of the Royal Society of London. Series A, Containing Papers of a Mathematical and Physical Character*, 112(760): 182–195, August 1926. Publisher: Royal Society.

[25] A. R. Troiano. The Role of Hydrogen and Other Interstitials in the Mechanical Behavior of Metals. *Metallography, Microstructure, and Analysis*, 5(6): 557–569, 1960. ISSN 2192-9270.

[26] G. M. Pressouyre. Trap theory of Hydrogen embrittlement. *Acta Metallurgica*, 28(7):895–911, July 1980. ISSN 0001-6160.

[27] S. Lynch. Hydrogen embrittlement phenomena and mechanisms. *Corrosion Reviews*, 30(3-4):105–123, June 2012. ISSN 0334-6005, 2191-0316.

[28] A. Van der Ven and G. Ceder. Impurity-induced van der Waals transition during decohesion. *Physical Review B*, 67(6):060101, February 2003. Publisher: American Physical Society.

[29] S. Wang, M. L. Martin, I. M. Robertson, and P. Sofronis. Effect of hydrogen environment on the separation of Fe grain boundaries. *Acta Materialia*, 107: 279–288, April 2016. ISSN 1359-6454.

[30] H. Vehoff and P. Neumann. Crack propagation and cleavage initiation in Fe-2.6%-Si single crystals under controlled plastic crack tip opening rate in various gaseous environments. *Acta Metallurgica*, 28(3):265–272, March 1980. ISSN 0001-6160.

[31] M. Möhle. Numerical investigation on hydrogen embrittlement of metallic pipeline structures. *Institut für Baumechanik und Numerische Mechanik;F18/3*, 2018.

[32] C. D. Beachem. A new model for hydrogen-assisted cracking (hydrogen "embrittlement"). *Metallurgical and Materials Transactions B*, 3(2):441–455, February 1972. ISSN 1543-1916.

[33] G. Lu, Q. Zhang, N. Kioussis, and E. Kaxiras. Hydrogen-enhanced local plasticity in aluminum: an ab initio study. *Physical Review Letters*, 87(9): 095501, August 2001. ISSN 0031-9007.

[34] I. M. Robertson. The effect of hydrogen on dislocation dynamics. *Engineering Fracture Mechanics*, 68(6):671–692, April 2001. ISSN 0013-7944.

[35] S. P. Lynch. A fractographic study of hydrogen-assisted cracking and liquid-metal embrittlement in nickel. *Journal of Materials Science*, 21(2):692–704, February 1986. ISSN 1573-4803.

[36] R. P. Gangloff. Hydrogen assisted cracking of high strength alloys. In *Comprehensive Structural Integrity*, volume 6, pages 31–101. Elsevier Science, i. milne, r.o. ritchie and b. karihaloo edition, 2003.

[37] O. Barrera, D. Bombac, Y. Chen, T. D. Daff, E. Galindo-Nava, P. Gong, D. Haley, R. Horton, I. Katzarov, J. R. Kermode, C. Liverani, M. Stopher, and F. Sweeney. Understanding and mitigating hydrogen embrittlement of steels: a review of experimental, modelling and design progress from atomistic to continuum. *Journal of Materials Science*, 53(9):6251–6290, 2018. ISSN 0022-2461.

[38] R. G. Hoagland and H. L. Heinisch. An atomic simulation of the influence of hydrogen on the fracture behavior of nickel. *Journal of Materials Research*, 7(8):2080–2088, August 1992. ISSN 2044-5326, 0884-2914. Publisher: Cambridge University Press.

[39] H. K. Birnbaum. Hydrogen Related Fracture of Metals. In R. M. Latanision and J. R. Pickens, editors, *Atomistics of Fracture*, pages 733–769. Springer US, Boston, MA, 1983. ISBN 978-1-4613-3500-9.

[40] W. Brocks, R. Falkenberg, and I. Scheider. Coupling aspects in the simulation of hydrogen-induced stress-corrosion cracking. *Procedia IUTAM*, 3:11–24, January 2012. ISSN 2210-9838.

[41] G. Gobbi, C. Colombo, S. Miccoli, and L. Vergani. A fully coupled implementation of hydrogen embrittlement in FE analysis. *Advances in Engineering Software*, 135:102673, September 2019. ISSN 0965-9978.

[42] V. Olden, C. Thaulow, R. Johnsen, E. Østby, and T. Berstad. Influence of hydrogen from cathodic protection on the fracture susceptibility of 25%Cr duplex stainless steel, Constant load SENT testing and FE-modelling using hydrogen influenced cohesive zone elements. *Engineering Fracture Mechanics*, 76(7):827–844, May 2009. ISSN 0013-7944.

[43] V. Olden, A. Alvaro, and O. M. Akselsen. Hydrogen diffusion and hydrogen influenced critical stress intensity in an API X70 pipeline steel welded joint – Experiments and FE simulations. *International Journal of Hydrogen Energy*, 37(15):11474–11486, August 2012. ISSN 0360-3199.

[44] A. Alvaro, V. Olden, and O. M. Akselsen. 3D cohesive modelling of hydrogen embrittlement in the heat affected zone of an X70 pipeline steel. *International Journal of Hydrogen Energy*, 38(18):7539–7549, June 2013. ISSN 0360-3199.

[45] A. Alvaro, V. Olden, and O. M. Akselsen. 3D cohesive modelling of hydrogen embrittlement in the heat affected zone of an X70 pipeline steel – Part II. *International Journal of Hydrogen Energy*, 39(7):3528–3541, February 2014. ISSN 0360-3199.

[46] G. Gobbi, C. Colombo, S. Miccoli, and L. Vergani. A weakly coupled implementation of hydrogen embrittlement in FE analysis. *Finite Elements in Analysis and Design*, 141:17–25, March 2018. ISSN 0168-874X.

[47] F.Q. Yang, W.J. Zhan, T. Yan, H.B. Zhang, and X.R. Fang. Numerical Analysis of the Coupling between Hydrogen Diffusion and Mechanical Behavior near the Crack Tip of Titanium. *Mathematical Problems in Engineering*, 2020. ISSN 1024-123X.

[48] C. Moriconi, G. Hénaff, and D. Halm. Cohesive zone modeling of fatigue crack propagation assisted by gaseous hydrogen in metals. *International Journal of Fatigue*, 68:56–66, November 2014. ISSN 0142-1123.

[49] M. C. Vasco, K. Tserpes, and S. G. Pantelakis. Numerical Simulation of Tensile Behavior of Corroded Aluminum Alloy 2024 T3 Considering the Hydrogen Embrittlement. *Metals*, 8(1):56, January 2018.

[50] D. Setsika, K. Tserpes, and S. Pantelakis. Numerical simulation of tensile behavior of corroded aluminum alloy 2024 T3. *International Journal of Structural Integrity*, 6(4):451–467, January 2015. ISSN 1757-9864. Publisher: Emerald Group Publishing Limited.

[51] R. F. Decker, C. J. Novak, and T. W. Landig. Developments and projected trends in maraging steels. *JOM*, 19(11):60–66, November 1967. ISSN 1543-1851.

[52] A. Shekhter, H. I. Aaronson, M. R. Miller, S. P. Ringer, and E. V. Pereloma. Effect of aging and deformation on the microstructure and properties of Fe-Ni-Ti maraging steel. *Metallurgical and Materials Transactions A*, 35(3): 973–983, March 2004. ISSN 1543-1940.

[53] J. A. Psioda and J. R. Low. The effect of microstructure and strength on the fracture toughness of an 18 Ni, 300 grade maraging steel. Technical report, NASA, November 1977.

[54] B. Rohit and N. R. Muktinutalapati. Austenite reversion in 18% Ni maraging steel and its weldments. *Materials Science and Technology*, 34(3):253–260, February 2018. ISSN 0267-0836.

[55] J. M. Pardal, S. S. M. Tavares, V. F. Terra, M. R. Da Silva, and D. R. Dos Santos. Modeling of precipitation hardening during the aging and overaging of 18Ni–Co–Mo–Ti maraging 300 steel. *Journal of Alloys and Compounds*, 393(1):109–113, May 2005. ISSN 0925-8388.

[56] R. Tewari, S. Mazumder, I. S. Batra, G. K. Dey, and S. Banerjee. Precipitation in 18 wt% Ni maraging steel of grade 350. *Acta Materialia*, 48(5): 1187–1200, March 2000. ISSN 1359-6454.

[57] L. G. de Carvalho, R. L. Plaut, M. A. de Martorano, and A. F. Padilha. Study of Age Hardening Behavior in a 350 Grade Maraging Steel. In *Characterization of Minerals, Metals, and Materials 2015*, pages 3–10. Springer International Publishing, Cham, 2016. ISBN 978-3-319-48191-3.

[58] S. Hossein Nedjad, S. Meimandi, A. Mahmoudi, T. Abedi, S. Yazdani, H. Shirazi, and M. Nili Ahmadabadi. Effect of aging on the microstructure and tensile properties of Fe–Ni–Mn–Cr maraging alloys. *Materials Science and Engineering: A*, 501(1):182–187, February 2009. ISSN 0921-5093.

[59] U. K. Viswanathan, G. K. Dey, and V. Sethumadhavan. Effects of austenite reversion during overageing on the mechanical properties of 18 Ni (350) maraging steel. *Materials Science and Engineering: A*, 398(1):367–372, May 2005. ISSN 0921-5093.

[60] E. I. Galindo-Nava, W. M. Rainforth, and P. E. J. Rivera-Díaz-del Castillo. Predicting microstructure and strength of maraging steels: Elemental optimisation. *Acta Materialia*, 117:270–285, September 2016. ISSN 1359-6454.

[61] H. Kitahara, R. Ueji, N. Tsuji, and Y. Minamino. Crystallographic features of lath martensite in low-carbon steel. *Acta Materialia*, 54(5):1279–1288, March 2006. ISSN 1359-6454.

[62] S. Morito, H. Tanaka, R. Konishi, T. Furuhara, and T. Maki. The morphology and crystallography of lath martensite in Fe-C alloys. *Acta Materialia*, 51(6):1789–1799, April 2003. ISSN 1359-6454.

[63] R. L Fleischer. Substitutional solution hardening. *Acta Metallurgica*, 11(3): 203–209, March 1963. ISSN 0001-6160.

[64] E. V. Pereloma, A. Shekhter, M. K. Miller, and S. P. Ringer. Ageing behaviour of an Fe–20Ni–1.8Mn–1.6Ti–0.59Al (wt%) maraging alloy: clustering, precipitation and hardening. *Acta Materialia*, 52(19):5589–5602, November 2004. ISSN 1359-6454.

[65] I. Gibson, D. W. Rosen, and B. Stucker. Development of Additive Manufacturing Technology. In *Additive Manufacturing Technologies: Rapid Prototyping to Direct Digital Manufacturing*, pages 36–58. Springer US, Boston, MA, 2010. ISBN 978-1-4419-1120-9.

[66] Deloitte University Press. 3D opportunity in aerospace and defense: Additive manufacturing takes flight.

[67] W. E. Frazier. Metal Additive Manufacturing: A Review. *Journal of Materials Engineering and Performance*, 23(6):1917–1928, June 2014. ISSN 1544-1024.

[68] K. V. Wong and A. Hernandez. A Review of Additive Manufacturing. *ISRN Mechanical Engineering*, August 2012.

[69] T. DebRoy, H. L. Wei, J. S. Zuback, T. Mukherjee, J. W. Elmer, J. O. Milewski, A. M. Beese, A. Wilson-Heid, A. De, and W. Zhang. Additive manufacturing of metallic components – Process, structure and properties. *Progress in Materials Science*, 92:112–224, March 2018. ISSN 0079-6425.

[70] S. W. Baek, E. J. Song, J. H. Kim, M. Jung, U. B. Baek, and S. H. Nahm. Hydrogen embrittlement of 3-D printing manufactured austenitic stainless steel part for hydrogen service. *Scripta Materialia*, 130:87–90, March 2017. ISSN 1359-6462.

[71] C. Katsarelis. Additive Manufacturing of NASA HR-1 Material for Liquid Rocket Engine Component Applications. Tampa, FL, United States, December 2019.

[72] S. Afkhami, M. Dabiri, S. H. Alavi, T. Björk, and A. Salminen. Fatigue characteristics of steels manufactured by selective laser melting. *International Journal of Fatigue*, 122:72–83, May 2019. ISSN 0142-1123.

[73] R. Mertens, S. Dadbakhsh, J. Van Humbeeck, and J. P. Kruth. Application of base plate preheating during selective laser melting. *Procedia CIRP*, 74: 5–11, January 2018. ISSN 2212-8271.

[74] K. G. Prashanth, S. Scudino, and J. Eckert. Defining the tensile properties of Al-12Si parts produced by selective laser melting. *Acta Materialia*, 126: 25–35, March 2017. ISSN 1359-6454.

[75] P. J. Withers and H. K. D. H. Bhadeshia. Residual stress. Part 1 – Measurement techniques. *Materials Science and Technology*, 17(4):355–365, April 2001. ISSN 0267-0836.

[76] P. J. Withers and H. K. D. H. Bhadeshia. Residual stress. Part 2 – Nature and origins. *Materials Science and Technology*, 17(4):366–375, April 2001. ISSN 0267-0836.

[77] P. J. Withers. Residual stress and its role in failure. *Reports on Progress in Physics*, 70(12):2211–2264, December 2007. ISSN 0034-4885, 1361-6633.

[78] K. Kempen, L. Thijs, B. Vrancken, S. Buls, J. Van Humbeeck, and J. P. Kruth. Producing crack-free, high density M2 HSS parts by Selective Laser Melting: Pre-heating the baseplate. In *24th International SFF Symposium - An Additive Manufacturing Conference, SFF 2013*, pages 131–139, 2013.

[79] L. E. Loh, C.K. Chua, W.Y. Yeong, J. Song, M. Mapar, S.L. Sing, Z.H. Liu, and D.Q. Zhang. Numerical investigation and an effective modelling on the Selective Laser Melting (SLM) process with aluminium alloy 6061. *International Journal of Heat and Mass Transfer*, 80:288–300, January 2015. ISSN 0017-9310.

[80] A. V. Gusarov and I. Smurov. Modeling the interaction of laser radiation with powder bed at selective laser melting. *Physics Procedia*, 5:381–394, January 2010. ISSN 1875-3892.

[81] W. King, A. T. Anderson, R. M. Ferencz, N. E. Hodge, C. Kamath, and S. A. Khairallah. Overview of modelling and simulation of metal powder bed fusion process at Lawrence Livermore National Laboratory. *Materials Science and Technology*, 31(8):957–968, June 2015. ISSN 0267-0836.

[82] D. Junker, O. Hentschel, M. Schmidt, and M. Merklein. Investigation of Heat Treatment Strategies for Additively-Manufactured Tools of X37CrMoV5-1. *Metals*, 8(10):854, October 2018. Number: 10 Publisher: Multidisciplinary Digital Publishing Institute.

[83] C. Tan, K. Zhou, M. Kuang, W. Ma, and T. Kuang. Microstructural characterization and properties of selective laser melted maraging steel with different build directions. *Science and Technology of Advanced Materials*, 19(1): 746–758, December 2018. ISSN 1468-6996.

[84] Y. Bai, Y. Yang, D. Wang, and M. Zhang. Influence mechanism of parameters process and mechanical properties evolution mechanism of maraging steel 300 by selective laser melting. *Materials Science and Engineering: A*, 703: 116–123, August 2017. ISSN 0921-5093.

[85] C. Tan, K. Zhou, W. Ma, P. Zhang, M. Liu, and T. Kuang. Microstructural evolution, nanoprecipitation behavior and mechanical properties of selective laser melted high-performance grade 300 maraging steel. *Materials & Design*, 134:23–34, November 2017. ISSN 0264-1275.

[86] E. A. Jägle, Z. Sheng, P. Kürnsteiner, S. Ocylok, A. Weisheit, and D. Raabe. Comparison of Maraging Steel Micro- and Nanostructure Produced Conventionally and by Laser Additive Manufacturing. *Materials*, 10(1):8, January 2017. Number: 1 Publisher: Multidisciplinary Digital Publishing Institute.

[87] S. Yin, C. Chen, X. Yan, X. Feng, R. Jenkins, P. O'Reilly, M. Liu, H. Li, and R. Lupoi. The influence of aging temperature and aging time on the mechanical and tribological properties of selective laser melted maraging 18Ni-300 steel. *Additive Manufacturing*, 22:592–600, August 2018. ISSN 2214-8604.

[88] R. Casati, J. N. Lemke, A. Tuissi, and M. Vedani. Aging Behaviour and Mechanical Performance of 18-Ni 300 Steel Processed by Selective Laser Melting. *Metals*, 6(9):218, September 2016. Number: 9 Publisher: Multidisciplinary Digital Publishing Institute.

[89] K. Kempen, E. Yasa, L. Thijs, J. P. Kruth, and J. Van Humbeeck. Microstructure and mechanical properties of Selective Laser Melted 18Ni-300 steel. *Physics Procedia*, 12:255–263, January 2011. ISSN 1875-3892.

[90] T. H. Becker and D. Dimitrov. The achievable mechanical properties of SLM produced Maraging Steel 300 components. *Rapid Prototyping Journal*, 22 (3):487–494, January 2016. ISSN 1355-2546. Publisher: Emerald Group Publishing Limited.

[91] L. Kučerová, I. Zetková, A. Jandová, and M. Bystrianský. Microstructural characterisation and in-situ straining of additive-manufactured X3NiCoMoTi 18-9-5 maraging steel. *Materials Science and Engineering: A*, 750:70–80, March 2019. ISSN 0921-5093.

[92] P. Bajaj, A. Hariharan, A. Kini, P. Kürnsteiner, D. Raabe, and E. A. Jägle. Steels in additive manufacturing: A review of their microstructure and properties. *Materials Science and Engineering: A*, 772:138633, January 2020. ISSN 0921-5093.

[93] Y. J. Kwon, R. Casati, M. Coduri, M. Vedani, and C. S. Lee. Hydrogen Embrittlement Behavior of 18Ni 300 Maraging Steel Produced by Selective Laser Melting. *Materials*, 12(15), July 2019. ISSN 1996-1944.

[94] X. Li, Q. Li, T. Wang, and J. Zhang. Hydrogen-assisted failure of laser melting additive manufactured IN718 superalloy. *Corrosion Science*, 160, 2019.

[95] E28 Committee. Test Methods for Tension Testing of Metallic Materials. Technical report, ASTM International.

[96] L. M. Haldorsen, B. Nyhus, and G. Rørvik. Hydrogen Induced Stress Cracking of Superduplex Steels: Effect of Operation Temperature. American Society of Mechanical Engineers Digital Collection, September 2018.

[97] S.L. Robinson, B.P. Somerday, and N.R. Moody. Hydrogen embrittlement of stainless steels.

[98] E08 Committee. Test Method for Measurement of Fracture Toughness. Technical report, ASTM International.

[99] X. Zhu. Progress in development of fracture toughness test methods for SENT specimens. *International Journal of Pressure Vessels and Piping*, 156: 40–58, September 2017. ISSN 0308-0161.

[100] C. Colombo, Gabriele Fumagalli, F. Bolzoni, G. Gobbi, and L. Vergani. Fatigue behavior of hydrogen pre-charged low alloy Cr–Mo steel. *International Journal of Fatigue*, 83:2–9, February 2016. ISSN 0142-1123.

[101] F. Bolzoni, P. Fassina, G. Fumagalli, L. Lazzari, and G. Re. Hydrogen charging of carbon and low alloy steel by electrochemical methods. 2010.

[102] C. Arvieu, C. Galy, E. Le Guen, and E. Lacoste. Relative Density of SLM-Produced Aluminum Alloy Parts: Interpretation of Results. *Journal of Manufacturing and Materials Processing*, 4(3):83, September 2020. Number: 3 Publisher: Multidisciplinary Digital Publishing Institute.

[103] M. Bayat, A. Thanki, S. Mohanty, A. Witvrouw, S. Yang, J. Thorborg, N. S. Tiedje, and J. H. Hattel. Keyhole-induced porosities in Laser-based Powder Bed Fusion (L-PBF) of Ti6Al4V: High-fidelity modelling and experimental validation. *Additive Manufacturing*, 30:100835, December 2019. ISSN 2214-8604.

[104] D. Wang, S. Wu, F. Fu, S. Mai, Y. Yang, Y. Liu, and C. Song. Mechanisms and characteristics of spatter generation in SLM processing and its effect on the properties. *Materials & Design*, 117:121–130, March 2017. ISSN 0264-1275.

[105] A.B. Spierings, M. Schneider, and R. Eggenberger. Comparison of density measurement techniques for additive manufactured metallic parts. *Rapid Prototyping Journal*, 17(5):380–386, January 2011. ISSN 1355-2546. Publisher: Emerald Group Publishing Limited.

[106] M. H. Nasab, D. Gastaldi, N. F. Lecis, and M. Vedani. On morphological surface features of the parts printed by selective laser melting (SLM). *Additive Manufacturing*, 24:373–377, December 2018. ISSN 2214-8604.

[107] D. S. Dugdale. Yielding of steel sheets containing slits. *Journal of the Mechanics and Physics of Solids*, 8(2):100–104, May 1960. ISSN 0022-5096.

[108] G. I. Barenblatt. The Mathematical Theory of Equilibrium Cracks in Brittle Fracture. In H. L. Dryden, Th. von Kármán, G. Kuerti, F. H. van den Dungen, and L. Howarth, editors, *Advances in Applied Mechanics*, volume 7, pages 55–129. Elsevier, January 1962.

[109] M. Ortiz and A. Pandolfi. Finite-deformation irreversible cohesive elements for three-dimensional crack-propagation analysis. *International Journal for Numerical Methods in Engineering*, 44(9):1267–1282, 1999. ISSN 1097-0207.

[110] G. Allegri. A unified formulation for fatigue crack onset and growth via cohesive zone modelling. *Journal of the Mechanics and Physics of Solids*, 138:103900, May 2020. ISSN 0022-5096.

[111] K. H. Schwalbe, I. Scheider, and A. Cornec. *Guidelines for Applying Cohesive Models to the Damage Behaviour of Engineering Materials and Structures*. SpringerBriefs in Applied Sciences and Technology. Springer-Verlag, Berlin Heidelberg, 2013. ISBN 978-3-642-29493-8.

[112] M. Kuna and S. Roth. General remarks on cyclic cohesive zone models. *International Journal of Fracture*, 196(1):147–167, November 2015. ISSN 1573-2673.

[113] V. Tvergaard and J. W. Hutchinson. The relation between crack growth resistance and fracture process parameters in elastic-plastic solids. *Journal of the Mechanics and Physics of Solids*, 40(6):1377–1397, August 1992. ISSN 0022-5096.

[114] I. Scheider and W. Brocks. The Effect of the Traction Separation Law on the Results of Cohesive Zone Crack Propagation Analyses. *Key Engineering Materials*, 251-252:313–318, 2003. ISSN 1662-9795.

[115] Abaqus 6.13 Online Documentation.

[116] S. Serebrinsky, E. A. Carter, and M. Ortiz. A quantum-mechanically informed continuum model of hydrogen embrittlement. *Journal of the Mechanics and Physics of Solids*, 52(10):2403–2430, October 2004. ISSN 0022-5096.

[117] D. E. Jiang and E. A. Carter. First principles assessment of ideal fracture energies of materials with mobile impurities: implications for hydrogen embrittlement of metals. *Acta Materialia*, 52(16):4801–4807, September 2004. ISSN 1359-6454.

[118] E. D. Hondros and M. P. Seah. The theory of grain boundary segregation in terms of surface adsorption analogues. *Metallurgical Transactions A*, 8: 1363–1371, September 1977.

[119] A. J. Kumnick and H. H. Johnson. Deep trapping states for hydrogen in deformed iron. *Acta Metallurgica*, 28(1):33–39, January 1980. ISSN 0001-6160.

[120] K. Khan and A. De. Modelling of selective laser melting process with adaptive remeshing. *Science and Technology of Welding and Joining*, 24(5):391–400, July 2019. ISSN 1362-1718.

[121] A. K. Ibraheem, B. Derby, and P. J. Withers. Thermal and Residual Stress Modelling of the Selective Laser Sintering Process. *MRS Online Proceedings Library Archive*, 758, 2002. ISSN 0272-9172, 1946-4274. Publisher: Cambridge University Press.

[122] M. J. Anderson, J. Benson, J. W. Brooks, B. Saunders, and H. C. Basoalto. Predicting Precipitation Kinetics During the Annealing of Additive Manufactured Inconel 625 Components. *Integrating Materials and Manufacturing Innovation*, 8(2):154–166, June 2019. ISSN 2193-9772.

[123] J. Guo, H. Fu, B. Pan, and R. Kang. Recent progress of residual stress measurement methods: A review. *Chinese Journal of Aeronautics*, November 2019. ISSN 1000-9361.

[124] Y. Momotani, A. Shibata, D. Terada, and N. Tsuji. Effect of strain rate on hydrogen embrittlement in low-carbon martensitic steel. *International Journal of Hydrogen Energy*, 42(5):3371–3379, February 2017. ISSN 0360-3199.

[125] H. Yu, J. S. Olsen, A. Alvaro, V. Olden, J. He, and Z. Zhang. A uniform hydrogen degradation law for high strength steels. *Engineering Fracture Mechanics*, 157:56–71, May 2016. ISSN 0013-7944.

[126] P. Fassina, M. F. Brunella, L. Lazzari, G. Re, L. Vergani, and A. Sciuccati. Effect of hydrogen and low temperature on fatigue crack growth of pipeline steels. *Engineering Fracture Mechanics*, 103:10–25, May 2013. ISSN 0013-7944.

[127] L. Jemblie, V. Olden, and O. M. Akselsen. A coupled diffusion and cohesive zone modelling approach for numerically assessing hydrogen embrittlement of steel structures. *International Journal of Hydrogen Energy*, 42(16):11980–11995, April 2017. ISSN 0360-3199.

[128] M. Barsanti, M. Beghini, F. Frasconi, R. Ishak, B. D. Monelli, and R. Valentini. Experimental study of hydrogen embrittlement in Maraging steels. *Procedia Structural Integrity*, 8:501–508, January 2018. ISSN 2452-3216.

[129] T. Ohnishi, K. Higashi, N. Inoue, and Y. Nakatani. Effect of Temperature and Strain Rate on Hydrogen Embrittlement of an Al-8%Mg Alloy. *Journal of the Japan Institute of Metals*, 45(9):972–976, 1981.

[130] J. Brown and W. Baldwin. Hydrogen embrittlement of steels. *Trans. AIME*, 200:298–303, 1954.

[131] Y. Nam, J. Park, U. Baek, J. Suh, and S. Nahm. Low-temperature tensile and impact properties of hydrogen-charged high-manganese steel. *International Journal of Hydrogen Energy*, 44(13):7000–7013, March 2019. ISSN 0360-3199.

[132] R. Valentini, C. Colombo, M. De Sanctis, and G. Lovicu. Hydrogen Re-Embrittlement of Aerospace grade High Strength Steels. *Frattura ed Integrità Strutturale*, 6(21):30–36, June 2012. ISSN 1971-8993. Number: 21.

[133] L. W. Tsay, Y. F. Hu, and C. Chen. Embrittlement of T-200 maraging steel in a hydrogen sulfide solution. *Corrosion Science*, 47(4):965–976, April 2005. ISSN 0010-938X.

[134] R. Thomas, D. Li, R. Gangloff, and J. Scully. Trap-governed hydrogen diffusivity and uptake capacity in ultrahigh-strength AERMET 100 steel. *Metallurgical and Materials Transactions A*, 33(7):1991–2004, July 2002. ISSN 1543-1940.

Appendix A

Listings

A.1 Stress_extraction.py

```
from odbAccess import *
from abaqusConstants import *
import re

# open the .odb file
odb = openOdb('noH.odb')

# open the file where the stresses are saved
reportfile_name = 'report_S.txt'
reportfile = open(reportfile_name, 'w')

step1 = odb.steps['Equilibrium']
# select the last increment
frame = step1.frames[-1]
stens = frame.fieldOutputs['S']
# select all the solid elements
elms = odb.rootAssembly.instances['PART-1-1'].elementSets['HYDRA']
stens_at_elms = stens.getSubset(region=elms)
fieldValues = stens_at_elms.values

for v in fieldValues:
  # save element number and the 4 stress components
  no=v.elementLabel
  s=v.data
  s11 = s[0]
  s22 = s[1]
  s33 = s[2]
  s12 = s[3]
  reportstr = str(no) + ' ' + str(s11) + ' ' + str(s22) + ' ' + str(
    s33) + ' ' + str(s12) + '\n'
  reportfile.write(reportstr)

reportfile.close()
```

A.2 Sigini.f

```
      SUBROUTINE SIGINI(SIGMA,COORDS,NTENS,NCRDS,NOEL,NPT,LAYER,
     1 KSPT,LREBAR,NAMES)
C
      INCLUDE 'ABA_PARAM.INC'
C
      DIMENSION SIGMA(NTENS),COORDS(NCRDS)
      CHARACTER NAMES(2)*80
      CHARACTER*256 OUTDIR
C
C     read from file
      integer, dimension(13125) :: el
      real, dimension(13125) :: s11, s22, s33, s12
C
C     number of elements
      elmax =13125
      if (NOEL .EQ. 1) THEN
C     open the file with the stress values
          CALL GETOUTDIR(OUTDIR, LENOUTDIR)
          open(unit=1,status='old',file=OUTDIR(1:LENOUTDIR)
     +//'/report_S.txt')
        do i=1, elmax
            read(1,*) el(i), s11(i), s22(i), s33(i), s12(i)
        end do
          close(unit=1)
      end if
C
      do i=1, elmax
C     impose the stress values elements by element
C     example: times -5
          if (el(i) .eq. NOEL) then
              SIGMA(1) = -5*s11(i)
              SIGMA(2) = -5*s22(i)
              SIGMA(3) = -5*s33(i)
              SIGMA(4) = 5*s12(i)
          end if
      end do
C
      RETURN
      END
```

A.3 Report.py

```
from odbAccess import *
from abaqusConstants import *

# open the .odb file
odb = openOdb('noH.odb')
step1 = odb.steps['Step-1']

# select the first node with cohesive elements (crack tip)
region = step1.historyRegions['Node PART-1-1.769']

# vertical displacement
u2Data = region.historyOutputs['U2'].data
```

```
reportfile_name='report_CTOD.txt'
reportfile=open(reportfile_name,'w')

for time, u2Disp in u2Data:
    reportfile.write('%10.4E\n' % (u2Disp))
reportfile.close()

spaces = '                    '
keys = odb.steps.keys()
for key in keys:
  step = odb.steps[key]

reportfile_name = 'report_F.txt'
reportfile = open(reportfile_name, 'w')
frameRepository = step.frames
if len(frameRepository):
  for frame in frameRepository:
    id = frame.frameId
    forces = frame.fieldOutputs['RF']

    # nodes at the top edge
    nodes = odb.rootAssembly.instances['PART-1-1'].nodeSets['TOP']
    force_at_nodes = forces.getSubset(region=nodes)
    fieldValues = force_at_nodes.values
    for v in fieldValues:
      no = v.nodeLabel
      s = v.data[1]

      # save node number and corresponding force
      reportstr = str(no) + spaces + str(s)
      reportfile.write(reportstr + '\n')
reportfile.close()

reportfile_name = 'report_U2.txt'
reportfile = open(reportfile_name, 'w')
if len(frameRepository):
  for frame in frameRepository:
    id = frame.frameId
    reportstr = str(id)
    disps = frame.fieldOutputs['U']

    # nodes of the solid elements connected to the cohesive ones
    nodes = odb.rootAssembly.instances['PART-1-1'].nodeSets['EQREAL']
    disp_at_nodes = disps.getSubset(region=nodes)
    fieldValues = disp_at_nodes.values
    for v in fieldValues:
      no = v.nodeLabel
      # direction 2
      s = v.data[1]
      reportstr = str(id) + spaces + str(no) + spaces + str(s)
      reportfile.write(reportstr + '\n')

reportfile.close()
```

A.4 Optimization.py

```
import os
import matlab.engine
import numpy as np
import time
import re
from shutil import copy2
from shutil import rmtree

# needed for initialization
def remove_file(name):
    if os.path.isfile(name):
        os.remove(name)


# remove files from previous runs and create dev.txt and top3 folder
def initialize():
    # delete files from previous runs
    files = ['dev.txt', 'noh.lck']
    for file in files:
        remove_file(file)

    dev_file = open('dev.txt', 'w')
    dev_str = ('delta_0          delta_N          delta_F'
               '          sigma       deviation         advancement\n')
    dev_file.write(dev_str)
    dev_file.close()

    # delete top3 folder and create a new one
    if os.path.isdir(t3wd):
        rmtree(t3wd)
    os.mkdir(t3wd)


# pass tsl parameters to matlab
def write_tsl_file(d_0, d_N, d_F, s):
    tsl_par = open('tsl_par.txt', 'w')
    tsl_par.write(str(d_0) + ', ' + str(d_N) + ', ' + str(d_F) + ', '
    + str(s))
    tsl_par.close()


# send abaqus job and report.py
def job_report(d_0, d_N, d_F, s):
    write_tsl_file(d_0, d_N, d_F, s)

    # create tsl
    eng = matlab.engine.start_matlab()
    eng.Damaging(nargout=0)
    eng.quit()

    # run abaqus
    os.system('abaqus j=noh')

    # wait for .lck creation
```

```
54      time.sleep(20)
55
56      # wait while analysis is running
57      while os.path.isfile('noh.lck'):
58          True
59
60      # run report
61      os.system('abaqus python Report.py')
62
63
64  # sort the dev.txt file by smallest deviation
65  def sort_results(lim):
66      data_raw = np.loadtxt('dev.txt', skiprows=1)
67      count = 0
68      rem = []
69      try:
70          for line in data_raw:
71              if line[5] < lim:
72                  rem.append(count)
73                  count += 1
74          data = np.delete(data_raw, rem, 0)
75          data_sorted = data[data[:, 4].argsort()]
76          return data_sorted
77      # exception happens when there is only one line (after the first
        simulation)
78      except:
79          return data_raw
80
81
82  # obtain deviation vs experimental and save the .odb in in the top 3
        folder
83  def run_analysis(d_0, d_N, d_F, s, n_run):
84      job_report(d_0, d_N, d_F, s)
85
86      # run script to analyze crack propagation
87      eng = matlab.engine.start_matlab()
88      eng.Results_noH(nargout=0)
89      eng.quit()
90
91      # check analysis advancement and save it
92      sta_file = open('noh.sta', 'r')
93      last3 = (sta_file.readlines()[-3:])
94      string = re.split('\s+', last3[0])
95      adv = string[7]
96      sta_file.close()
97
98      dev_file = open('dev.txt', 'a')
99      dev_file.write('          ' + adv + '\n')
100     dev_file.close()
101
102     # order results and save odb if top 3
103     if float(adv) > lim:
104         data_sorted = sort_results(lim)
105         # check if tsl parameters are in the first 3 lines and save
        position
106         top3 = False
```

```
107         # round to avoid numerical errors
108         d_N = round(d_N, 5)
109         d_F = round(d_F, 5)
110         # depending on the number of analyses done
111         if n_run == 0:
112             top3 = True
113             pos = 0
114         else:
115             if n_run == 1:
116                 topn = 2
117             else:
118                 topn = 3
119             for idx in range(topn):
120                 for line in data_sorted[idx:idx + 1, :]:
121                     if set([d_0, d_F, d_N, s]).issubset(line):
122                         top3 = True
123                         pos = idx
124 
125         # save .odb --> have to move down the ranking when a new one
    comes
126         if top3:
127             nfile = t3wd + 'noh_' + str(pos) + '.odb'
128             if pos < 2:
129                 if os.path.isfile(nfile):
130                     nfile_moved = t3wd + 'noh_' + str(pos+1) + '.odb'
131                     copy2(nfile, nfile_moved)
132             copy2('noh.odb', nfile)
133 
134 
135 
136 # acceptable advancement limit
137 global lim
138 lim = 0.5
139 
140 # top3 directory
141 global t3wd
142 t3wd = os.getcwd() + '/top3/'
143 
144 # initialize sum up file
145 initialize()
146 
147 # tsl parameters for all the combinations
148 n_run = 0
149 for d_0 in np.arange(0.0002, 0.0016, 0.0002):
150     for d_N in np.arange(0.002,0.015,0.0005):
151         for d_F in np.arange(0.02,0.07,0.005):
152             for s in np.arange(3650, 3900, 50):
153                 run_analysis(d_0, d_N, d_F, s, n_run)
154                 n_run += 1
155 
156 # extract the best 3 and save txt
157 data_sorted = sort_results(lim)
158 np.savetxt('sorted.txt', data_sorted, fmt='%6.6f, %6.6f, %6.6f, %6.0f
    , %6.1f, %6.2f')
```

A.5 Results.m

```
% import tsl parameters written by python script
pars = load('tsl_par.txt');
delta_0 = pars(1);
deltaN = pars(2);
deltaF = pars(3);
sigma_0 = pars(4);

load DATA_CRACK_noH_4130.mat
% loading experimental data with variables:
% CTOD_exp_H
% Da_exp_H
load Coord.mat
% loading Coord matrix, nx2, with n node number, columns:
% 1:nodes ordered from the crack tip (the first one is the crack tip)
% 2:distance from the tip

% displacements must be doubled, as only half specimen is modelled
CTOD=load('report_CTOD.txt');  CTOD=2*CTOD;
U2=load('report_U2.txt');
% matrix (n_allxi)x3, n_all=all nodes on the symmetry axis, i=
    increment;
% columns: 1: increment, 2:node, 3:U2

% i=cycling over active ordered nodes
% j=cycling over all ordered symmetry nodes
% k=cycling over the step increments
i_max=length(Coord);
j_max=311; % Crack tip ID
k_max=length(U2)/j_max;

%% Estimating Delta_a, crack length advancement
for k=1:k_max
    for i=1:i_max
        for j=1:j_max
            if Coord(i,1)==U2((k-1)*j_max+j,2)
                if U2((k-1)*j_max+j,3)>=deltaF
                    Coord(i,3)=1;
                else
                    Coord(i,3)=0;
                end
            end
        end
    end
    i=1;
    while Coord(i,3)==0 && i<i_max
         i=i+1;
    end
    if Coord(i,3)==1
        i=i-1;
    end
    Da(k,1)=k;
    if i==i_max
        Da(k,2)=0;
    else
```

```
54          Da(k,2)=Coord(i,2);
55      end
56      if Da(k,2) == Coord(1,2)
57          % terminate loop if crack has completely propagated
58          break
59      end
60  end
61
62  %% Deviation from experimental data
63  CTOD_exp_interp = interp1(Da_exp(2:end),CTOD_exp(2:end),Da(:,2));
64  % quadratic deviation, 10^4 for readability
65  dev = sum(((CTOD_exp_interp-CTOD(1:k)).^2))/length(CTOD_exp_interp)
        *10^4;
66
67  string = ['%6.6f        %6.6f        %6.6f      %6.0f       %6.2f'];
68  fid = fopen('dev.txt', 'a');
69  fprintf(fid, string, pars(1), pars(2), pars(3), pars(4), dev);
70  fclose(fid);
```